Revisiting Gravitational Wave Detection with SCRF Cavities at DESY

Robin Löwenberg

Master Thesis
Universität Hamburg

DESY
April 19, 2023

First Referee: Prof. Dr. Gudrid Moortgat-Pick
Second Referee: Prof. Dr. Krisztian Peters

Abstract

Before the successful detection of gravitational waves (GWs) with LIGO and VIRGO [1], superconducting radio frequency (SCRF) cavities were already considered as potential alternatives for large laser interferometers. They are particularly suited to probe high frequencies above $\sim 10\,\mathrm{kHz}$ by using a heterodyne approach where the GW has to be resonant with the frequency difference of two cavity eigenmodes. Since DESY/UHH and FNAL intend to reactivate the research on these detectors, this thesis revisits the theory of the GW-detector interaction. In this context, we consider the indirect coupling to the cavity boundaries as well as the direct coupling to the electromagnetic field mediated by the Gertsenshtein effect. The formalism is applied to the geometry of the MAGO prototype, which was built in 2005 at INFN in Genoa [2].
We compare the results with recent publications [3, 4] that focus on the same type of detectors. Different to these papers, we include a damping term that was initially found by [5] and significantly flattens the Breit-Wigner curves of the resonances. We further provide a detailed analysis of the mechanical coupling as well as possible noise sources and the prospective sensitivity of the MAGO cavity. The results are compared to signals above 10 kHz from promising candidates for new physics, including primordial black holes (PBHs) and black hole superradiance. We show that future improvements of the MAGO parameters could enable to reach the region of new physics. The aim of this thesis therefore is to provide a basis for future research on the theoretical as well as experimental aspects of the detector, focusing on possible modifications.

Kurzzusammenfassung

Bereits vor der ersten Messung von Gravitationswellen (GW) mit LIGO und VIRGO [1] wurden supraleitende Hohlraumresonatoren im Radiofrequenz-Bereich (auch SCRF Kavitäten genannt) als potentielle Alternativen zu großen Laser Interferometern untersucht. Sie sind besonders dazu geeignet, hohe Frequenzen über $\sim 10\,\mathrm{kHz}$ zu messen. Dabei betrachtet man bevorzugt einen heterodynen Ansatz, bei dem die GW resonant auf die Frequenzdifferenz zwischen zwei Eigenmoden des Hohlraumresonators ist. Aufgrund des Interesses von DESY/UHH und FNAL, die Forschung an diesen Detektoren wieder aufzunehmen, setzt sich diese Arbeit zum Ziel, die Theorie der Wechselwirkung zwischen GW und Detektor neu zu entwickeln. Dabei betrachten wir sowohl die indirekte Kopplung der GW an die Wand des Hohlraumresonators als auch die direkte Kopplung an das elektromagnetische Feld durch den Gertsenshtein Effekt. Der Formalismus wird auf die Geometrie des MAGO-Prototyps angewand, der 2005 am INFN in Genua entwickelt wurde [2].
Wir vergleichen die Resultate mit aktuellen Publikationen [3, 4], in denen dieselbe Art von Detektor untersucht wurde. Im Gegensatz zu diesen Veröffentlichungen berücksichtigen wir einen Dämpfungsterm, der bereits in [5] beschrieben wurde und zu einer Abflachung der Breit-Wigner Resonanzen führt. Desweiteren untersuchen wir die mechanische Kopplung im Detail und analysieren mögliche Störeffekte. Damit schätzen wir dann die Sensitivität von MAGO auf GW ab. Die Ergebnisse werden mit Signalen über 10 kHz von möglichen Kandidaten für neue Physik verglichen. Dabei betrachten wir sowohl primordiale schwarze Löcher als auch Superradianz von schwarzen Löchern. Wir zeigen, dass es mit verbesserten Parametern der MAGO Kavität möglich sein könnte, diese Effekte nachzuweisen. Die Absicht dieser Masterarbeit ist daher, eine Basis für zukünftige Forschung an diesen Detektoren zu bilden, die sich auf die theoretische und experimentelle Weiterentwicklung konzentriert.

Table of Contents

1. Introduction

The first detection of a gravitational wave (GW) in 2016 [1] by the LIGO/VIRGO collaboration opened a new window for research in astrophysics and cosmology. Since then, several black hole and neutron star mergers have been measured, providing remarkable insights into the most energetic processes in the universe [6]. Most of the future efforts to detect GWs will be based on interferometers such as the Einstein Telescope [7, 8, 9] or LISA [10]. Due to the weak signal of GWs, they have to be very large[1], so the question arises whether it is possible to use smaller detectors of a different type. Pioneering work on alternative detector types was already conducted in the 1960s by Joseph Weber, who invented the so-called Weber Bar Detectors [11, 12]. They are based on a simple elastic body that is deformed by an incoming GW. When the GW frequency is resonant with a mechanical eigenmode, the signal is amplified, making it possible to capture the typically very low amplitudes. The displacement is measured by a resonant transducer, i.e. it is converted into an electromagnetic signal. Since these detectors are smaller and less expensive than interferometers, they are easy to fabricate. Examples for Weber Bar experiments conducted around the turn of the millennium include EXPLORER [13], NAUTILUS [14], ALLEGRO [15] and AURIGA [16]. However, they are only sensitive to considerably strong sources in the Milky Way, which are expected to be very rare [11]. Therefore, the larger interferometers were preferred and many scientists that worked on the aforementioned experiments moved to the LIGO/VIRGO collaboration.

Today, improved technologies and a growing interest in frequency ranges beyond the reach of interferometers have led to an intensive search for alternative detector designs. There are currently many concepts on the market, including optically-levitated sensors [17], bulk acoustic wave devices [18, 19, 20] and superconducting rings [21, 22], that are being discussed or already in operation. Although they may not have the required sensitivities, exotic ideas are also being considered, such as measuring the GW interaction with a Bose Einstein condensate [23, 24]. Particularly high frequency GWs above $\sim 10\,\mathrm{kHz}$ are of interest as there are no known sources at this frequency in the Standard Model of particle physics and cosmology. Thus, discoveries of such sources would definitely point towards new physics. These prospects have led to the formation of the Ultra-High-Frequency Gravitational Wave (UHF-GW) initiative, which aims to create a network of researchers searching for GWs above $10\,\mathrm{kHz}$ [25]. A comprehensive overview of potential sources and further experimental approaches can be found in [26].

In this master thesis, we want to focus on a different approach, which is comparable to that of the Weber Bar detectors. Instead of a solid mechanical resonator, however, the GW couples to an electromagnetic field trapped in a cavity. There are two ways to design such an experiment. The first method uses a static B-field and utilizes the inverse Gertsenshtein effect [27, 28], which means that the GW directly couples to the electromagnetic field and resonantly induces a photon in an eigenmode of the cavity. Similar experiments such as ADMX [29] and HAYSTACK [30] are currently under operation to search for Axions, which couple to the electromagnetic fields in an analogous way. The possibility of using them for GW detection as well was proposed in

[1] The two arms of LIGO, for instance, have a length of $4\,\mathrm{km}$. LISA will even provide an arm length of $2.5\times10^6\,\mathrm{km}$.

[31], where sensitivity estimates are given as well.
The second method uses a heterodyne approach where the GW is resonant with the frequency difference between two electromagnetic cavity eigenmodes. This is particularly suited for GWs in the 1 kHz to 10 MHz range, where cavities with corresponding eigenmodes have to be very large. The frequency difference, however, is in principle independent of the cavity size and allows for compact designs even in the kHz regime. We will therefore focus on this concept throughout the thesis.
It should be pointed out that the heterodyne approach is not a novel one. First proposals were made already in the 1970s [32, 33, 34, 35, 36, 37], about ten years after the Weber Bar detectors were suggested. Important for the physical understanding was that the Gertsenshtein effect is suppressed at low frequencies and that an indirect coupling of the GW to the cavity boundaries dominates. The changing boundaries lead to an overlap between the modes, allowing them to exchange energy. In earlier works (e.g. [37]), the effect was described by an effective dielectric and magnetic permeability tensor. A more direct formalism based on elasticity theory was invented by J. Lobo in 1995 [38]. In the same paper, he also pointed out that the geometry that provides the best coupling to the GW is given by a sphere.
First attempts for an experimental implementation were made in 1984 [39], which led to further studies at INFN in the late 90s [40, 41, 42]. The main challenge was to build a cavity that has two nearly degenerate eigenmodes, which is not possible with a single sphere. One can solve this by using two coupled spheres so that each eigenmode splits into a symmetric and an antisymmetric part. For financial reasons, INFN started with a cylindrical design that was not optimized for GW detection. The first prototype *PArametric COnverter* (PACO) [41] obtained the two nearly degenerate modes with two cylindrical cavities coupled by an axial iris. A sketch and a picture of the final prototype can be found in figure 1.1.
Successful operation and characterization of the electromagnetic and mechanical properties led to further studies with improved cavity geometries. An important step was the implementation

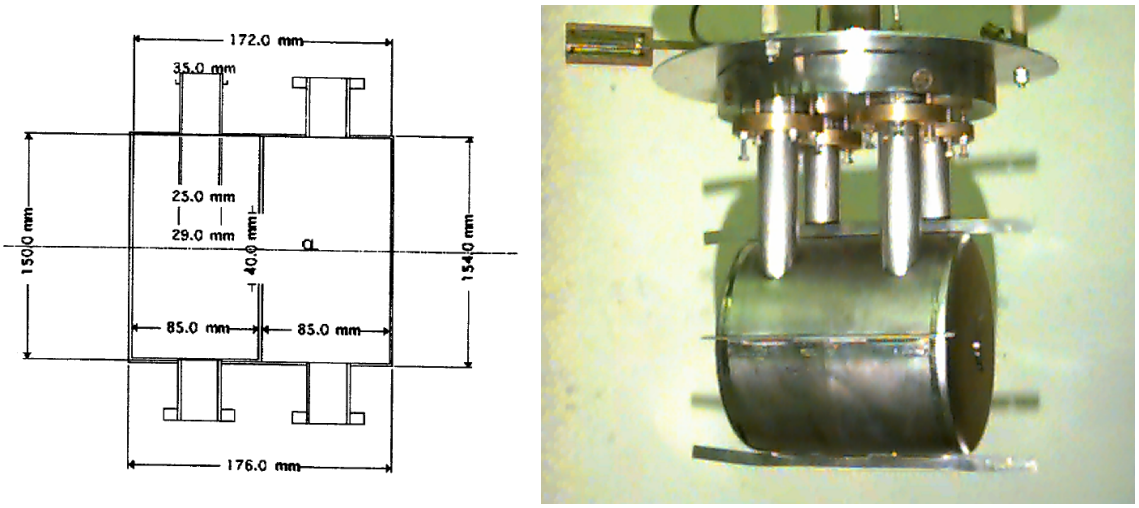

(a) *Technical drawing of PACO [40].*

(b) *Picture of the PACO prototype.*

Figure 1.1.: *The PACO prototype. (a): Technical drawing showing how the cylindrical cavities are coupled. (b): Picture of the final prototype at INFN (Image credits to Gianluca Gemme (INFN)).*

of the required spherical geometry, which resulted in another two prototypes called *Microwave Apparatus for Gravitational Waves Observation* (MAGO) in 2005 [2, 5]. They consist of two slightly flattened spheres with a central coupling system that is either constant or tunable with an additional tuning cell. The goal was to be sensitive in a frequency range of 5 kHz to 20 kHz. To achieve a high cavity quality factor and thus improve the sensitivity, superconducting shell material requiring a cryogenic system to cool the walls should be used. Pictures of the prototypes and a technical drawing can be found in figure 2.3 and 2.4.
However, the funding was stopped shortly after the initial proposal, so the cavity was never put into operation. Many key tasks such as a detailed simulation, characterization and measurement of the mechanical eigenmodes and the development of a suitable cryogenic system remained open. Just as with the Weber bar detectors, most researchers of the MAGO collaboration moved to LIGO and VIRGO.
Improvements in cavity technology, noise reduction and cryogenics have led to an increasing interest in MAGO type cavities over the last years. Since it was suggested in [3, 43] that similar experiments can be used for Axion detection, particularly DESY/UHH and FNAL are interested in reactivating the research on heterodyne cavity detectors. The current plan is to gather first experiences with the original MAGO prototype, which is currently at the INFN in Genoa. Attempts to loan the cavity were successful, enabling first experiments to be scheduled at DESY/UHH in spring 2023. The main goal is to characterize the mechanical spectrum and the electromagnetic resonances at room temperature. Subsequently, the cavity will be taken to FNAL, where first cold tests will be conducted. Eventually, it will come back to DESY/UHH, where the mechanical spectrum will be studied again at cold temperatures. While the cavity is at FNAL, a PhD student is going to develop a method for conducting the complicated measurements. After these basic studies, the long-term goal is to build new detectors, possibly with different geometries, and to improve the sensitivity as well as the frequency range.
The work on this master thesis started before the collaboration between INFN, DESY/UHH and FNAL was initiated, and even before DESY/UHH decided to focus on this project. It is based on a talk by Sebastian Ellis [44] given in 2021 at DESY as well as the aforementioned proposals to use the same types of detectors for Axion research [3, 43]. The main goal is two-fold: First, we aim to provide a comprehensive and complete theoretical treatment of the interaction between GWs and the electromagnetic field in the cavity. This includes the mechanical interaction which was already considered by the MAGO collaboration as well as the Gertsenshtein effect. Although the latter is suppressed at low frequencies, we assume that the cavities could have a tunable frequency difference $\sim \mathcal{O}(1\,\mathrm{GHz})$, where the effect becomes dominant. The theoretical part is mainly based on previous works, in particular [4, 5, 31], but we translate the results into a novel, consistent formalism and provide some extensions (for instance, a new treatment of the Gertsenshtein effect).
It is important to point out that there is currently no scientist at DESY/UHH who has worked on this detector type before. Another advantage of a detailed theoretical treatment therefore is a general understanding of the system and its parameters. This allows for making electrodynamic and mechanical simulations and to apply the final formalism to the MAGO prototype. Therefore, a 3D model of the prototype is needed, which was, unfortunately, not available during the work on this thesis. We only had technical drawings of the cavity with constant coupling (see figure 2.4), so the measure of the tuning cell had to be estimated. With the approximated model, we were able to calculate the important couplings of GWs to the cavity and to analyse the sensitivity reach.

With the methods and results shown in this thesis, future bachelor, master or even PhD students should have a guideline to conduct more accurate and detailed studies of the original MAGO design. Many theoretical calculations shown here are carried out for special cases[2], so there are many possibilities to look at more general configurations in future.
It should be noted that we are not the only group working out the theoretical details of MAGO. A collaboration of scientists from different universities in Europe[3] revisited the physics of this detector type as well and published a paper in March 2023 (Berlin et al. [4]). The content is similar to this thesis, so we will often refer to the paper and compare the results. We point out that our approach is primarily based on first principles, while many terms are introduced by hand in Berlin et al. [4]. This results in one important difference: We also account for the field back-action to the mechanical modes which leads to a considerable damping of the signal (also called Lorentz Force Detuning). Since it simultaneously reduces the noise as well, the effect does not change the overall conclusions of Berlin et al. [4], but it changes the hierarchy of the contributions from different mechanical modes to the signal. Furthermore, Berlin et al. [4] only works with perfect spheres that are coupled by a cylinder of some unspecified radius and does not consider the real MAGO design. This thesis provides calculations for the couplings of the original prototype.
This thesis is structured as follows: We start with a detailed description of heterodyne cavity experiments with a particular focus on the MAGO design in chapter 2. We discuss the mechanical and electromagnetic properties as well as the tuning mechanism and possible modifications for future cavities. In chapter 3, we provide a detailed theoretical background of cavity electrodynamics. Starting with basic properties of eigenmodes, we discuss ways to describe energy and spectral distributions of the electromagnetic fields. A key ingredient to describe the mechanical coupling to the electromagnetic field is cavity perturbation theory, which is also fully developed. Chapter 4 is devoted to the theory of GWs and some techniques from relativistic geodesy. Most of the content is standard textbook material, but we also give a detailed discussion of the proper detector frame which we need to properly describe the Gertsenshtein coupling. In chapter 5, we show the proper theoretical treatment of the (inverse) Gertsenshtein effect and derive the full Lagrangian of the system. The equations of motion are then solved in chapter 6, where we also analyze the coupling coefficients for the MAGO design and discuss the signal power for a toy GW with strain $h_0 = 10^{-20}$. In order to make predictions for the sensitivity, we give a theoretical discussion of the five most important noise sources in chapter 7. Additionally, other possible noise sources are discussed, but we neglect them as they are expected to be much less dominant. We then show estimates for the sensitivity in chapter 8 and compare them with the results from [4]. Chapter 9 finally discusses possible sources of high frequency GWs from extensions of the Standard Model of particle physics and cosmology and compares the expected strains with the sensitivity of MAGO. We particularly concentrate on primordial black holes (PBHs) and black hole superradiance as they are the most promising candidates which could be measurable in the foreseeable future. We conclude the results in chapter 10 and give a detailed outlook to future developments of the experiment together with open questions for the next step of theoretical studies. This chapter may serve as an inspiration for future bachelor and master projects.
In the appendix, one can find additional information for some of the theoretical topics. We

[2] For example, we only consider monochromatic GWs travelling in z-direction throughout the thesis, which is a very strong restriction.
[3] The same group has also studied the application of heterodyne cavities to Axion detection [3, 43] and the Gertsenshtein effect in static B-field experiments [31].

shortly discuss aspects of elasticity theory in appendix A and some more details on cavity eigenmodes in appendix B. Appendix C gives an alternative approach to treat thermal noise in the cavity and appendix D discusses prospects of Axion detection. Finally, appendix E provides an overview over some technical parameters of MAGO.

2. Heterodyne Gravitational Wave Experiments

This chapter gives a short introduction to heterodyne experiments and how they can be used to detect GWs. We start with the general principle and the two different couplings of a GW that can cause a signal in the readout system. Since this thesis is based on previous studies of the former MAGO collaboration, we further discuss their scientific goals and the particular cavity design they choose. In 2005, the project was cancelled due to financial reasons and only some prototypes were built, which were exhibited at the University of Genoa [4] for several years. Currently, one of them is borrowed by UHH and DESY to make first measurements, and is going to be moved to FNAL where further measurements will be conducted. This shows the huge scientific interest on the MAGO cavity design and it will therefore be also the focus of this thesis. However, we will conclude this chapter with a short discussion of possible improvements of the design and tuning mechanism, which will be necessary to cover the full potential of the experiment in future.

2.1. General Principle

Heterodyne Cavity setups for GW detection were first suggested in the 1970s by [32, 33] with further developments by [35, 36]. The basic idea is that a GW can couple to the electromagnetic field of a resonator and therefore induces an overlap of the eigenmodes. This overlap can be measured with an appropriate setup. As a resonator we use an electromagnetic cavity which is well known from accelerator physics and already used in Axion experiments such as ADMX [29] and HAYSTAC [30]. An external oscillator resonantly excites a specific eigenmode ω_0 which we denote as *pump mode* throughout this thesis. We then consider a second mode ω_1, which is nearly degenerate to the first one and in best case not excited by the oscillator[1]. If the GW is resonant to the frequency difference between the two modes, i.e. $\omega_g \approx |\omega_1 - \omega_0|$, it will induce a transition of the photons from the pump mode to the second mode, which we therefore call *signal mode* in the following. An additional readout system is then coupled to the signal mode to search for the excited photons. A sketch of the principle is shown in figure 2.1.
Ideally, the readout measures no signal unless a GW propagates through the system. However, there are several possible noise sources that can induce photons in the signal mode. They are treated in detail in chapter 7. Another problem is that, for instance due to ohmic losses through the cavity walls, cavity eigenmodes are in general not perfectly monochromatic. This leads to a Breit-Wigner shape of the mode spectrum where its width is governed by the so-called quality factor (see chapter 3.2 for more details). If the frequency difference, i.e. $|\omega_1 - \omega_0|$, is too small, the Breit-Wigner curves overlap which makes it difficult to distinct between the modes. It is therefore necessary to achieve quality factors that are as high is possible. One way to do this is to use superconducting radio frequency (SCRF) cavities that are cooled below the

[1] This can in general not be perfectly achieved as the oscillator always couples to the second mode with a factor ϵ. One important task of the cavity design is to keep ϵ as small as possible. We will discuss this in detail in later chapters, in particular chapter 7.

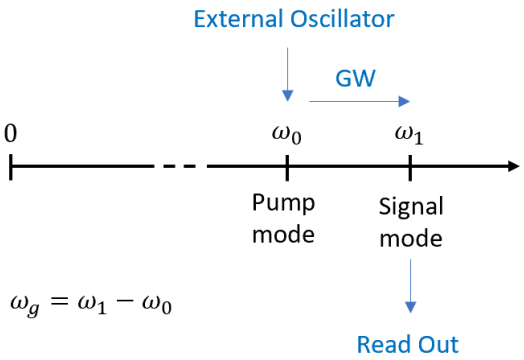

Figure 2.1.: *This sketch shows the principle of heterodyne cavity experiments. One eigenmode ω_0, called pump mode, is excited by an external oscillator. When a GW propagates through the system, it induces a transition from the pump mode to a second mode ω_1, called signal mode. A readout system is then coupled to the signal mode. If photons reach the readout, we know in principle that there was a GW. The advantage of this approach is that the GW ideally has a frequency $\omega_g \approx |\omega_1 - \omega_0|$, which can be much smaller than the frequency of the cavity eigenmodes.*

critical temperature of the shell material. The MAGO collaboration [2] used Niobium, which can achieve very high quality factors ($\sim \mathcal{O}(10^{11})$) in the superconducting state.
In principle, a GW could also couple to a static B-field in the cavity such that it resonantly enhances the cavity eigenmodes directly. This approach is used by the aforementioned Axion experiments ADMX and HAYSTAC. In [31], it is argued that these experiments should be already sensitive to GWs with strains $h \gtrsim \mathcal{O}(10^{-22})$ in the appropriate frequency band. However, the best signal strength is achieved when a GW is resonant with an eigenmode, which typically has a frequency above c/L_{cav}, where L_{cav} is the typical size of the cavity. For MAGO with $L_{\text{cav}} \sim 50\,\text{cm}$, this corresponds to $\omega_g \sim 3.77\,\text{GHz}$. Sources with these frequencies are scarcely predicted by theoretical models, so the physical motivation to search in this region is very low. The heterodyne setup can be, in principle, tuned to arbitrary frequencies above $\mathcal{O}(1\,\text{kHz})$ and is therefore able to scan a much larger and more promising frequency region.
There is another reason why the heterodyne approach is favourable compared to static B-field experiments for GW frequencies much below $\mathcal{O}(1\,\text{GHz})$. In the following, we will only give a brief presentation of the arguments. More details on the GW-cavity interaction can be found in chapter 5 and 6. The idea is that a passing GW induces an effective current $\vec{J}_{\text{eff}} = g_{\text{GW}}(t)\vec{F}_0(t)$ inside the cavity consisting of a function $g_{\text{GW}}(t) \sim e^{i\omega_g t}$ that describes the GW with frequency ω_g and a field $\vec{F}_0(t)$ that can be either the E-field or the B-field. We start with Ampéres law

$$\nabla \times \vec{B} = \mu_0 \vec{J}_{\text{eff}} + \mu_0 \varepsilon_0 \frac{\partial \vec{E}}{\partial t}$$

which can be written as a wave equation

$$\Delta \vec{E} + \frac{\partial^2 \vec{E}}{\partial t^2} = \mu_0 \frac{\partial \vec{J}_{\text{eff}}}{\partial t}$$

by using the Maxwell equations. Thus, the effective current induced by the GW drives the electromagnetic field in the cavity. In a static setup where $\vec{F}_0(t) = \vec{F}_0$, the driving term becomes

$\partial_t \vec{J}_{\text{eff}}(t) \sim i\omega_g \vec{J}_{\text{eff}}(t)$. On the other hand, if $\vec{F}_0$ corresponds to an eigenmode of the cavity with frequency ω_0, i.e. $\vec{F}_0 \sim e^{i\omega_0 t}$, we get $\partial_t \vec{J}_{\text{eff}}(t) \sim i(\omega_0 + \omega_g)\vec{J}_{\text{eff}}(t)$. Since $\omega_g \ll \omega_0$, the effective current in the heterodyne setup is therefore much larger.
For the same reasoning, the heterodyne approach was recently suggested for axion searches [3, 43, 45], since the axion coupling to the electromagnetic field is similar to the GW coupling. We will discuss some aspects of axions in Appendix D, where they are described as an additional noise source.

2.2. Gravitational Wave Couplings

In the last chapter, we described the general principle of heterodyne experiments without giving details on how a GW interacts with the electromagnetic field. This coupling is not trivial and can be split into two different channels [4, 37]. The first one is the *direct* coupling of the GW to the electromagnetic field via the inverse Gertsenshtein Effect [27, 28, 31, 46]. It is usually described in terms of classical field theory, which we will employ in chapter 5.1. However, we can also understand the effect as a graviton-photon interaction in the particle picture.
In the long wavelength approximation, i.e. where the wavelength of the GW is assumed to be much larger than the cavity size, we can distinguish between a GW coupling to the E-field and to B-field. These couplings are denoted by the overlap factors η_{01}^{E} and η_{01}^{B} respectively. A detailed derivation is given in chapter 5.4. The solutions are

$$\eta_{01}^{\text{E}} = \frac{1}{H\sqrt{U_0 U_1}} \int_{V_{\text{cav}}} \mathrm{d}^3x H_0(\vec{x}) \varepsilon_0 \vec{E}_0(\vec{x}) \vec{E}_1(\vec{x})$$
$$\eta_{01}^{\text{B}} = \frac{1}{H\sqrt{U_0 U_1}} \int_{V_{\text{cav}}} \mathrm{d}^3x H_0(\vec{x}) \frac{1}{\mu_0} \vec{B}_0(\vec{x}) \vec{B}_1(\vec{x}),$$

where $\vec{E}_0$, $\vec{B}_0$ and $\vec{E}_1$, $\vec{B}_1$ are the pump and signal modes. Furthermore, $H_0(\vec{x})$ represents the GW and H, U_0 and U_1 are some normalization factors.
The second channel is an *indirect* coupling of the GW to the mechanical modes of the cavity shell. The deformation leads to an overlap between the cavity eigenmodes and can be described within cavity perturbation theory (see e.g. chapter 3.4). In the particle picture, it can be understood as a GW-phonon-photon interaction.
The GW-mechanical coupling for a monochromatic GW is described by two coupling coefficients Γ_+ and $\Gamma_\times$ corresponding to the polarisation. They are derived in chapter 4.5 for a GW travelling in z-direction and yield

$$\Gamma_+ := \frac{V_{\text{cav}}^{-1/3}}{M} \int_{V_{\text{cav}}} \mathrm{d}^3x \rho(\vec{x}) \big(x\xi_{l,x}(\vec{x}) - y\xi_{l,y}(\vec{x})\big)$$
$$\Gamma_\times := \frac{V_{\text{cav}}^{-1/3}}{M} \int_{V_{\text{cav}}} \mathrm{d}^3x \rho(\vec{x}) \big(x\xi_{l,y}(\vec{x}) + y\xi_{l,x}(\vec{x})\big),$$

where ρ is the density of the cavity shell and $\vec{\xi}(\vec{x})$ the shell displacement field.
The mechanical-electromagnetic coupling is given by a connection coefficient C_{01}^l, which we derive in chapter 3.4, where we find

$$C_{01}^l = \frac{V_{\text{cav}}^{1/3}}{2\sqrt{U_0 U_1}} \int_{\partial V_{\text{cav}}} \mathrm{d}\vec{S} \cdot \vec{\xi}_l(\vec{x}) \Big[\frac{1}{\mu_0} \vec{B}_0(\vec{x}) \vec{B}_1(\vec{x}) - \epsilon_0 \vec{E}_0(\vec{x}) \vec{E}_1(\vec{x})\Big],$$

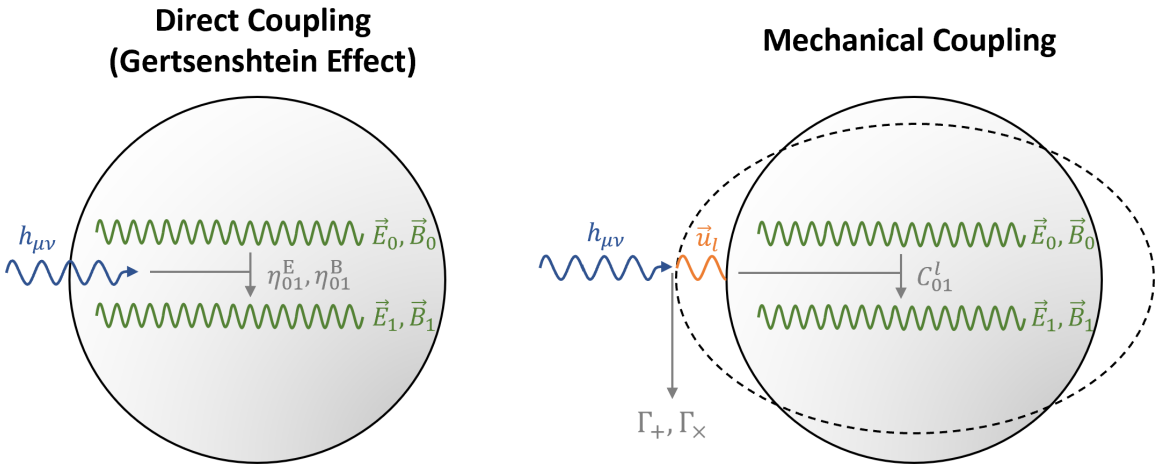

Figure 2.2.: *This sketch shows the two different channels of the GW interaction with the electromagnetic field. On the left, the direct coupling via the inverse Gertsenhtein effect is shown governed by two couplings η^E_{01} and η^E_{01} in the long wavelength regime. Note that $h_{\mu\nu}$ denotes the strain of the GW, which is supposed to be monochromatic throughout this thesis. On the right, the indirect coupling of the GW over a mechanical mode $\vec{u}_l$ is shown. It can be understood as a graviton-phonon-photon interaction in the particle picture. The GW-mechanical coupling can be described by two coupling coefficients Γ_+ and $\Gamma_\times$, while the mechanical-EM coupling is governed by the connection coefficients C^l_{01}. In both pictures, $\vec{E}_0$, $\vec{B}_0$ and $\vec{E}_0$, $\vec{B}_0$ are the fields of the pump and signal mode, respectively.*

Here, we integrate over the unperturbed surface of the cavity shell. An appropriate design in order to achieve high signal must be chosen such that all coupling parameters are maximized. The main properties that have to be fixed are the cavity geometry as well as the mechanical and electromagnetic eigenmodes. Additionally, the noise must remain as low as possible and the frequency difference between pump and signal mode should be tunable over a wide frequency range. We will further discuss this in chapter 2.3 and 2.5. A sketch of all couplings is shown in figure 2.2.
As argued in [4], the mechanical coupling is supposed to give the strongest signal in the cavity. The main reason for this is that

$$\frac{|\vec{E}^{(\mathrm{mech})}_{\mathrm{sig}}|}{|\vec{E}^{(\mathrm{EM})}_{\mathrm{sig}}|} \propto \frac{c}{c_{\mathrm{s}}} \approx 10^6$$

where c_{s} is the speed of sound in the cavity shell. However, this assumption is made for the long wavelength regime and the mechanical signal is supposed to go down for higher GW frequencies. We will therefore analyze both channels and in particular consider the behaviour of the Gertsenshtein coupling towards higher frequencies.

2.3. MAGO and MAGO Design

The MAGO cavity proposed in [2] was designed to scan over a frequency regime from 4 kHz to 20 kHz. Since our goal is to scan a much larger region up to $\sim$ 1 GHz, the design is not

(a) *Fixed Coupling*

(b) *Variable Coupling*

Figure 2.3.: *Pictures of the prototypes built by the MAGO collaboration. (a): Cavity with fixed coupling, where no tuning is possible. In figure 2.4, technical drawings of this cavity are shown. (b): Cavity with central tuning cell. We had to guess the shape of the cell in order to construct a 3D model of the system. Image credits to Gianluca Gemme (INFN).*

sufficient for our purposes. However, first experiments at DESY and FNAL will be conducted with the MAGO prototype to gain experience with the cavity and the measurement techniques. We therefore concentrate on this particular design throughout the thesis as it will find direct application in the foreseeable future. Possible modifications in order to reach higher frequency differences are discussed in chapter 2.5. We also note that, as pointed out in [4, 43], it is possible to make broadband measurements even with small frequency differences.

It was first shown in [38], that the detector design which is most sensitive to GWs is given by a spherical cavity. The main reason is that a GW only couples to a discrete set of $l = 2$ eigenmodes, so the energy is less distributed. In [5], it was further pointed out that spherical cavities have particularly large quality factors (see chapter 3.2), which is important to separate signal mode and pump mode.

Pure spherical shapes, however, are not well suited for heterodyne GW detection. GWs are spin 2 waves, so due to angular momentum conservation, the pump and signal mode must differ as $\Delta l = 2$ to achieve the optimal coupling. Furthermore, the required modes must be nearly degenerate and we need an efficient mechanism to tune the frequency difference between them. As argued in [3], these requirements are scarcely fulfilled by spherical cavities.

The MAGO collaboration solved the problem by using two coupled spheres with a malleable central tuning cell [2, 5, 40], see figure 2.3. In addition, it turned out to be advantageous to slightly flatten the spheres such that they form an ellipsoid. This allows for a better control of the orientation of the electromagnetic fields, which is important to achieve the required $\Delta l = 2$ difference between the pump and signal mode. In the coupled system, the modes corresponding to the initial spherical eigenmodes split into a symmetric and antisymmetric part which are nearly degenerate. The level of degeneracy depends on the coupling and can therefore be easily tuned. As shown in [2], the most appropriate mode is the TE_{011}[2] mode.

[2]We use the standard convention that TE denotes the *Transverse Traceless* and TM the *Transverse Magnetic* mode.

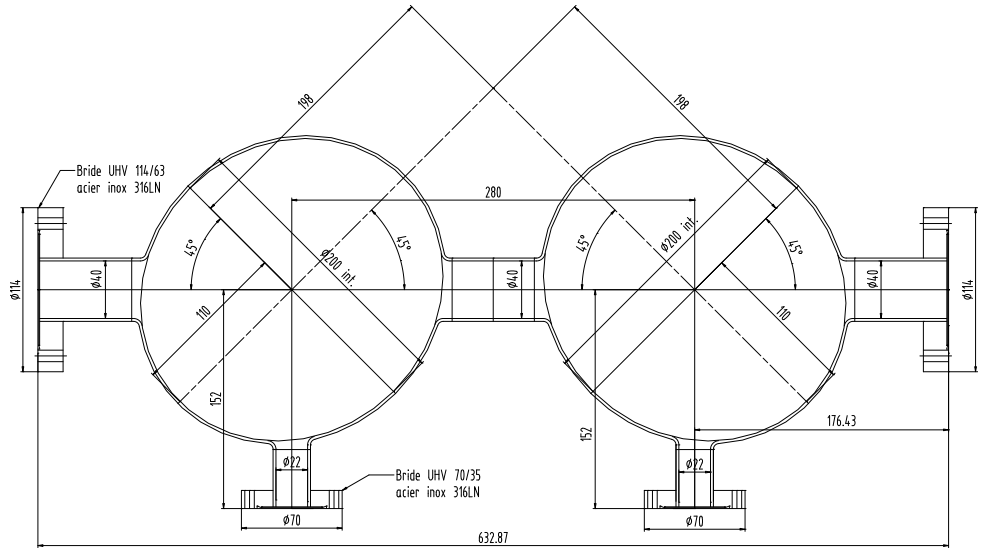

Figure 2.4.: *Technical drawing of the MAGO design with fixed coupling. Shown are the size and orientation of the cavity cells as well as the flanges that couple the cavity to the external oscillator and readout. Image credits to Gianluca Gemme (INFN).*

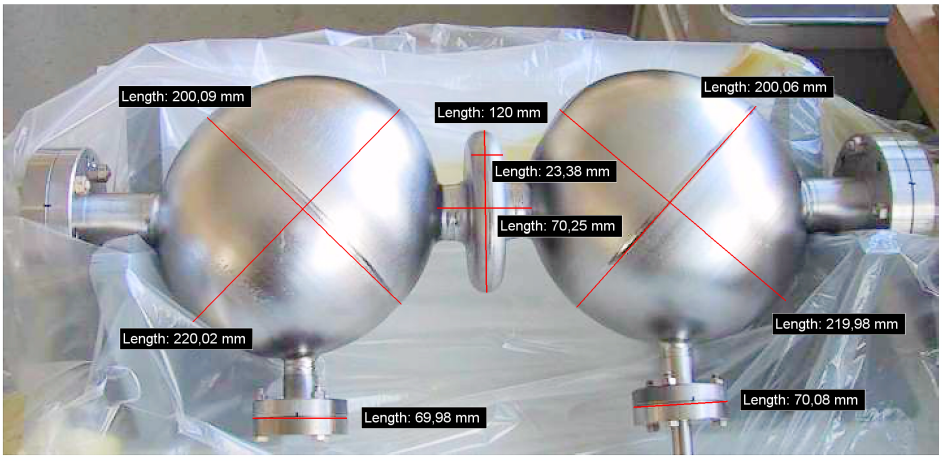

Figure 2.5.: *Qualitative analysis of the cavity measure with variable coupling. The open source program IC Measure was used for the measurement. It is important to note that these are only rough values due to a possible bias in perspective. Accurate values can only be obtained by direct measurements at the real cavity, since technical drawings for the variable coupling were not available. When this thesis was written, DESY did not have the cavity, so we had to use this way to obtain parameters for the simulations.*

Two prototypes were built by the MAGO collaboration which are both shown in figure 2.3. One has a fixed coupling where no significant tuning is possible (figure 2.3a). The other has a central cell which can be stretched an squeezed and therefore allows for a variable tuning of the geometry (figure 2.3b). From Gianluca Gemme, one of the former MAGO members, we only received a technical drawing for the system with fixed coupling, which is shown in figure 2.4. When this thesis was written, direct measurements at the real prototype were not possible as DESY did not yet have the cavity. For the tunable version, we therefore had to estimate the exact size and shape of the central cell from the pictures. A picture of the qualitative analysis is shown in figure 2.5. It is important to note that the obtained values could be inaccurate due to a possible bias in perspective. However, they were sufficient to construct a 3D model which contains the most important properties of the cavity.
To simulate the electromagnetic fields, we used *CST Microwave Studio* from Dassault Systèmes. With the available measures, it was straightforward to build a 3D model and to run the eigenmode solver of the program. The total electric field of the required symmetric and antisymmetric TE_{011}-modes is shown in figure 2.6. Some properties can be better seen by considering the vector field, which can be done in figure 2.7. On the left cell, the symmetry difference between the modes is depicted. We also see that the fields are aligned along the minor axis of the ellipse, which shows that we have better control over the field alignment compared to an approach with pure spheres. Note that the field strength is arbitrary and will be normalized to the input energy in the pre-processing. From [2] and the 3D model, we were able to derive some important properties of the MAGO cavity that are useful for the later calculations. First of all, we note that the detector is made of niobium. This has some advantages concerning the malleability and superconductivity. For the latter, the critical temperature is $T_c \approx 9.2\,\mathrm{K}$ and the critical magnetic field is $B_c \approx 180 - 200\,\mathrm{mT}$ [47]. Since the signal is proportional to the energy stored in the electromagnetic field, we have to operate the cavity near the quenching limit. We adopt the value for the average pump field strength from [4], which is assumed to be $\langle E_0 \rangle = 30\,\mathrm{MV/m}$.

Table 2.1.: *This table shows some important material parameters. The values for niobium are highlighted in bold. Note that RRR corresponds to Residual Resistivity Ratio, which is 300 in this case. Further values are given for annealed copper (OFE = Oxygen Free Electronic Grade) and stainless steel (LN = Low carbon, Nitrogen). Thanks to Marc Wenskat for providing us with these data.*

Material	Temperature [K] [K]	Density [kg/m^3]	Young's Modulus [GPa]	Poisson's Ratio
Cu OFE Annealed	293	8930	115	0.344
SS 316LN		7950	196	0.27
Nb RRR 300		**8570**	**106**	**0.40**
Cu OFE Annealed	2	8930	138	0.377
SS 316LN		7950	208	N/A
Nb RRR 300		**8570**	**104.8**	**N/A**

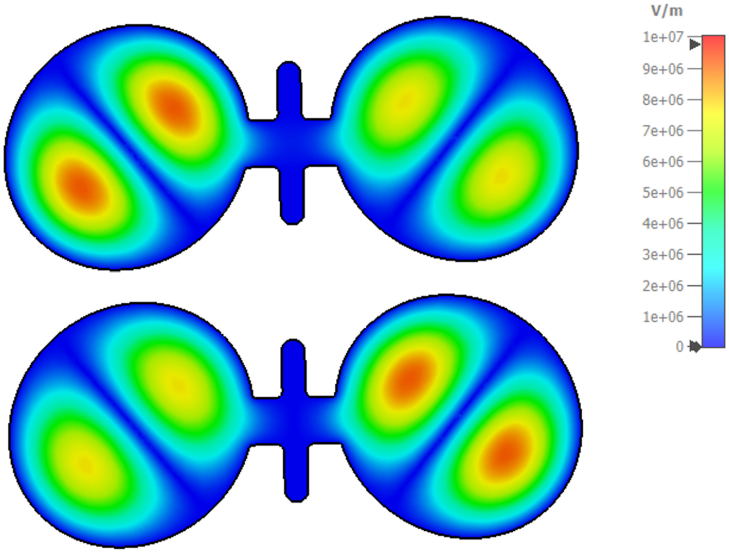

Figure 2.6.: *Pump mode with* $\omega_0 = 1.773430\,GHz$ *(upper plot) and signal mode with* $\omega_1 = 1.773446\,GHz$ *(lower plot) of the MAGO-like cavity. The frequency difference is* $\omega_1 - \omega_0 \approx 16\,kHz$*. Note that the field strength is arbitrary and will be normalized in post-processing.*

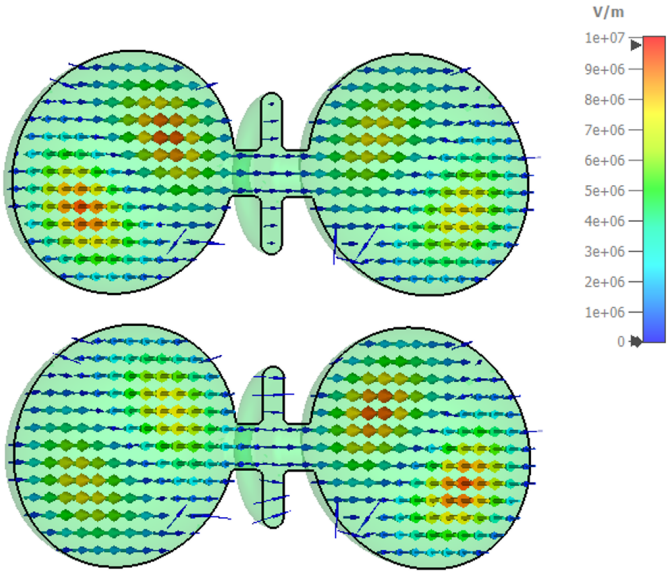

Figure 2.7.: *Vector fields of the pump mode with* $\omega_0 = 1.773430\,GHz$ *(upper plot) and signal mode with* $\omega_1 = 1.773446\,GHz$ *(lower plot). In the left cell, it can be seen that the signal mode is antisymmetric. Note that the field strength is arbitrary and will be normalized in post-processing.*

It leads to a total energy of[3]

$$U_0 = \frac{\varepsilon_0}{2} \int \mathrm{d}^3 x \vec{E}_0^2 \approx \frac{\varepsilon_0}{2} V_{\mathrm{cav}} \langle E_0 \rangle^2 \approx 40\,\mathrm{J},$$

where we used the cavity volume $V_{\mathrm{cav}} \approx 0.0096\,\mathrm{m}^3$. Another important value is the shell surface, which we measured to be[4] $A_{\mathrm{cav}} \approx 0.3111\,\mathrm{m}^2$. For the mechanical simulation, we additionally need some material properties such as the density, Young's modulus and Poisson's ratio. They can be found in table 2.1. An overview of all assumed MAGO parameters can be found in appendix E.

Finally, we also conducted a first analysis of the tunability. For MAGO, the idea was to use piezoelectric elements to slightly deform the central cell. For instance, one could place the elements such that the cell diameter can be changed. We performed a parameter sweep and varied the diameter from 20 mm to 30 mm. The result is shown in figure 2.8. One can see that the frequency difference could roughly be tuned from 16 kHz up to 18 kHz, so a range of 2 kHz can be probed. However, the MAGO collaboration proposed that the cavity will be able to scan over a much larger range, i.e. 5 kHz to 20 kHz. The reason why the influence of the central tuning cell is so small can be seen in figure 2.6. A deformation of the cell changes the electromagnetic field in a region where it is weak, so it only needs small modifications to fulfill the new boundary conditions. However, in future analysis, also the changing of the distance between the cells should

[3] See chapter 3.2, eqn. 3.16.

[4] Note that COMSOL does not specify errors, so we do not mention them here either.

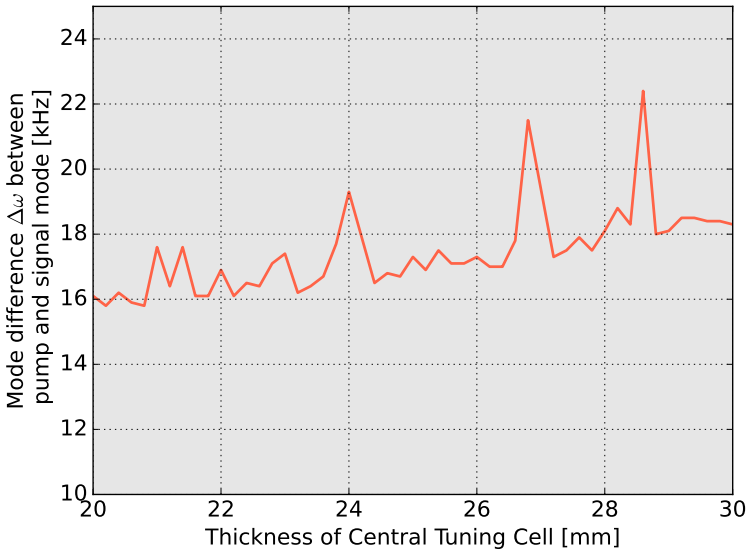

Figure 2.8.: *Parameter sweep of the cell diameter from 20 mm to 30 mm. The frequency range varies from 16 kHz to 18 kHz, so a scan over 2 kHz is possible. The strong fluctuations are likely numerical issues as the mode frequencies are much higher than the difference between them. A problem is that the shell deformation is performed at regions with small field gradients, so the field is only slightly modified to fulfill the new boundary conditions. For the final detector, we require a much larger tuning range. Note that we did not consider that a deformation of the cell also changes the distance between the cavities, which may allow for a larger scanning region.*

be put into account. In the best case, the cavity should be malleable at a place with large field gradients, which would lead to a broader frequency range. Therefore, it is necessary to further investigate possible tuning mechanisms in the future. One example is shown in chapter 2.5.

2.4. The Mechanical Spectrum of MAGO

In the penultimate chapter we discussed that a GW can induce a signal by coupling first to the mechanical eigenmodes of the shell. It is therefore important to investigate the shell resonances as they have a direct influence on the outcoming signal power.

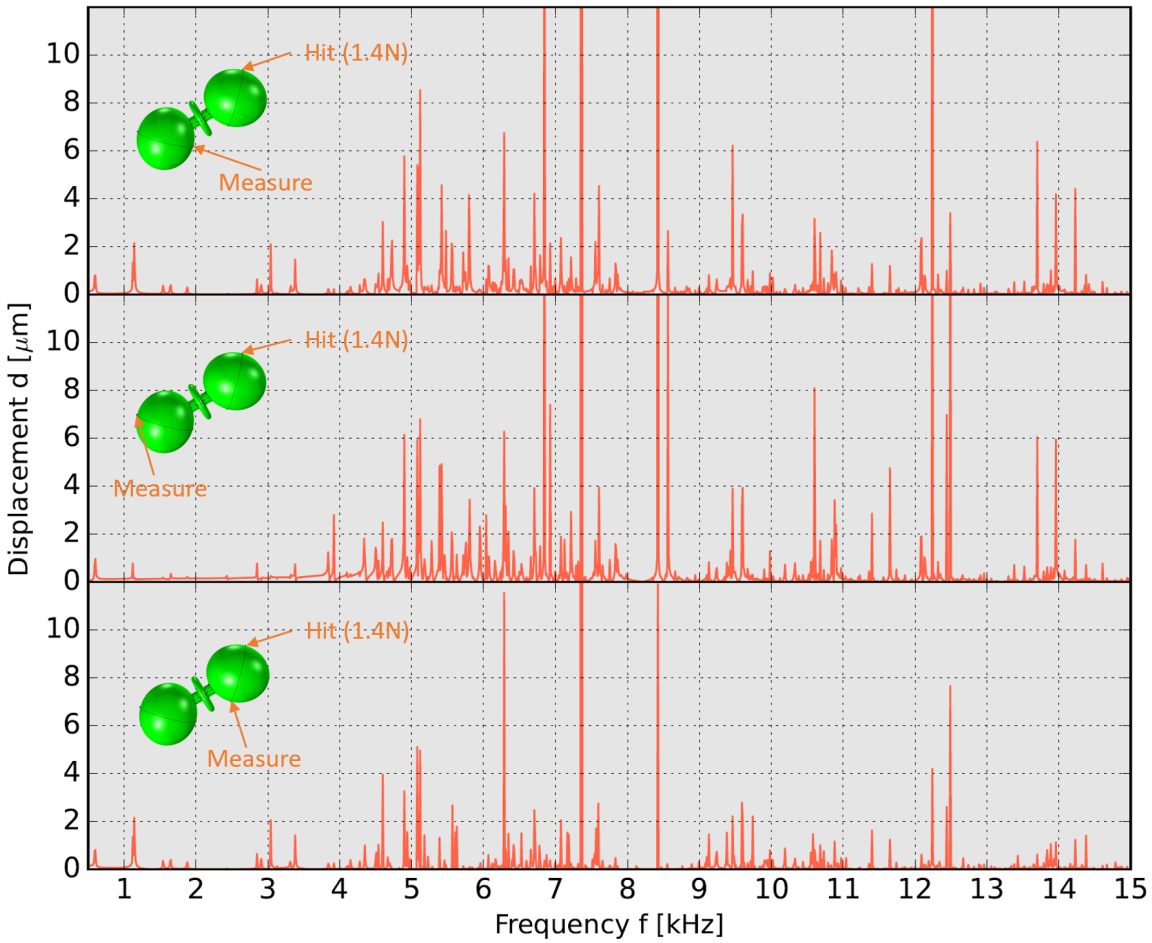

Figure 2.9.: *Simulated mechanical spectrum of the MAGO-like cavity at room temperature, which is measured at three different positions. The mechanical resonances are excited by hitting one point of the cavity with a hammer (here with 1.4 N). On the left, we show the locations of the detectors and the position of the blow. For some excitations, the scale of the y-axis is too small. A more appropriate scaling is shown in figure 2.10. However, the excitations dominate in this plot such that the other modes can not be resolved.*

First measurements of the cavity are going to be conducted at room temperature. The idea is to hit the cavity with a hammer at one point and to place several detectors at different positions on the shell to measure the local displacement. We performed a simulation of such a measurement with the MAGO geometry using the *Frequency Domain* tool from COMSOL. The result is shown in figure 2.9. Some modes are very dominant and the chosen scaling only covers the spectrum of the weak modes. The dominant resonances are better resolved in figure 2.10, which is the same plot with a larger scaling of the displacement. We see that some modes are between one and two orders of magnitude stronger than the rest. When the original MAGO cavity will arrive at DESY, we will be able to measure the real spectrum and see if it matches with the predicted behaviour.
With the *Eigenmode* solver of COMSOL, it is further possible to calculate the displacement fields of the eigenmodes. We identified the mode shapes of the two most dominant modes. They

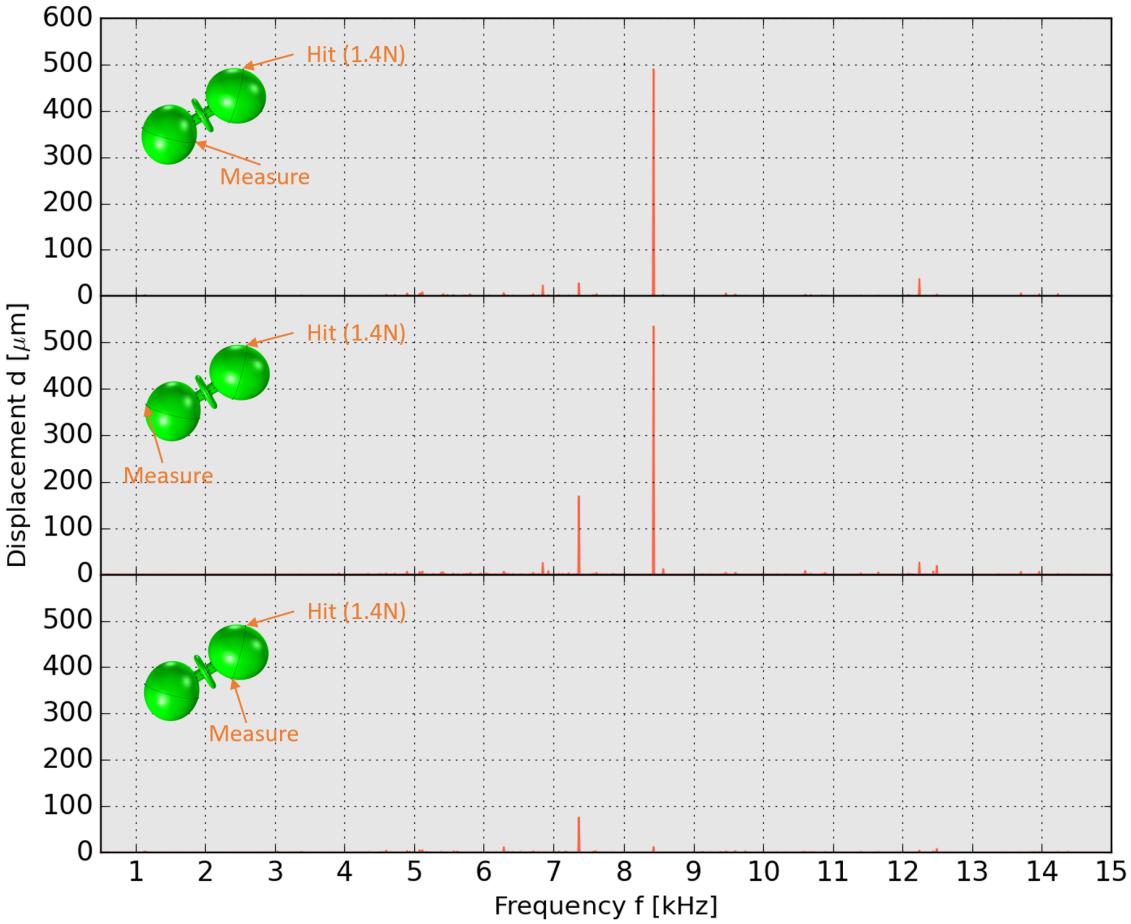

Figure 2.10.: *Simulated mechanical spectrum of the MAGO-like cavity at room temperature measured at three different positions. The mechanical resonances are excited by hitting one point of the cavity with a hammer (here with* 1.4 *N). On the left, we show the locations of the detectors and the position of the blow. In the chosen scaling, only the most dominant modes can be resolved. A better resolution of the weaker modes can be found in figure 2.9.*

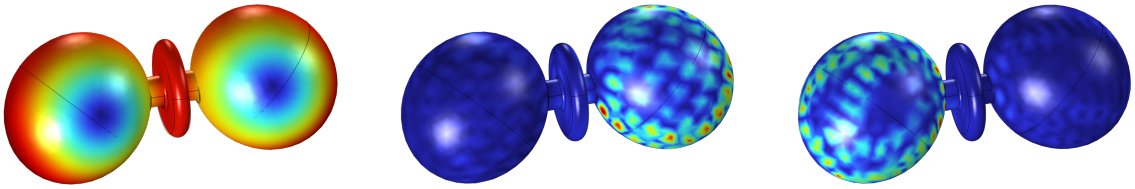

(a) $\omega_l = 0.0510\,kHz$ **(b)** $\omega_l = 7.3596\,kHz$ **(c)** $\omega_l = 8.4175\,kHz$

Figure 2.11.: *This plot shows the mechanical displacement fields for some eigenmodes of the MAGO cavity. The red colored regions are strongly displaced while the blue regions only have a small offset. We show no legend as the displacement is in arbitrary units. (a): Lowest lying mode of the spectrum. (b): Higher order mode which corresponds to a dominant resonance. (c): Higher order mode which corresponds to another dominant resonance.*

are shown in figure 2.11, together with the lowest lying mode at $\omega_l = 0.0510\,\text{kHz}$. One can see that the largest signals come from higher order modes with many nodes and anti-nodes. A detailed analysis was beyond the scope of this master thesis. The next step for future simulations would be to investigate different positions of the hammer blow as well as the detectors. The most promising locations could then be tested at the real cavity.
It should be pointed out that the step width of 10 Hz might be not sufficient to resolve very narrow resonances. This could be one reason why there are only a few very dominant modes. Furthermore, we ignored the flanges, which are also expected to have a considerable influence on the mechanical properties. In future simulations, we will therefore need to put them into account.

2.5. Future Developments

Although we work with a MAGO-like design throughout this thesis, we will briefly discuss modifications of the geometry and tuning mechanism in order to scan higher frequency regions.
In the last chapter, we saw that the tuning mechanism suggested for the MAGO cavity does only allow for relatively small scanning regions of $\Delta\omega \approx 2\,\text{kHz}$. To reach the full region of $1\,\text{kHz} - 1\,\text{GHz}$, we need a tuning mechanism that is much more efficient. However, a cavity design allowing for a scan over the full frequency region may be hard to realize which implies that we will need multiple detectors. Each detector should have a slightly modified design such that it allows for scanning a different frequencies.
Here, we show a first naive approach for such a modification. One reason why the pump and signal mode are so close in frequency space is the high symmetry of the system. The idea of coupling two identical cells leads to the required constructive interference of the corresponding eigenmodes and the formation of symmetric and antisymmetric mode fields with nearly degenerate frequencies. A first modification would be to break the symmetry by slightly deforming one cavity. The problem is that this leads to two coupled resonators with different eigenfrequencies. Hence, there is no constructive interference and a mode cannot exist in both cavities simultaneously. For the TE_{011}-mode, this means that the field vanishes in one of the cells, in fact in different ones for the pump and signal mode. Thus, the mechanical overlap as well as

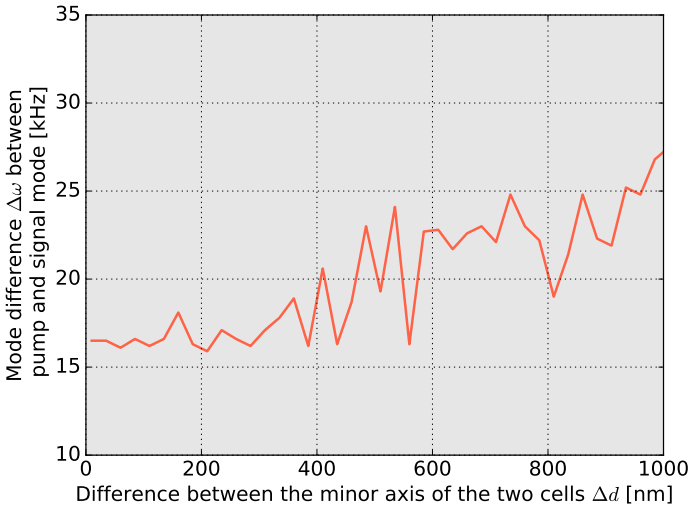

Figure 2.12.: *Parameter sweep of the difference Δd between the minor axis' of both cavities. The plot shows that already for nm-size differences, a scanning region of $\Delta\omega \approx 10\,kHz$ is possible. Note, however, that an increasing Δd automatically leads to smaller coupling coefficients since the pump and signal mode become weaker in different cells. Therefore, this approach is not able to provide large frequency differences above $\sim 50\,kHz$.*

the Gertsenshtein overlap vanish since they contain integrals over the product of both fields.
Despite these obvious disadvantages, we investigated the possibilities of very small symmetry breakings in the nm-region. Figure 2.12 shows a parameter sweep similar to the one in figure 2.8. Instead of the central tuning cell, we changed the minor axis of one cavity. The difference to the minor axis of the other cell is varied from 0 nm to 1000 nm. We see that this allows for a much larger scanning region from ~ 16 kHz to ~ 26 kHz, i.e. $\Delta\omega \approx 10$ kHz. For the small displacements assumed here, the effect of destructive interference is small, which means that the electromagnetic modes can in principle exist in both cells. However, with large symmetry breakings, the fields become weaker in one cell which means that the coupling coefficients decrease. This analysis also shows that the required precision for constructing the real MAGO cavity must be in the nm-regime.
We conclude that larger frequency differences above ~ 30 kHz between pump and signal mode are not easy to realize. Further efforts to find a better design and tuning mechanism are required. One option suggested by [3] is to add retractable fins to the cavity walls, which can be placed in regions with high field gradients. This should allow for an effective scanning over a large frequency range. Currently, the feasibility of using fins is investigated at FNAL. We point out, however, that fins add sharp features to the otherwise smooth cavity design which could considerably enhance the field emission noise. This effect is discussed in chapter 7.5.
Another possibility is to use an iris instead of the tuning cell as was done for the PACO prototype [41]. This approach adds sharp features as well, but may may also lead to a broader scanning range. Perhaps, a combination of different mechanisms might be advisable for the final experiment.

3. Cavities

This chapter introduces the basic concepts from cavity theory required for a full description of the signal in a heterodyne cavity experiment. We start with a basic introduction to cavity eigenmodes. Then we discuss the main characteristics of real cavities such as the bandwith and the quality factor. The main part of this chapter is devoted to cavity perturbation theory. Although some approaches to such a theory can be found in literature, we need a very specific one, which can only be found in a rather outdated book by Goubau et al. [48]. We will therefore describe the formalism in detail and further develop it with regard to its application in cavity theory. Finally, we discuss the displacement of the cavity shell due to an external force density, which can be done in the framework of elasticity theory.

3.1. Cavity Eigenmodes

The electromagnetic field is governed by the Maxwell equations [49]

$$\nabla \cdot \vec{E} = \frac{\rho}{\epsilon_0} \tag{3.1}$$

$$\nabla \cdot \vec{B} = 0 \tag{3.2}$$

$$\nabla \times \vec{E} = -\frac{\partial \vec{B}}{\partial t} \tag{3.3}$$

$$\nabla \times \vec{B} = \mu_0 \vec{J} + \mu_0 \epsilon_0 \frac{\partial \vec{E}}{\partial t}. \tag{3.4}$$

In vacuum ($\rho = 0$, $\vec{J} = 0$), the electric field $\vec{E}$ and magnetic field $\vec{B}$ fulfill the wave equations

$$\Delta \vec{E} = \frac{1}{c^2} \frac{\partial^2 \vec{E}}{\partial t^2} \qquad \Delta \vec{B} = \frac{1}{c^2} \frac{\partial^2 \vec{B}}{\partial t^2}. \tag{3.5}$$

In a cavity, the walls now impose boundary conditions to these partial differential equations. From general principles of electrodynamics, we found that these conditions are given by [49]

$$\vec{n} \times \vec{E}|_S = 0 \qquad \vec{n} \cdot \vec{B}|_S = 0. \tag{3.6}$$

We can solve the boundary value problem by expanding the electromagnetic field in eigensolutions of eqn. 3.5, i.e.

$$\vec{E}(t, \vec{x}) = \sum_n e_n(t) \vec{E}_n(\vec{x}) \qquad \vec{B}(t, \vec{x}) = \sum_n b_n(t) \vec{B}_n(\vec{x}). \tag{3.7}$$

The spatial eigenmodes $\vec{E}_n(\vec{x})$ are then governed by the Helmholtz equation. The full boundary value problem (BVP) can be rewritten as

$$\begin{array}{lll} \Delta \vec{E}_n(\vec{x}) + k_n^2 \vec{E}_n(\vec{x}) = 0 & \nabla \cdot \vec{E}_n = 0 & \vec{n} \times \vec{E}_n|_S = 0 \\ \Delta \vec{B}_n(\vec{x}) + k_n^2 \vec{B}_n(\vec{x}) = 0 & \nabla \cdot \vec{B}_n = 0 & \vec{n} \cdot \vec{B}_n|_S = 0 \end{array} \tag{3.8}$$

where the time-dependent eigenmodes have to fulfill the relations

$$\frac{\partial^2 e_n}{\partial t^2} = -\omega_n^2 e_n \qquad\qquad \frac{\partial^2 b_n}{\partial t^2} = -\omega_n^2 b_n$$

with $k_n = c\omega_n$. However, formulating the BVP in this way causes some problems. One can show [48, 50] that the eigensolutions $\vec{E}_n$ and $\vec{B}_n$ do not represent a complete set for all electromagnetic fields satisfying eqn. 3.6. In order to change this, we need to weaken the boundary conditions. The simplest way to do this is to require $\rho = 0$ and $\vec{J} = 0$ only on the boundaries, but not inside the cavity. We then get the modified BVP

$$\begin{array}{lll} \Delta\vec{E}_n(\vec{x}) + k_n^2\vec{E}_n(\vec{x}) = 0 & \nabla\cdot\vec{E}_n|_S = 0 & \vec{n}\times\vec{E}_n|_S \;\;= 0 \\ \Delta\vec{B}_n(\vec{x}) + k_n^2\vec{B}_n(\vec{x}) = 0 & \vec{n}\cdot\vec{B}_n|_S = 0 & \vec{n}\times(\nabla\times\vec{B}_n)|_S = 0. \end{array} \tag{3.9}$$

The solutions have some useful properties [48, 50]:

- Non-zero real eigenfunctions exist only for a discrete spectrum of real eigenvalues.
- The degree of degeneracy is always finite.
- The eigensolutions are orthogonal and normalizable.
- The eigensolutions provide a complete set for the vector space of fields $\vec{E}$, $\vec{B}$, which satisfy the boundary conditions in eqn. 3.6.

Furthermore, the solutions of BVP 3.8 are solutions of BVP 3.9 as well. We adopt the normalization convention from [3] and define

$$\int_{V_{\text{cav}}} \mathrm{d}^3x\vec{E}_n(\vec{x})\vec{E}_m(\vec{x}) = \delta_{nm}\int_{V_{\text{cav}}} \mathrm{d}^3x\vec{E}_n^2(\vec{x}) \tag{3.10}$$

$$\int_{V_{\text{cav}}} \mathrm{d}^3x\vec{B}_n(\vec{x})\vec{B}_m(\vec{x}) = \delta_{nm}\int_{V_{\text{cav}}} \mathrm{d}^3x\vec{B}_n^2(\vec{x}). \tag{3.11}$$

The time-dependent functions $e_n(t)$ and $b_n(t)$ can be expressed in this formalism for a given field $\vec{E}(t,\vec{x})$ or $\vec{B}(t,\vec{x})$ by

$$e_n(t) = \Big[\int_{V_{\text{cav}}} \mathrm{d}^3x\vec{E}_n^2(\vec{x})\Big]^{-1}\int_{V_{\text{cav}}} \mathrm{d}^3x\vec{E}(t,\vec{x})\vec{E}_n(\vec{x}) \tag{3.12}$$

$$b_n(t) = \Big[\int_{V_{\text{cav}}} \mathrm{d}^3x\vec{B}_n^2(\vec{x})\Big]^{-1}\int_{V_{\text{cav}}} \mathrm{d}^3x\vec{B}(t,\vec{x})\vec{B}_n(\vec{x}). \tag{3.13}$$

As we have already mentioned, the solution space of BVP 3.9 is larger than the solution space of BVP 3.8. One can show that the additional modes have vanishing rotation, so they are called *irrotational modes*. In Appendix B, we show that the full set of eigensolutions $\vec{E}_n$ and $\vec{B}_n$ can be separated into solenoidal and irrotational solutions. That is, they fulfill

$$\left.\begin{array}{ll} \Delta\vec{E}_n^s + k_n\vec{E}_n^s = 0 & \nabla\cdot\vec{E}_n^s = 0 \\ \Delta\vec{B}_n^s + k_n\vec{B}_n^s = 0 & \nabla\cdot\vec{B}_n^s = 0 \end{array}\right\} \quad \text{solenoidal modes}$$

$$\left.\begin{array}{ll} \Delta\vec{E}_n^r + k_n\vec{E}_n^r = 0 & \nabla\times\vec{E}_n^r = 0 \\ \Delta\vec{B}_n^r + k_n\vec{B}_n^s = 0 & \nabla\times\vec{B}_n^r = 0 \end{array}\right\} \quad \text{irrotational modes.}$$

However, it was argued in [31] that it is not possible to resonantly amplify irrotational modes. But in a heterodyne system, we can only measure a signal from modes that are resonant with an external driver. Therefore, the irrotational can be neglected and it is sufficient to consider the solenoidal modes only. We give a short proof of this statement in Appendix B.

3.2. Energy and Quality Factor

We begin with a general consideration of the electromagnetic energy in a cavity eigenmode. The details can be found in many standard textbooks like [49], we therefore only focus on the most important aspects. First, recall that the total energy $U(t)$ in a cavity is given by

$$U(t) := \frac{\epsilon_0}{2}\int_{V_{\text{cav}}} \mathrm{d}^3x\vec{E}^2(t,\vec{x}) + \frac{1}{2\mu_0}\int_{V_{\text{cav}}} \mathrm{d}^3x\vec{B}^2(t,\vec{x}), \tag{3.14}$$

where we treat $\vec{E}(t,\vec{x})$ and $\vec{B}(t,\vec{x})$ as real fields. We now want to show that the energy stored in the E-field is the same as the energy stored in the B-field for a monochromatic solenoidal cavity mode. For this purpose, we consider the monochromatic Maxwell equations

$$\nabla\times\vec{E}_n = ck_n\vec{B}_n \qquad\qquad \nabla\times\vec{B}_n = \frac{k_n}{c}\vec{E}_n. \tag{3.15}$$

Integrating the standard identity

$$\nabla\cdot(\vec{B}_n\times\vec{E}_n) = \vec{E}_n\cdot(\nabla\times\vec{B}_n) - \vec{B}_n\cdot(\nabla\times\vec{E}_n)$$

over the cavity volume and using Gauss's theorem yields

$$\int_{\partial V_{\text{cav}}}(\vec{B}_n\times\vec{E}_n)\mathrm{d}\vec{S} = \int_{V_{\text{cav}}}\mathrm{d}^3x\vec{E}_n(\nabla\times\vec{B}_n) - \int_{V_{\text{cav}}}\mathrm{d}^3x\vec{B}_n(\nabla\times\vec{E}_n).$$

The left hand side vanishes because the boundary condition (see eqn. 3.6) on the cavity surface gives $(\vec{B}_n\times\vec{E}_n)\mathrm{d}\vec{S} = (\mathrm{d}\vec{S}\times\vec{E}_n)\vec{B}_n = 0$. On the right hand side we can insert eqn. 3.15 to find

$$\epsilon_0\int_{V_{\text{cav}}}\mathrm{d}^3x\vec{E}_n^2 = \frac{1}{\mu_0}\int_{V_{\text{cav}}}\mathrm{d}^3x\vec{B}_n^2,$$

which proves the statement. Finally, we can express the energy as

$$U_n(t) = U_n = \frac{\epsilon_0}{2}\int_{V_{\text{cav}}}\mathrm{d}^3x\vec{E}_n^2(\vec{x}) = \frac{1}{2\mu_0}\int_{V_{\text{cav}}}\mathrm{d}^3x\vec{B}_n^2(\vec{x}), \tag{3.16}$$

where we used $e_n^2(t) + b_n^2(t) = 1$. Note that the energy is now time-independent, so the calculations are consistent. Using U_n, we can write the normalizations 3.10 and 3.11 as

$$\int_{V_{\text{cav}}}\mathrm{d}^3x\varepsilon_0\vec{E}_n(\vec{x})\vec{E}_m(\vec{x}) = 2U_n\delta_{nm} = \int_{V_{\text{cav}}}\mathrm{d}^3x\frac{1}{\mu_0}\vec{B}_n(\vec{x})\vec{B}_m(\vec{x}). \tag{3.17}$$

The time-modes in eqn. 3.12 and 3.13 can be recast in this formalism as

$$e_n(t) = \frac{\varepsilon_0}{2U_n}\int_{V_{\text{cav}}}\mathrm{d}^3x\vec{E}(t,\vec{x})\vec{E}_n(\vec{x}) \tag{3.18}$$

$$b_n(t) = \frac{1}{2U_n\mu_0}\int_{V_{\text{cav}}}\mathrm{d}^3x\vec{B}(t,\vec{x})\vec{B}_n(\vec{x}). \tag{3.19}$$

If we consider an open system, it should be noted that the energy becomes in general time-dependent and the time-average of $U_n(t)$ can be expressed (using the adiabatic approximation $\langle e_n^2(t)\rangle \approx \langle b_n^2(t)\rangle$) as

$$\langle U_n(t)\rangle = 2U_n\langle e_n^2(t)\rangle = 2U_n\langle b_n^2(t)\rangle.$$

We need this generalized case because due to ohmic power losses through the cavity walls, the average energy U_n is not constant in time. The quality, i.e., how well the energy can be stored, is described by the quality factor Q_n defined by [49]

$$Q_n := \omega_n \frac{\text{stored energy in mode n}}{\text{power loss per cycle in mode n}}. \tag{3.20}$$

This leads to a standard decay law

$$\frac{\mathrm{d}U_n(t)}{\mathrm{d}t} = \frac{\omega_n}{Q_n} U_n(t) \tag{3.21}$$

for the mode n. The left hand side is nothing but the signal power of the mode. If we pump the cavity with an external oscillator, both sides become independent and we can write

$$P_{\text{sig}} = \frac{\omega_n}{Q_n} \langle U_n(t) \rangle = \frac{\omega_n}{Q_n} 2U_n \langle b_n^2(t) \rangle \tag{3.22}$$

However, it is also useful to consider the general solution $U_n(t) = U_n e^{-\frac{\omega_n}{Q_n} t}$ to eqn. 3.21. Using eqn. 3.14, it can be written in terms of the E- and B-field, i.e.

$$\vec{E}_n'(\vec{x}, t) = \vec{E}_n(\vec{x}, t) e^{-\frac{\omega_n}{2Q_n} t} \qquad \vec{B}_n'(\vec{x}, t) = \vec{B}_n(\vec{x}, t) e^{-\frac{\omega_n}{2Q_n} t}.$$

The equations can be solved for the unprimed fields and then substituted into eqn. 3.5. We pick the B-field and consider the result

$$\Delta \vec{B}_n' = \frac{1}{c^2} \frac{\partial^2 \vec{B}_n'}{\partial t^2} + \frac{1}{c^2} \frac{\omega_n}{Q_n} \frac{\partial \vec{B}_n'}{\partial t}$$

where we have assumed a large quality factor such that terms of order $\mathcal{O}(\omega_n^2/Q_n^2)$ can be neglected. Now, the modes can be expanded using eqn. 3.7. It is further possible to apply eqn. 3.9 since the spatial dependence for the primed field has not changed. The result for the time-dependent mode $b_n(t)$ then reads

$$\ddot{b}_n + \frac{\omega_n}{Q_n} \dot{b}_n + \omega_n^2 b_n = 0 \tag{3.23}$$

where we have dropped the prime as we will mainly work with the damped fields throughout this thesis.

We will need later that quality factors can be separated into different components. For instance, if the cavity is a closed system, than the signal mode has only one quality factor Q_1. When we couple a readout system with the signal mode, there is an additional loss determined by a coupling quality factor Q_{cpl}. Together with the internal quality factor Q_{int}, the full quality factor Q_1 can then be written as [3]

$$\frac{1}{Q_1} = \frac{1}{Q_{\text{cpl}}} + \frac{1}{Q_{\text{int}}}. \tag{3.24}$$

Sometimes it is useful to choose $Q_{\text{cpl}} \approx Q_{\text{int}}$, which is called *critical coupling*. In other cases it is better to use $Q_{\text{cpl}} \ll Q_{\text{int}}$, which we denote as *overcoupling*. We will give more details in chapter 7.

3.3. Power Spectral Densities

In many cases, it is useful to consider the frequency dependence of a signal, which is represented by the Power Spectral Density (PSD) [51]. Here we give a brief overview of the formalism since we want to derive PSD's for the signals and noises later in the thesis.
In general, the PSD of a function f is related to its time average via

$$\langle f^2(t)\rangle = \frac{1}{(2\pi)^2}\int \mathrm{d}\omega S_f(\omega), \tag{3.25}$$

where we have adopted the conventions from [3, 43]. Furthermore, the time average can be expressed in terms of the autocorrelation function

$$G_f(\tau) := \lim_{T\to\infty}\frac{1}{T}\int_0^T \mathrm{d}t f(t)f^*(t-\tau)$$

since $\langle f^2(t)\rangle = G(0)$. In general, we can define

$$G(t-t') = \langle f(t)f^*(t')\rangle.$$

The autocorrelation function and PSD are related by the *Wiener-Khinchin theorem*, which states that each is the Fourier transform of the other. We can therefore write

$$S_f(\omega) = 2\pi\int \mathrm{d}\tau e^{-i\omega\tau}G(\tau). \tag{3.26}$$

Another important quantity is the ensemble average $\langle f(\omega)f^*(\omega')\rangle$ defined as the fourier transformation of $G(t-t')$. It is related to the PSD via

$$\langle f(\omega)f^*(\omega')\rangle = \delta(\omega-\omega')S_f(\omega).$$

We now want to discuss some special cases using this formalism. Consider two functions $f(t) = e^{i\omega_1 t}$ and $g(t) = e^{i\omega_2 t}$. The correlation between them can be quantified by

$$\langle f(\tau)g^*(\tau)\rangle = \lim_{T\to\infty}\frac{1}{T}\int_0^T \mathrm{d}t f(t)g^*(t-\tau) = \begin{cases} e^{i\omega_1\tau} & \omega_1 = \omega_2 \\ 0 & \omega_1 \neq \omega_2 \end{cases}.$$

We see that two periodic functions are correlated only when they have overlapping spectra. This results in some useful rules for the PSD. First, consider a function $f(\omega) = h(\omega)g(\omega)$ with periodic part $g(\omega)$ and a non-periodic part $h(\omega)$. The PSD can be than written as

$$S_f(\omega) = |h(\omega)|^2 S_g(\omega). \tag{3.27}$$

We can further show that the PSD of a function $f(\omega) = f_1(\omega) + f_2(\omega)$ with two uncorrelated functions $f_1(\omega)$ and $f_2(\omega)$ in the sense that their spectra do not intersect can be written as

$$S_f(\omega) = S_{f_1}(\omega) + S_{f_2}(\omega). \tag{3.28}$$

Finally, we need the PSD of the function $f(\omega) = e^{i\omega_0 t}$, which can be calculated using eqn. 3.26. The result is, as expected, given by

$$S_f(\omega) = 4\pi^2\delta(\omega-\omega_0). \tag{3.29}$$

One main goal of this thesis is to derive a PSD for $b_n(t)$. Once it has been found, the signal power can be easily calculated with 3.22. This relation can be also written in the form

$$P_{\text{sig}} = \frac{1}{(2\pi)^2}\int \mathrm{d}\omega S_{\text{sig}}(\omega) = \frac{1}{2\pi^2}\frac{\omega_n}{Q_{\text{cpl}}}U_n \int \mathrm{d}\omega S_{b_n}(\omega). \tag{3.30}$$

such that $S_{\text{sig}}(\omega) := 2U_n\omega_n/Q_{\text{cpl}}S_{b_n}(\omega)$. Note that we have to take the coupling quality factor here since the signal power corresponds exactly to the energy loss through the readout coupling.

3.4. Cavity Perturbation Theory

When a GW propagates through a cavity, it changes the boundary conditions of the electromagnetic field. The eigenmodes of the deformed cavity are in general different from the eigenmodes of the unperturbed one. However, the GW strains are very small ($\lesssim \mathcal{O}(10^{-21})$), so cavity perturbation theory can be applied. In other words, we express the perturbed modes as series expansions of the unperturbed modes. We are then interested in the resulting overlap given by the expansion coefficients. An important result of this procedure is that the perturbed mode $\vec{E}'_n$ appears to be strongly coupled to its unperturbed counterpart $\vec{E}_n$, but also has contributions from other modes $\vec{E}_m$ with $m \neq n$.
There are several approaches to find such mode expansions. We will use the method given in [48] as it is consistent with the method applied in [5]. The main idea is to find an expression for the deformed boundary conditions at the position of the unperturbed shell. The advantage of this approach is that we do not have to deal with a perturbed volume V'_{cav} and can therefore work with V_{cav} throughout the calculation.
We will discuss the formalism in detail here. The main reason is that [48] is a rather old and outdated book, which further contains some inconsistencies. We present the arguments in a new and improved way using a modern notation.

3.4.1. The Perturbed Boundary Condition

The unperturbed shell should have surface S, while the perturbed shell should have surface S'. We note that the electromagnetic field in both cavities is governed by the BVP's

$$\begin{aligned} \nabla\times\vec{E}_n &= ck_n\vec{B}_n & \nabla\times\vec{E}'_n &= ck'_n\vec{B}'_n \\ \nabla\times\vec{B}_n &= \frac{k_n}{c}\vec{E}_n & \nabla\times\vec{B}'_n &= \frac{k'_n}{c}\vec{E}'_n \\ \vec{n}\times\vec{E}_n|_S &= 0 & \vec{n}'\times\vec{E}'_n|_{S'} &= 0. \end{aligned} \tag{3.31}$$

We will use $\omega_n = ck_n$ instead of k_n from now on. Our goal is to find the equivalent of the boundary condition $\vec{n}'\times\vec{E}'_n|_{S'} = 0$ on S. Since S is supposed to be a (at least piece-wise) smooth manifold, we can parameterize it with two parameters λ_1 and λ_2. We then define two curves

$$\begin{aligned} \vec{u}_1 &:= \vec{u}_{\lambda_2}(\lambda_1) := \vec{S}(\lambda_1,\lambda_2)|_{\lambda_2 \text{ fixed}} \\ \vec{u}_2 &:= \vec{u}_{\lambda_1}(\lambda_2) := \vec{S}(\lambda_1,\lambda_2)|_{\lambda_1 \text{ fixed}} \end{aligned}$$

such that the tangential vectors

$$\vec{t}_1 := \frac{\partial \vec{u}_1}{\partial \lambda_1} \qquad \vec{t}_2 = \frac{\partial \vec{u}_2}{\partial \lambda_2}$$

define a right-handed orthonormal system $(\vec{t}_1, \vec{t}_2, \vec{n})$, where $\vec{n}$ is the surface normal. The displacement is described by $\Delta(\vec{x})$, which gives the absolute value of the shell deformation at a point $\vec{x}$ on the surface. By convention, it is $\Delta < 0$ for inward and $\Delta > 0$ for outward deformations. Throughout the following discussion, we will assume that $|\Delta(\vec{x})| \ll 1$.
We start by going along the infinitesimal distances

$$\mathrm{d}\vec{u}_1 = \vec{t}_1 \mathrm{d}\lambda_1 \qquad \mathrm{d}\vec{u}_2 = \vec{t}_2 \mathrm{d}\lambda_2$$

on the unperturbed surface S. We then move around a closed way using $\vec{n}\Delta$ to jump on the perturbed surface S'. The path for both inward and outward deformation is shown in figure 3.1. We consider the surface elements within the path, which are given by

$$\mathrm{d}\vec{A}_1 = \pm \vec{t}_2 \mathrm{d}\lambda_1 \Delta \qquad \mathrm{d}\vec{A}_2 = \mp \vec{t}_1 \mathrm{d}\lambda_2 \Delta$$

Note that the upper sign corresponds to the inward direction and the lower sign to the outward direction. The key idea now is to apply Stokes theorem. It is useful to look at fig. 3.1 to track the signs correctly. Weighting the surface elements $\mathrm{d}\vec{A}_1$ and $\mathrm{d}\vec{A}_2$ with $\nabla \times \vec{E}'_n$ leads to

$$\begin{aligned}
\nabla \times \vec{E}'_n \cdot \mathrm{d}\vec{A}_1 &= \pm \nabla \times \vec{E}'_n \cdot \vec{t}_2 \Delta \mathrm{d}\lambda_1 \\
&= \pm \vec{E}'_n \Delta \vec{n} \mp \vec{E}'_n \Delta \vec{n} \mp \mathrm{d}\lambda_1 \frac{\partial}{\partial \lambda_1} (\vec{E}'_n \vec{n} \Delta) \mp \vec{E}'_n \vec{t}_1 \mathrm{d}\lambda_1 \\
&= \mp \vec{E}'_n \vec{t}_1 \mathrm{d}\lambda_1 \mp \mathrm{d}\lambda_1 \frac{\partial}{\partial \lambda_1} (\vec{E}'_n \vec{n} \Delta)
\end{aligned}$$

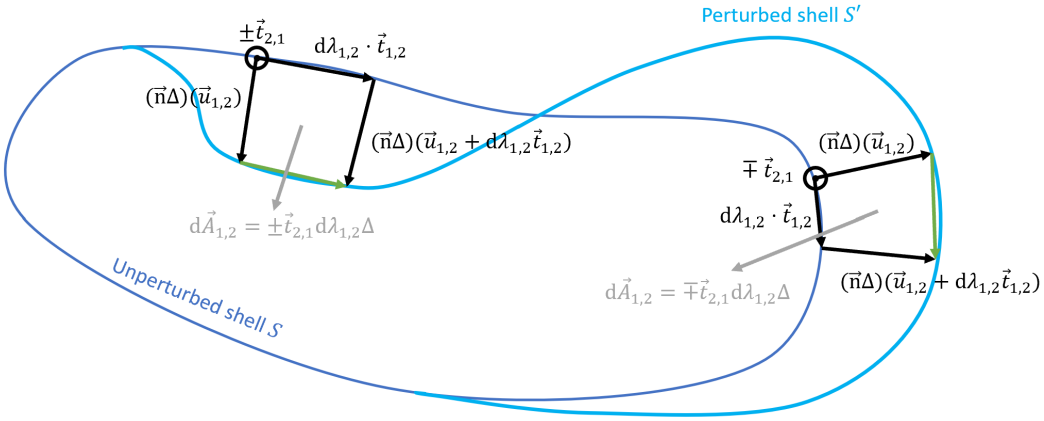

Figure 3.1.: *Construction of the boundary conditions for the perturbed mode. The idea is to use the area elements $d\vec{A}_{1,2}$, Stoke's theorem and that $\vec{E}'_n$ vanishes on the perturbed shell to find an expression for $\vec{n} \times \vec{E}'_n|_S$ on the unperturbed shell. This sketch should help to track the correct signs for inward/outward deformation and $\vec{t}_1/\vec{t}_2$-direction respectively.*

$$\begin{aligned}\nabla \times \vec{E}_n' \cdot \mathrm{d}\vec{A}_2 &= \mp \nabla \times \vec{E}_n' \cdot \vec{t}_1 \Delta \mathrm{d}\lambda_2 \\ &= \pm \vec{E}_n' \Delta \vec{n} \mp \vec{E}_n' \Delta \vec{n} \mp \mathrm{d}\lambda_2 \frac{\partial}{\partial \lambda_2}(\vec{E}_n' \vec{n} \Delta) \mp \vec{E}_n' \vec{t}_2 \mathrm{d}\lambda_2 \\ &= \mp \vec{E}_n' \vec{t}_2 \mathrm{d}\lambda_2 \mp \mathrm{d}\lambda_2 \frac{\partial}{\partial \lambda_2}(\vec{E}_n' \vec{n} \Delta),\end{aligned}$$

where we have tailor expanded $(\vec{E}_n' \vec{n} \Delta)(\vec{u}_{1,2} + \mathrm{d}\lambda_{1,2} \vec{t}_{1,2})$ and used that $\vec{E}_n'|_S' = 0$ on the perturbed surface (see fig. 3.1). By eliminating $\mathrm{d}\lambda_1$ and $\mathrm{d}\lambda_2$, we find

$$\begin{aligned}\vec{E}_n' \cdot \vec{t}_1 &= -\nabla \times \vec{E}_n' \cdot \vec{t}_2 \Delta - \frac{\partial}{\partial \lambda_1}(\vec{E}_n' \vec{n} \Delta) \\ \vec{E}_n' \cdot \vec{t}_2 &= \nabla \times \vec{E}_n' \cdot \vec{t}_1 \Delta - \frac{\partial}{\partial \lambda_2}(\vec{E}_n' \vec{n} \Delta).\end{aligned}$$

These results can be now combined to

$$\begin{aligned}\vec{E}_n' &= (\vec{E}_n' \vec{t}_1) \cdot \vec{t}_1 + (\vec{E}_n' \vec{t}_2) \cdot \vec{t}_2 + (\vec{E}_n' \vec{n}) \cdot \vec{n} \\ &= -(\nabla \times \vec{E}_n' \vec{t}_2 \Delta) \cdot \vec{t}_1 + (\nabla \times \vec{E}_n' \vec{t}_1 \Delta) \cdot \vec{t}_2 \\ &\quad - \frac{\partial}{\partial \lambda_1}(\vec{E}_n' \vec{n} \Delta) \cdot \vec{t}_1 - \frac{\partial}{\partial \lambda_2}(\vec{E}_n' \vec{n} \Delta) \cdot \vec{t}_2 + (\vec{E}_n' \vec{n}) \cdot \vec{n}.\end{aligned}$$

On the shell of the unperturbed cavity this expression reads

$$\vec{E}_n'|_S = \vec{n} \times (\nabla \times \vec{E}_n') \Delta|_S - \nabla(\vec{E}_n' \vec{n} \Delta)|_S + (\vec{E}_n' \vec{n}) \cdot \vec{n}|_S,$$

where we used the standard gradient in the coordinate system $(\vec{t}_1,\ \vec{t}_2,\ \vec{n})$ together with the identity $\vec{a} \times (\vec{b} \times \vec{c}) = \vec{b} \cdot (\vec{a} \cdot \vec{c}) - \vec{c} \cdot (\vec{a} \cdot \vec{b})$. Inserting the monochromatic Maxwell equations 3.15 finally yields the perturbed version of the boundary condition $\vec{n} \times \vec{E}_n|_S = 0$. The result is

$$\vec{n} \times \vec{E}_n'|_S = \Delta(\omega_n \vec{B}_n \times \vec{n}) \times \vec{n}|_S + \nabla(\vec{E}_n \vec{n} \Delta) \times \vec{n}|_S,$$

so the perturbed electric field does not vanish in the unperturbed shell. This will now help us to find a series expansion for $\vec{E}_n'$ (or $\vec{B}_n'$) in terms of $\vec{E}_n$ (or $\vec{B}_n$). Note that we have dropped the primes of the right hand side as we assumed Δ to be small so we can only consider leading order terms.

3.4.2. Solving the Boundary Value Problem

According to the general idea of perturbation theory, we decompose the perturbed eigenmodes as

$$\begin{aligned}\vec{E}_n' &= \vec{E}_n + \sigma \vec{E}_n^{(1)} + \mathcal{O}(\sigma^2) \\ \vec{B}_n' &= \vec{B}_n + \sigma \vec{B}_n^{(1)} + \mathcal{O}(\sigma^2) \\ \omega_n' &= \omega_n + \sigma \omega_n^{(1)} + \mathcal{O}(\sigma^2).\end{aligned}$$

Substituting this into the perturbed BVP and using the unperturbed BVP (see eqn. 3.31), we obtain a BVP for the first order corrections $\sigma \vec{E}_n^{(1)}$ and $\sigma \vec{B}_n^{(1)}$. It can be written as

$$\nabla \times \sigma \vec{E}_n^{(1)} - \omega_n \sigma \vec{B}_n^{(1)} = \sigma \omega_n^{(1)} \vec{B}_n \tag{3.32}$$

$$\nabla \times \sigma \vec{B}_n^{(1)} - \frac{\omega_n}{c^2} \sigma \vec{E}_n^{(1)} = \frac{\sigma \omega_n^{(1)}}{c^2} \vec{E}_n \tag{3.33}$$

$$\vec{n} \times \sigma \vec{E}_n^{(1)}|_S = \omega_n \vec{V}_n|_S. \tag{3.34}$$

where again we consider only leading order terms in Δ and σ. To abbreviate notation, we have defined

$$\vec{V}_n := \Delta(\vec{B}_n \times \vec{n}) \times \vec{n}|_S + \frac{1}{\omega_n}\nabla(\vec{E}_n \vec{n}\Delta) \times \vec{n}|_S \tag{3.35}$$

here. We can now expand the first order corrections in terms of the unperturbed modes, i.e.

$$\sigma\vec{E}_n^{(1)} = \sum_m \alpha_{nm}\vec{E}_m \tag{3.36}$$

$$\sigma\vec{B}_n^{(1)} = \sum_m \beta_{nm}\vec{B}_m \tag{3.37}$$

$$\sigma\omega_n^{(1)} = \sum_m \kappa_{nm}\omega_m. \tag{3.38}$$

The remaining task then is to find the coefficients α_{nm}, β_{nm} and κ_{nm}. We start by integrating equation 3.32 over $\vec{B}_m$ such that

$$\int_{V_{\text{cav}}} \mathrm{d}^3x\vec{B}_m \cdot \nabla \times \sigma\vec{E}_n^{(1)} - \omega_n \int_{V_{\text{cav}}} \mathrm{d}^3x\vec{B}_m \cdot \sigma\vec{B}_n^{(1)} = \sigma\omega_n^{(1)}\delta_{nm}\int_{V_{\text{cav}}} \mathrm{d}^3x\vec{B}_n^2. \tag{3.39}$$

Equivalently, we can integrate equation 3.33 over $\vec{E}_m$, leading to a similar expression with $\vec{B}$ and $\vec{E}$ exchanged. Using standard nabla identities and Gauss's law, we can rewrite the first integral of eqn. 3.39 as

$$\int_{V_{\text{cav}}} \mathrm{d}^3x\vec{B}_m \cdot \nabla \times \sigma\vec{E}_n^{(1)} = -\int_{\partial V_{\text{cav}}} \mathrm{d}\vec{S}(\vec{B}_m \times \sigma\vec{E}_n^{(1)}) + \int_{V_{\text{cav}}} \mathrm{d}^3x\sigma\vec{E}_n^{(1)}\nabla \times \vec{B}_m$$

and similarly for the B-field. To evaluate the surface integral, we can use the boundary conditions in 3.31 and 3.34. Note that there is now a difference between the E-field and B-field because

$$\mathrm{d}\vec{S}(\vec{B}_m \times \sigma\vec{E}_n^{(1)}) = \vec{n} \cdot (\vec{B}_m \times \sigma\vec{E}_n^{(1)})\mathrm{d}S = \vec{B}_m \cdot (\sigma\vec{E}_n^{(1)} \times \vec{n})\mathrm{d}S = -\omega_n\vec{B}_m \cdot \vec{V}_n\mathrm{d}S$$
$$\mathrm{d}\vec{S}(\vec{E}_m \times \sigma\vec{B}_n^{(1)}) = \vec{n} \cdot (\vec{E}_m \times \sigma\vec{B}_n^{(1)})\mathrm{d}S = \sigma\vec{B}_n^{(1)} \cdot (\vec{n} \times \vec{E}_m)\mathrm{d}S = 0.$$

With these results and using eqn. 3.31, we can write equation 3.39 as

$$\begin{aligned}
\frac{\omega_m}{c^2}\int_{V_{\text{cav}}} \mathrm{d}^3x\sigma\vec{E}_n^{(1)}\vec{E}_m - \omega_n\int_{V_{\text{cav}}} \mathrm{d}^3x\sigma\vec{B}_n^{(1)} \cdot \vec{B}_m& \\
= \sigma\omega_n^{(1)}\delta_{nm}\int_{V_{\text{cav}}} \mathrm{d}^3x\vec{B}_n^2 - \omega_n\int_{\partial V_{\text{cav}}} \mathrm{d}S\vec{B}_m \cdot \vec{V}_n& \\
\omega_m\int_{V_{\text{cav}}} \mathrm{d}^3x\sigma\vec{B}_n^{(1)}\vec{B}_m - \frac{\omega_n}{c^2}\int_{V_{\text{cav}}} \mathrm{d}^3x\sigma\vec{E}_n^{(1)}\vec{E}_m& \\
= \frac{\sigma\omega_n^{(1)}}{c^2}\delta_{nm}\int_{V_{\text{cav}}} \mathrm{d}^3x\vec{E}_n^2.&
\end{aligned}$$

where we wrote the expression for the B-field as well. The next step is to insert the expansions eqn. 3.36-3.37. We can use eqn. 3.17 to simplify the notation and arrive at

$$\frac{\omega_m}{c^2}\alpha_{nm}\frac{2U_m}{\epsilon_0} - \omega_n\beta_{nm}2\mu_0U_m = \delta_{nm}\sigma\omega_n^{(1)}2\mu_0U_m + \frac{2U_m}{\epsilon_0}\frac{\omega_n}{c^2}\mathcal{C}_{nm} \tag{3.40}$$

$$\omega_m\beta_{nm}2\mu_0U_m - \frac{\omega_n}{c^2}\alpha_{nm}\frac{2U_m}{\epsilon_0} = \frac{\sigma\omega_n^{(1)}}{c^2}\delta_{nm}\frac{2U_n}{\epsilon_0}, \tag{3.41}$$

where a new coupling coefficient is defined by

$$\mathcal{C}_{nm} := -\frac{c^2}{2U_m}\int_{\partial V_{\text{cav}}} \mathrm{d}S\epsilon_0 \vec{B}_m \vec{V}_n. \tag{3.42}$$

To find the coefficients α_{nm}, β_{nm} and κ_{nm}, we have to solve eqn. 3.40 and 3.41. For this, we have to distinguish between the case $n = m$ and $n \neq m$. We start with the latter, which yields

$$\alpha_{nm} = \frac{\omega_m\omega_n}{\omega_m^2 - \omega_n^2}\mathcal{C}_{nm} \tag{3.43}$$

$$\beta_{nm} = \frac{\omega_n^2}{\omega_m^2 - \omega_n^2}\mathcal{C}_{nm}. \tag{3.44}$$

The case $n = m$ is a little more involved. From eqn. 3.40 and 3.41, we directly find

$$\sigma\omega_n^{(1)} = -\frac{1}{2}\omega_n\mathcal{C}_{nn}.$$

This leads to a solution for κ_{nm} and an interim result for α_{nn} and β_{nn}. More precisely, we have

$$\kappa_{nm} = -\frac{1}{2}\delta_{nm}\mathcal{C}_{nm}$$

$$\alpha_{nn} = \beta_{nn} + \frac{1}{2}\mathcal{C}_{nn}.$$

However, we have to fix another degree of freedom to get a final result for the remaining coefficients. That is because we have not yet chosen a normalization for the perturbed fields. An appropriate choice is to define

$$\int_{V_{\text{cav}}} \mathrm{d}^3x\vec{E}_n'^2 := \frac{2U_n}{\epsilon_0} = \int_{V_{\text{cav}}} \mathrm{d}^3x\vec{E}_n^2. \tag{3.45}$$

By observing that

$$\frac{2U_n}{\epsilon_0} = \int_{V_{\text{cav}}} \mathrm{d}^3x(\vec{E}_n + \sigma\vec{E}_n^{(1)})^2 = (1 + 2\alpha_{nn})\frac{2U_n}{\epsilon_0},$$

we find that the diagonal coefficients are asymmetric and given by

$$\alpha_{nn} = 0 \qquad\qquad \beta_{nn} = -\frac{1}{2}\mathcal{C}_{nn}. \tag{3.46}$$

This seems to be a contradiction when we consider equation 3.17. It should be noted, however, that the boundary condition for the unperturbed mode (eqn. 3.6) is no longer valid and we have to use equation 3.34 instead. Repeating the calculation in chapter 3.2 would yield the same result as given in equation 3.46.
Finally, we write the perturbed solutions in terms of the time modes $e_n(t)$ and $b_n(t)$. Thus, substituting the expansions 3.36-3.38 into eqn. 3.18 and 3.19, we end up with

$$e_n'(t) = e_n(t) + \sum_{m\neq n} \alpha_{nm}\frac{U_m}{U_n}e_m(t) \qquad\qquad \alpha_{nm} = \frac{\omega_n\omega_m}{\omega_m^2 - \omega_n^2}\mathcal{C}_{nm} \tag{3.47}$$

$$b_n'(t) = b_n(t) - \frac{1}{2}\mathcal{C}_{nn}b_n(t) + \sum_{m\neq n} \frac{U_m}{U_n}\beta_{nm}b_m(t) \qquad\qquad \beta_{nm} = \frac{\omega_n^2}{\omega_m^2 - \omega_n^2}\mathcal{C}_{nm} \tag{3.48}$$

$$\omega_n' = \omega_n - \frac{1}{2}\omega_n\mathcal{C}_{nn}. \tag{3.49}$$

The remaining task now is to determine the connection coefficient $\mathcal{C}_{nn}$.

3.4.3. The Connection Coefficient

We return to eqn. 3.35 and eqn. 3.42, which define the connection coefficient $\mathcal{C}_{nm}$. The full expression reads

$$\mathcal{C}_{nm} = -\frac{c^2}{2U_m}\int_{\partial V_{\text{cav}}} \mathrm{d}S\epsilon_0\vec{B}_m\Big[(\Delta\vec{B}_n\times\vec{n})\times\vec{n} + \frac{1}{\omega_n}\nabla(\vec{n}\vec{E}_n\Delta)\times\vec{n}\Big].$$

We can write this in a shorter form by using the boundary condition $\vec{B}_n\cdot\vec{n}|_S = 0$ for the unperturbed cavity. The left integral can be then written as

$$\int_{\partial V_{\text{cav}}} \mathrm{d}S\cdot\vec{B}_m(\vec{B}_n\times\vec{n})\times\vec{n}\Delta = -\int_{\partial V_{\text{cav}}} \mathrm{d}S\cdot\vec{B}_m\vec{B}_n\Delta$$

using the triple product expansion. For the right integral, we use that $\mathrm{d}\vec{S} = \vec{n}\mathrm{d}S$ together with common nabla identities and the Helmholtz equation to find

$$\begin{aligned}\int_{\partial V_{\text{cav}}} &\mathrm{d}S\cdot\epsilon_0\vec{B}_m\nabla(\vec{n}\vec{E}_n\Delta)\times\vec{n}\\ &= \omega_m\int_{\partial V_{\text{cav}}}\mathrm{d}S\cdot\frac{\epsilon_0}{c^2}\Delta(\vec{n}\vec{E}_n)(\vec{n}\vec{E}_m) - \int_{\partial V_{\text{cav}}}\mathrm{d}\vec{S}\cdot\nabla\times((\vec{n}\vec{E}_n)\vec{B}_m\Delta).\end{aligned}$$

Using the boundary condition $\vec{E}_{n,m}\times\vec{n}|_S = 0$, we can write in the first integral

$$(\vec{n}\cdot\vec{E}_n)(\vec{n}\cdot\vec{E}_m)|_S = \vec{E}_n\cdot\vec{E}_m|_S.$$

The second integral vanishes due to Stoke's law. Combining all results leads to the relation

$$\mathcal{C}_{nm} = \frac{1}{2U_m}\int_{\partial V_{\text{cav}}}\mathrm{d}S\cdot\Delta\Big[\frac{1}{\mu_0}\vec{B}_n\vec{B}_m - \frac{\omega_m}{\omega_n}\epsilon_0\vec{E}_n\vec{E}_m\Big].$$

Note that in cases where $\omega_m\approx\omega_n$, we get the simplified form

$$\mathcal{C}_{nm} \approx \frac{1}{2U_m}\int_{\partial V_{\text{cav}}}\mathrm{d}S\cdot\Delta\Big[\frac{1}{\mu_0}\vec{B}_n\vec{B}_m - \epsilon_0\vec{E}_n\vec{E}_m\Big]. \tag{3.50}$$

3.5. Wall Deformation

A passing GW changes the spacetime and therefore also the boundary conditions of an electromagnetic resonator. This deformation is usually vary small ($\lesssim\mathcal{O}(10^{-21}\,\mathrm{m})$), so we can describe the physical influence within cavity perturbation theory.
To describe the mechanical deformation properly, we need the framework of elasticity theory [52, 53]. In earlier studies about heterodyne gravitational wave experiments [5, 38], this formalism was already investigated in detail. We start with the differential equation governing the displacement field $\vec{u}(t,\vec{x})$ of an isotropic elastic solid under the influence of an external force density $\vec{f}(t,\vec{x})$. It is given by

$$\rho(\vec{x})\frac{\partial\vec{u}}{\partial t} - (\lambda+\mu)\nabla(\nabla\vec{u}) - \mu\Delta\vec{u} = \vec{f}(t,\vec{x}), \tag{3.51}$$

where $\rho(\vec{x})$ denotes the material density and λ and μ the materials first and second Lamé-coefficients [38]. More details on the derivation of this formula can be found in Appendix A. Assuming that the cavity walls are initially at rest, i.e. $\vec{u}(t,\vec{x}) = \partial_t \vec{u}(0,\vec{x})$, we can use the expansion theorem [5, 54] and make a seperation ansatz of the form

$$\vec{u}(t,\vec{x}) = \sum_{l=1}^{\infty} \vec{\xi}_l(\vec{x}) q_l(t). \tag{3.52}$$

We use the convention that the time-dependent modes $q_l(t)$ carry the amplitude of the wall displacement and the spatial modes $\vec{\xi_l}(\vec{x})$ are normalized such that

$$\int_{V_{\text{cav}}} \mathrm{d}^3x \vec{\xi_l}(\vec{x})\vec{\xi_k}(\vec{x})\rho(\vec{x}) = M\delta_{kl}, \tag{3.53}$$

where M is the cavity mass. Applying the separation ansatz to equation 3.51, it splits into an eigenvalue equation

$$\omega_l^2 \rho(\vec{x})\vec{\xi_l}(\vec{x}) + (\lambda+\mu)\nabla(\nabla\vec{\xi_l}(\vec{x})) + \mu\Delta\vec{\xi_l}(\vec{x}) = 0. \tag{3.54}$$

and a differential equation governing the response to an external force given by

$$\ddot{q}_l(t) + \omega_l^2 q_l(t) = \frac{f_l(t)}{M}. \tag{3.55}$$

Here, $f_l(t)$ is the generalized force density

$$f_l(t) := \int_{V_{\text{cav}}} \mathrm{d}^3x \vec{f}(t,\vec{x})\vec{\xi_l}(\vec{x}). \tag{3.56}$$

So far, the external force $\vec{f}(t,\vec{x})$ is not specified. In chapter 4.5, we will identify it with the tidal force of a passing GW.
It will be useful later to consider the Lagrangian of the mode $q_l(t)$, which is simply the harmonic oscillator

$$L_{\text{HO}} = \sum_l \left(\frac{1}{2}M\dot{q}_l^2(t) - \frac{1}{2}M\omega_l^2 q_l^2(t) + q_l(t)f_l(t)\right). \tag{3.57}$$

Note that eqn. 3.55 and 3.57 do not properly describe the system as we also have to consider damping effects due to mechanical losses. Corresponding dissipative terms have to be inserted by hand. When we add an additional damping term according to eqn. 3.23 that contains a mechanical quality factor Q_l defined as in eqn. 3.20, it follows

$$\ddot{q}_l(t) + \frac{\omega_l}{Q_l}\dot{q}_l(t) + \omega_l^2 q_l(t) = \frac{f_l(t)}{M}. \tag{3.58}$$

Finally, we consider again the connection coefficient 3.50. In the language of elasticity theory, we can identify $\mathrm{d}S\cdot\Delta = \mathrm{d}\vec{S}\cdot\vec{u}(t,\vec{x})$, so $\mathcal{C}_{nm}$ describes the coupling between the mechanical and the electromagnetic modes. Note that this has to be treated carefully, since we assumed a constant deformation of the cavity in chapter 3.4 [5]. However, the frequency of the mechanical mode is much smaller than the frequency of the electromagnetic mode. Therefore, we can use the adiabatic theorem, i.e. the electromagnetic field can be always described with the eigenmodes

of the current deformation.
The connection coefficient can be now rewritten as

$$\mathcal{C}_{nm} = V_{\text{cav}}^{-1/3} \sqrt{\frac{U_n}{U_m}} \sum_l q_l(t) C_{nm}^l \tag{3.59}$$

where C_{nm}^l is the normalized, dimensionless version of the connection coefficient given by

$$C_{nm}^l = \frac{V_{\text{cav}}^{1/3}}{2\sqrt{U_n U_m}} \int_{\partial V_{\text{cav}}} \mathrm{d}\vec{S} \cdot \vec{\xi}_l(\vec{x}) \Big[\frac{1}{\mu_0} \vec{B}_n(\vec{x}) \vec{B}_m(\vec{x}) - \epsilon_0 \vec{E}_n(\vec{x}) \vec{E}_m(\vec{x}) \Big]. \tag{3.60}$$

4. Gravitational Waves

In this chapter, we review the facts from linearized gravity that are relevant to build up the theory of heterodyne cavity experiments. We start with a short overview of gravitational wave (GW) physics, focusing on the problem of choosing the appropriate gauge. In this regard, we give a detailed description of the proper detector frame, which turns out to be the best gauge choice for calculating the response of a detector to a GW. Finally, we derive a formula for the tidal force describing how a GW transfers energy into a cavity.
Most of the material covered in this chapter can be also found more detailed in standard text books, such as [55, 56, 57].

4.1. Linearized Theory of Gravity

The general equations governing the interaction of matter with the underlying spacetime metric $g_{\mu\nu}$ are given by the Einstein Equations

$$R_{\mu\nu} - \frac{1}{2} g_{\mu\nu} R = \frac{8\pi G}{c^4} T_{\mu\nu}. \tag{4.1}$$

The Ricci Tensor $R_{\mu\nu}$ and Ricci Scalar R describe the metric and therefore the space curvature, whereas $T_{\mu\nu}$ is the stress-energy tensor induced by an arbitrary energy density. Since the Einstein Equation is non-linear, it is in general very difficult to calculate exact solutions. However, there are several simplified cases allowing for an analytical treatment. An example is a system with low energy density, so one can assume that the metric is approximately flat except for a small perturbation, i.e.

$$g_{\mu\nu} = \eta_{\mu\nu} + h_{\mu\nu} \qquad\qquad g^{\mu\nu} = \eta^{\mu\nu} - h^{\mu\nu} \tag{4.2}$$

The symmetric tensor $h_{\mu\nu}$ is called *strain* and describes small perturbations in the sense that $|h_{\mu\nu}| \ll 1$ as well as $|\partial_\alpha h_{\mu\nu}| \ll 1$. For instance, the strain caused by the Earth's gravitational field can be estimated as [57]

$$|h_{\mu\nu}| \sim |\Phi| \lesssim \frac{M_\odot}{R_\odot} \cong 10^{-6}.$$

where Φ is the gravitational potential.
These conditions require a specific choice of the coordinate frame, because the energy density is not the same for every observer. So the invariance of general relativity under coordinate transformation is broken. However, there is a remaining gauge freedom of the form

$$x'^\mu = x^\mu + \xi^\mu(x) \tag{4.3}$$

where $\xi^\mu(x)$ is a small four-vector in the same sense as $h_{\mu\nu}$ (so we can neglect all terms of order $\mathcal{O}(\xi^2)$ in the following). Using

$$g_{\mu\nu} + h'_{\mu\nu} = (g_{\alpha\beta} + h_{\alpha\beta}) \frac{\partial x^\alpha}{\partial x'^\mu} \frac{\partial x^\beta}{\partial x'^\nu},$$

it is straightforward to show that the strain $h_{\mu\nu}$ transforms as

$$h'_{\mu\nu} = h_{\mu\nu} - \partial_\nu \xi_\mu - \partial_\mu \xi_\nu := h_{\mu\nu} - \mathcal{L}_\xi \eta_{\mu\nu}. \tag{4.4}$$

where $\mathcal{L}_\xi \eta_{\mu\nu} := \partial_\nu \xi_\mu + \partial_\mu \xi_\nu$ is the Lie derivative with respect to ξ [58]. We can apply this derivative to an arbitrary tensor $T^{\mu\nu\cdots}{}_{\alpha\beta\ldots} = (T^{(1)})^{\mu\nu\cdots}{}_{\alpha\beta\ldots} + (T^{(0)})^{\mu\nu\cdots}{}_{\alpha\beta\ldots}$, where 0 denotes the unperturbed and 1 the perturbed part. It follows [58]

$$(T'^{(1)})^{\mu\nu\cdots}{}_{\alpha\beta\ldots} = (T^{(1)})^{\mu\nu\cdots}{}_{\alpha\beta\ldots} - \mathcal{L}_\xi (T^{(0)})^{\mu\nu\cdots}{}_{\alpha\beta\ldots},$$

which can be read as a general form of eqn. 4.4. We can directly see that a general tensor is invariant under a gauge transformation (eqn. 4.3) if and only if it vanishes in flat space. One example is given by the Riemann curvature tensor, i.e.

$$R'^{\mu}{}_{\alpha\beta\nu} = R^{\mu}{}_{\alpha\beta\nu}. \tag{4.5}$$

We now want to give a short review of the linearization procedure. The starting point is to calculate the christoffel symbols, which are given by

$$\Gamma^{\mu}_{\alpha\beta} = \frac{1}{2}(\partial_\alpha h_\beta{}^\mu + \partial_\beta h_\alpha{}^\mu - \partial^\mu h_{\alpha\beta}) \tag{4.6}$$

in leading order. They can be used to determine the Riemann tensor, which becomes

$$R_{\mu\alpha\beta\nu} = \frac{1}{2}(\partial_\alpha \partial_\beta h_{\mu\nu} + \partial_\mu \partial_\nu h_{\alpha\beta} - \partial_\mu \partial_\beta h_{\alpha\nu} - \partial_\alpha \partial_\nu h_{\mu\beta}). \tag{4.7}$$

We can plug this into eqn. 4.1, using that $R_{\mu\nu} = R^{\alpha}{}_{\mu\alpha\nu}$. Additionally, we assume the local environment to be approximately a vacuum, i.e. $T_{\mu\nu} = 0$. Altogether, the linearized Einstein equation yields

$$\partial_\nu \partial^\alpha h_{\mu\alpha} + \partial_\mu \partial^\alpha h_{\nu\alpha} - \partial^\alpha \partial_\alpha h_{\mu\nu} - \partial_\mu \partial_\nu h^\alpha{}_\alpha - g_{\mu\nu}(\partial^\alpha \partial^\beta h_{\alpha\beta} - \partial^\beta \partial_\beta h^\alpha{}_\alpha) = 0. \tag{4.8}$$

The form of this equation, however, is not very practical. We therefore introduce the *trace-reversed* strain defined by

$$\bar{h}_{\mu\nu} = h_{\mu\nu} - \frac{1}{2} g_{\mu\nu} h^\alpha{}_\alpha \qquad \Leftrightarrow \qquad h_{\mu\nu} = \bar{h}_{\mu\nu} - \frac{1}{2} g_{\mu\nu} \bar{h}^\alpha{}_\alpha.$$

Substituting it into eqn. 4.8 leads to

$$\partial_\alpha \partial^\alpha \bar{h}_{\mu\nu} + g_{\mu\nu} \partial^\alpha \partial^\beta \bar{h}_{\alpha\beta} - \partial^\alpha \partial_\nu \bar{h}_{\mu\alpha} - \partial^\alpha \partial_\mu \bar{h}_{\nu\alpha} = 0. \tag{4.9}$$

Now, we can use the gauge transformation given in eqn. 4.3 in order to reduce the initially ten degrees of freedom encoded in the strain. Note that this has to be done carefully, since fixing the gauge is equivalent to the choice of a particular coordinate system. We will address this problem in detail later, but for we now look at the standard gauge, which can be found in many standard textbooks such as [11, 56, 57, 59].
First, equation 4.9 can be brought into the form of a wave equation by applying the *Lorentz Gauge*

$$\partial^\mu \bar{h}_{\mu\nu} = 0. \tag{4.10}$$

This reduces the number of degrees of freedom to six and the linearized Einstein equation yields

$$\partial^\alpha \partial_\alpha \bar{h}_{\mu\nu} = 0. \tag{4.11}$$

However, there is still a residual gauge degree of freedom. It is given by a transformation $x'^\mu = x^\mu + \xi^\mu(x)$ where ξ^μ fulfills the property

$$\partial^\alpha \partial_\alpha \xi^\mu(x) = 0. \tag{4.12}$$

This fixes another four gauge degrees of freedom and we are therefore free to choose the strain such that

$$h^{0\mu} = 0 \qquad\qquad h^i{}_i = 0 \qquad\qquad \partial^j h_{ij}. \tag{4.13}$$

Since this metric is transverse and traceless, it is commonly referred to as TT-gauge. Note that the total number of degrees of freedom is two, corresponding to two different polarizations of the GW. Furthermore, it is $\bar{h}_{\mu\nu} = h_{\mu\nu}$.
We will describe the physical meaning of this gauge in a moment, but we first introduce an important mathematical tool called the equation of geodesic deviation.

4.2. The Equation of Geodesic Deviation

The equation of geodesic deviation describes how the distance between two freely falling observers on two different geodesics evolves dependent on a parameter λ, which can be usually identified with the proper time τ or the proper distance s. The derivation shown here follows [11]. We start with the standard geodesic equation for one of the two observers given by

$$\frac{\partial^2 x^\mu}{\partial \lambda^2} + \Gamma^\mu_{\alpha\beta}(x(\lambda)) \frac{\partial x^\alpha}{\partial \lambda} \frac{\partial x^\beta}{\partial \lambda} = 0. \tag{4.14}$$

Now, assume that the geodesics of the second observer varies only slightly from the first one and can be parametrized with $x'^\mu(\lambda) = x^\mu(\lambda) + \xi^\mu(\lambda)$, where the small vector $\xi(\lambda)$ connects two points on the geodesics with same λ. It is $\xi^\mu(0) = 0$, so that the obeservers cross at one point. The idea now is to plug the parameterization into the geodesic equation and expand up to linear order in ξ. Therefore, note that the christoffel symbol has to be expanded as

$$\Gamma^\mu_{\alpha\beta}(x + \xi) = \Gamma^\mu_{\alpha\beta}(x) + \xi^\nu (\partial_\nu \Gamma^\mu_{\alpha\beta})(x) + \mathcal{O}(\xi^2),$$

neglecting all higher order terms in ξ. It is then straightforward to calculate

$$\begin{aligned} 0 &= \frac{\partial^2 (x^\mu + \xi^\mu)}{\partial \lambda^2} + \Gamma^\mu_{\alpha\beta}(x + \xi) \frac{\partial (x^\alpha + \xi^\alpha)}{\partial \lambda} \frac{\partial (x^\beta + \xi^\beta)}{\partial \lambda} \\ &= \frac{\partial^2 x^\mu}{\partial \lambda^2} + \Gamma^\mu_{\alpha\beta}(x) \frac{\partial x^\alpha}{\partial \lambda} \frac{\partial x^\beta}{\partial \lambda} + \frac{\partial^2 \xi^\mu}{\partial \lambda^2} + 2\Gamma^\mu_{\alpha\beta}(x) \frac{\partial x^\alpha}{\partial \lambda} \frac{\partial \xi^\beta}{\partial \lambda} \\ &\qquad + \xi^\nu (\partial_\nu \Gamma^\mu_{\alpha\beta})(x) \frac{\partial x^\alpha}{\partial \lambda} \frac{\partial x^\beta}{\partial \lambda} + \mathcal{O}(\xi^2). \end{aligned}$$

Applying eqn. 4.14 again, we arrive at the equation of geodesic deviation

$$\frac{\partial^2 \xi^\mu}{\partial \lambda^2} + 2\Gamma^\mu_{\alpha\beta}(x) \frac{\partial x^\alpha}{\partial \lambda} \frac{\partial \xi^\beta}{\partial \lambda} + \xi^\nu (\partial_\nu \Gamma^\mu_{\alpha\beta})(x) \frac{\partial x^\alpha}{\partial \lambda} \frac{\partial x^\beta}{\partial \lambda} = 0. \tag{4.15}$$

4.3. The TT-Gauge

We now discuss in detail the most important gauge for the theory of GWs. Although the strain takes a simple form, we will argue that it is not a physical gauge and that we have to use a different frame for the calculation of the detector response. However, we still need it, for example to calculate Riemann tensors. The reason is, as we argued in chapter 4.1, that Riemann tensor is invariant under gauge transformation.
Considering only the Lorentz gauged metric, the most general solution of eqn. 4.11 for the trace-reversed strain $\bar{h}_{\mu\nu}$ reads [59]

$$\bar{h}_{\mu\nu} = \int \mathrm{d}^3k \big(\bar{h}_{\mu\nu}(\vec{k})e^{i(\vec{k}\vec{x}-\omega t)} + \bar{h}^*_{\mu\nu}(\vec{k})e^{-i(\vec{k}\vec{x}-\omega t)}\big)$$

with $k^\mu \bar{h}_{\mu\nu} = 0$ and the dispersion relation $\omega(\vec{k}) = c|\vec{k}|$. Applying the residual gauge eqn. 4.12, this expression can be rewritten as

$$h^{TT}_{ij} = \sum_{r=+,\times} \int \frac{\mathrm{d}^3k}{(2\pi)^3} h_r(\vec{k},t) e^r_{ij}(\hat{k}) e^{-i\vec{k}\vec{x}}, \tag{4.16}$$

where we sum over the two remaining degrees of freedom, also called polarizations, of the GW. Note that $\hat{k} := \vec{k}/|\vec{k}|$. The polarization tensors $e^r_{ij}(\hat{k})$ are symmetric, transverse ($\hat{k}_i e^r_{ij} = 0$) and traceless. They are defined by [59]

$$\begin{aligned} e^+_{ij}(\hat{k}) &= \hat{m}_i\hat{m}_j - \hat{n}_i\hat{n}_j \\ e^\times_{ij}(\hat{k}) &= \hat{m}_i\hat{n}_j + \hat{n}_i\hat{m}_j, \end{aligned}$$

where $\hat{m}$ and $\hat{n}$ are unit vectors orthogonal to $\hat{k}$ and to each other. The fourier modes $h_r(\vec{k},t)$ are real when the condition $h^*_r(\vec{k},t) = h_r(-\vec{k},t)$ is fulfilled.
We consider the simple case of a monochromatic GW propagating along the z-direction. Here, the fourier modes take the form

$$h_r(\vec{k},t) = (2\pi)^3 h_r\big(\delta^3(\vec{k} - k_z\hat{z})e^{i\omega t} + \delta(\vec{k} + k_z\hat{z})e^{-i\omega t}\big)$$

and we can identify $\hat{m} := \hat{x}$ as well as $\hat{n} := \hat{y}$. The full gravitational wave can be then written as

$$h^{TT}_{ij}(\vec{k},t) = \begin{pmatrix} h_+ & h_\times & 0 \\ h_\times & -h_+ & 0 \\ 0 & 0 & 0 \end{pmatrix} \cos(\omega t - k_z z). \tag{4.17}$$

This metric additionally provides the corresponding line element $\mathrm{d}s$ given by

$$\begin{aligned} \mathrm{d}s^2 = -c^2\mathrm{d}t^2 + \mathrm{d}z^2 &+ \big(1 + h_+\cos(\omega t - k_z z)\big)\mathrm{d}x^2 \\ &+ \big(1 - h_+\cos(\omega t - k_z z)\big)\mathrm{d}y^2 + 2h_\times\cos(\omega t - k_z z)\mathrm{d}x\mathrm{d}y \end{aligned} \tag{4.18}$$

We now discuss the physical meaning of the TT-frame, following again [11]. This can be done by considering the geodesic equation for a particle which is initially at rest at $\tau = 0$, such that $\mathrm{d}x^i/\mathrm{d}\tau = 0|_{\tau=0}$. Equation 4.14 than takes the form

$$\left.\frac{\partial^2 x^i}{\partial\tau^2}\right|_{\tau=0} = -\frac{1}{2}(2\partial_0 h_{0i} - \partial_i h_{00})\left(\frac{\partial x^0}{\partial\tau}\right)^2\Bigg|_{\tau=0} = 0,$$

where the last step follows by applying the properties of the TT-gauge given in eqn. 4.13. So we see that, if $\mathrm{d}x^i/\mathrm{d}\tau = 0$ at $\tau = 0$, it remains zero at all times. It is instructive to think about the TT-frame as a coordinate system which deforms itself in response to a GW such that masses initially at rest do not move. One way to construct this frame is by defining the test masses themselves as points of the coordinate system [11].
We can further analyse the distance between two coordinate points in the TT-frame by using the equation of geodesic deviation. Therefore, we introduce a second freely falling test mass at a small distance $\xi^\mu(\tau)$ to the first one, such that $\mathrm{d}\xi^i/\mathrm{d}\tau|_{\tau=0} = 0$. Plugging this into eqn. 4.15 yields

$$\left.\frac{\partial^2 \xi^i}{\partial \tau^2}\right|_{\tau=0} = -\left[\partial_0 h_{ij} \frac{\partial \xi^i}{\partial \tau}\right]\Bigg|_{\tau=0} = 0.$$

So again, if $\mathrm{d}\xi^i/\mathrm{d}\tau = 0$ at $\tau = 0$, the distance remains constant at all times.
It is important to note that ξ^i is a coordinate distance in this context and therefore generally not equal to the proper distance s, which can be calculated with eqn. 4.18. We can see immediately, that s does not vanish for a non-zero perturbation $h_{\mu\nu}$ and is therefore a better choice for calculating physical effects.
However, in order to describe the detector response to a GW, it is convenient to have a coordinate frame which is directly connected to the physical effects of $h_{\mu\nu}$. So in the next chapter, we will give a detailed discussion of how to find a better coordinate system.

4.4. The Proper Detector Frame

In a laboratory, a coordinate system is usually not defined by freely falling particles [11]. Instead, it is more realistic to define the coordinate points with respect to a rigid ruler. In our case, this would be the cavity walls (except for a deformation induced by the GW tidal forces, which we consider later in this thesis).
A simple realisation is given by a freely falling frame, which can be described by Fermi normal coordinates. It can be understood as the best approximation to flat Euclidean coordinates in the vicinity of the observer. One way to derive Fermi normal coordinates is to use elementary differential geometry and the equation of geodesic deviation. Since the last one is only valid for small distances, the resulting metric should only be accurate close to the observer's geodesic. More details can be found in [57, 60].
However, because of the planet's rotation and gravitational field, a detector on earth can be in general not described by a freely falling frame. So more effort has to be done in order to include these effects as well. Using again the equation of geodesic deviation, the result reads after a lengthy calculation [11, 57, 61]

$$\begin{aligned}\mathrm{d}s^2 = &\big(-(1+\vec{a}\vec{x})^2 + (\vec{\omega}\times\vec{x})^2 - R_{0i0j}(G)x^i x^j\big)\mathrm{d}t^2 \\ &+ 2\big(\omega^j x^k \epsilon_{ijk} - \frac{2}{3}R_{0ikj}(G)x^j x^k\big)\mathrm{d}t\mathrm{d}x^i + \big(\delta_{ij} - \frac{1}{3}R_{ikjl}(G)x^k x^l\big)\mathrm{d}x^i\mathrm{d}x^j,\end{aligned} \tag{4.19}$$

where $\vec{a}$ and $\vec{\omega}$ are the local acceleration and rotation vectors.
In principle, we could now go on using this metric. Although it is an approximation for small distances to the observer's worldline, we often deal with GWs in the kHz to MHz regime, which have a wavelength much longer than the detector size. But, since it may be possible to modify the experiment to be sensitive for higher frequencies where the approximation is not further

valid, we want to give a detailed discussion of the full solution. In future work, we may then extend the theory by using the general metric. Note that this has already been done to some extend in [4, 31], so there are already existent approaches.
We start with a brief historical outline. After Ni and Zimmermann found equation 4.19 in 1978 [61], efforts were made to find higher order terms or even the full metric in the proper detector frame. They all used modifications of the equation of geodesic deviation and were only able to find the third and fourth order terms of the expansion [62, 63]. At least in [63], an iteration scheme was given for calculating in principle all orders of magnitude, but it is very time-consuming to use.
The first successful derivation for all orders was made by Fortini and Gualdi in 1982 for the special case of a plane GW in a flat background [64]. In 1994, the result was generalized by Marzlin for all possible metric perturbations [65]. Since the derivation invented by Marzlin is very compact and straightforeward, we want at least review the main ideas in the following. A throughout discussion for the case of a plain gravitational wave can be found in [66].
We start by considering an observer moving along its own so-called *reference geodesics* $g^\mu(\tau)$. It fulfills, as usual, the geodesic equation

$$\frac{\mathrm{d}^2 g^\mu}{\mathrm{d}\tau^2} + \Gamma^\mu_{\alpha\beta}(g(\tau))\frac{\mathrm{d}g^\alpha}{\mathrm{d}\tau}\frac{\mathrm{d}g^\beta}{\mathrm{d}\tau} = 0,$$

where τ is the eigentime of the observer. Now, we take a family of geodesics $y^\mu(\tau, s)$, starting from $g^\mu(\tau)$ such that $y^\mu(\tau, 0) = g^\mu(\tau)$. They are called *connecting geodesics* and fulfill the corresponding geodesic equation

$$\frac{\mathrm{d}^2 y^\mu}{\mathrm{d}s^2} + \Gamma^\mu_{\alpha\beta}(y(s))\frac{\mathrm{d}y^\alpha}{\mathrm{d}s}\frac{\mathrm{d}y^\beta}{\mathrm{d}s} = 0, \tag{4.20}$$

where s denotes to the proper distance. Furthermore, we require that reference and connecting geodesics are perpendicular at the point of intersection, i.e.

$$\left.\frac{\mathrm{d}g^\mu}{\mathrm{d}\tau}\frac{\mathrm{d}y_\mu}{\mathrm{d}s}\right|_{s=0} = 0.$$

A sketch of the construction is given in fig. 4.1.
The strategy now is to decompose the geodesics in weak field approximation into a minkowskian part M and a perturbed part h, i.e.

$$\begin{aligned} g^\mu(\tau) &= g^\mu_M(\tau) + g^\mu_h(\tau) \\ y^\mu(\tau, s) &= y^\mu_M(\tau, s) + y^\mu_h(\tau, s). \end{aligned}$$

We can then solve eqn. 4.20 for $y_h(\tau, s)$ by integration. The result is [65]

$$\begin{aligned} y^\mu_h(\tau, s) = C^\mu_2(\tau) + sC^\mu_1(\tau) - \eta^{\mu\nu}v^\beta_M \int_0^s \mathrm{d}s' h_{\beta\nu}(y_M(\tau, s')) \\ + \frac{1}{2}\eta^{\mu\nu}v^\alpha_M v^\beta_M \int_0^s \mathrm{d}s' \int_0^{s'} \mathrm{d}s''(\partial_\nu h_{\alpha\beta})(y^\mu_M(\tau, s'')), \end{aligned} \tag{4.21}$$

where we have defined $v^\mu_M := \mathrm{d}y^\mu/\mathrm{d}s|_{s=0}$ and $C^\mu_1(\tau)$ as well as $C^\mu_2(\tau)$ are some integration constants that can be specified by defining a suitable coordinate system. In our case, we define a local tetrad $e^\mu_{\hat{\alpha}}(\tau)$ such that

$$\frac{\mathrm{d}x^\mu(\tau)}{\mathrm{d}\tau} = e^\mu_{\hat{0}}(\tau) \qquad\qquad v^\mu_M = \left.\frac{\mathrm{d}y^\mu}{\mathrm{d}s}\right|_{s=0} =: \alpha^{\hat{i}} e^\mu_{\hat{i}}(\tau).$$

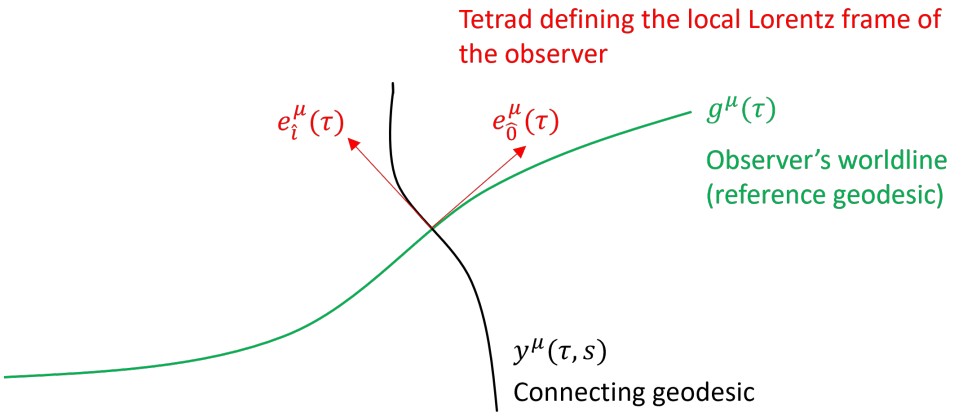

Figure 4.1.: *Construction of Fermi Normal Coordinates. The tangential vectors of the connecting geodesics define the spatial axis of the coordinate system. They are perpendicular to the worldline of the observer (reference geodesics). The tangential vector of the reference geodesics defines the time direction.*

Here, a hat denotes a coordinate index in the system of the tetrad. We further assume that the observer is not in general free, but can be accelerated or rotated, i.e.

$$\frac{\mathrm{d}e_{\hat{\alpha}}^{\mu}}{\mathrm{d}\tau} = -\Omega^{\mu}{}_{\nu} e_{\hat{\alpha}}^{\nu}.$$

The antisymmetric tensor $\Omega^{\mu\nu}$ encodes both the Fermi-Walker transport and a spatial rotation [57]. It is given by

$$\Omega^{\mu\nu} = a^{\mu}u^{\nu} - a^{\nu}u^{\mu} + u_{\alpha}\omega_{\beta}\epsilon^{\alpha\beta\mu\nu}.$$

Finally, we define Fermi Normal coordinates by choosing

$$x^{\hat{0}} := \tau \qquad\qquad x^{\hat{i}} := s\alpha^{\hat{i}}.$$

It is important to note that this choice of coordinate system is not unique. If $h_{\mu\nu}$ has a special shape, it may be instructive to consider other options. Two alternatives for the case of a monochromatic GW are discussed in [66].
With the precise definition of Fermi normal coordinates, we can further evaluate eqn. 4.21. The integrals can be calculated by expanding the strain as

$$h_{\hat{i}\hat{j}}(\tau, s) = \sum_{n=0}^{\infty} \frac{1}{n!} (\partial_{\hat{k}_1} \cdots \partial_{\hat{k}_n} h_{\hat{i}\hat{j}})(g) s^n \alpha^{\hat{k}_1} \cdots \alpha^{\hat{k}_n}.$$

The indices have to be understood as $x_{\hat{i}} := e_{\hat{i}}^{\mu} x_{\mu}$ and $h_{\hat{i}\hat{j}} := e_{\hat{i}}^{\alpha} e_{\hat{j}}^{\beta} h_{\alpha\beta}$. The general result for the connecting geodesics up to all orders then reads

$$\begin{aligned} y^{\mu}(x) = g^{\mu}(x^{\hat{0}}) &+ x^{\hat{i}}(e_{\hat{i}}^{\mu}(x^{\hat{0}}) + h_{\hat{i}}{}^{\mu}(x^{\hat{0}})) \\ &- \sum_{n=0}^{\infty} \frac{1}{(n+1)!} (\partial_{\hat{k}_1} \cdots \partial_{\hat{k}_n} h_{\hat{i}}{}^{\mu})(g) x^{\hat{i}} x^{\hat{k}_1} \cdots x^{\hat{k}_n} \\ &+ \frac{1}{2} \sum_{n=0}^{\infty} \frac{1}{(n+2)!} (\partial_{\hat{k}_1} \cdots \partial_{\hat{k}_n} \partial^{\mu} h_{\hat{i}\hat{j}})(g) x^{\hat{i}} x^{\hat{j}} x^{\hat{k}_1} \cdots x^{\hat{k}_n}. \end{aligned}$$

From here, it is in principle straightforeward to derive the general metric expansion in Fermi normal coordinates. However, we have to use the transformation

$$g_{\hat{\alpha}\hat{\beta}} = \frac{\partial y^\mu}{\partial x^{\hat{\alpha}}} \frac{\partial y^\nu}{\partial x^{\hat{\beta}}} g_{\mu\nu}(y(x)).$$

which leads to a rather lengthy calculation. Along the way, it is important to remember that the tetrad $e^\mu_{\hat{\alpha}}(\tau) = e^\mu_{\hat{\alpha}}(x^{\hat{0}})$ itself depends on the eigentime.
For the final result, we drop the hat above the index since everything is now written in Fermi normal coordinates. As given in [65], we arrive at

$$\begin{aligned} g_{00} &= -(1+\vec{a}\cdot\vec{x})^2 + (\vec{\omega}\times\vec{x})^2 - \gamma_{00} - 2(\vec{\omega}\times\vec{x})^i\gamma_{0i} - (\vec{\omega}\times\vec{x})^i(\vec{\omega}\times\vec{x})^j\gamma_{ij} \\ g_{0i} &= (\vec{\omega}\times\vec{x})_i - \gamma_{0i} - (\vec{\omega}\times\vec{x})^j\gamma_{ij} \\ g_{ij} &= \delta_{ij} - \gamma_{ij}. \end{aligned} \tag{4.22}$$

where $\vec{a}$ and $\vec{\omega}$ are again the acceleration and rotation vector respectively. The constants γ_{00}, γ_{0i} and γ_{ij} appear to be given the series expansions

$$\gamma_{00} = \sum_{n=0}^{\infty} \frac{2}{(n+3)!} x^k x^l x^{k_1} \cdots x^{k_n} (\partial_{k_1} \cdots \partial_{k_n} R_{0k0l})(g) \cdot \Big[(n+3) + 2(n+2)\vec{a}\vec{x} + (n+1)(\vec{a}\vec{x})^2\Big]$$

$$\gamma_{0i} = \sum_{n=0}^{\infty} \frac{2}{(n+3)!} x^k x^l x^{k_1} \cdots x^{k_n} (\partial_{k_1} \cdots \partial_{k_n} R_{0kil})(g) \cdot \Big[(n+2) + (n+1)\vec{a}\vec{x}\Big]$$

$$\gamma_{ij} = \sum_{n=0}^{\infty} \frac{2}{(n+3)!} x^k x^l x^{k_1} \cdots x^{k_n} (\partial_{k_1} \cdots \partial_{k_n} R_{ikjl})(g) \cdot \Big[n+1\Big].$$

Eqn. 4.22 gives the most general result for the local Lorentz frame in generalized gravity. Although it is very cumbersome to use, it is recommended as a starting point for all calculations. In most cases, it is possible to simplify the equations, but that strongly depends on the system. If the strain $h_{\mu\nu}$, for instance, varies on scales much larger than the detector, we are allowed to cut off the series expansion at some order. In case it is sufficient cut off at second order, one obtains eqn. 4.19, so the theory appears to be consistent with previous results.
In our experiment, we deal with GWs with frequencies in the range $\sim \mathcal{O}$(kHz-GHz). The gravitational field of the earth is almost static and varies on typical frequencies of $f \lesssim 0.1\,\mathrm{Hz}$ [59]. That means, we can well separate the GW signal from the background field and do not need to consider those effects. We therefore set $\vec{a} = 0$ and $\vec{\omega} = 0$ and end up with the metric [66]

$$h_{00} = -2\sum_{n=0}^{\infty} \frac{n+3}{(n+3)!} x^k x^l x^{k_1} \cdots x^{k_n} (\partial_{k_1} \cdots \partial_{k_n} R_{0k0l})(g) \tag{4.23}$$

$$h_{0i} = -2\sum_{n=0}^{\infty} \frac{n+2}{(n+3)!} x^k x^l x^{k_1} \cdots x^{k_n} (\partial_{k_1} \cdots \partial_{k_n} R_{0kil})(g) \tag{4.24}$$

$$h_{ij} = -2\sum_{n=0}^{\infty} \frac{n+1}{(n+3)!} x^k x^l x^{k_1} \cdots x^{k_n} (\partial_{k_1} \cdots \partial_{k_n} R_{ikjl})(g). \tag{4.25}$$

This metric has to be used when we deal with GW in the GHz-range as it was done e.g. in [31]. However, we concentrate on GW with frequencies equal or lower than 1 GHz throughout this

thesis, which have a larger wavelength than the detector size. Therefore, we assume that we can cut off the expansion at second order, although the approximation may not be accurate enough to describe the metric close to 1 GHz. We postpone a detailed analysis to future work, some discussions can be already found in [4, 31]. In the approximated form, the resulting metric then corresponds to the solutions given in [57, 60] and reads

$$\begin{aligned} \mathrm{d}s^2 = (-1 - R_{0i0j}(G)x^i x^j)\mathrm{d}t^2 - \frac{4}{3}x^i x^j R_{0ikj}(G)\mathrm{d}t\mathrm{d}x^k \\ + (\delta_{kl} - \frac{1}{3}x^i x^j R_{kilj}(G))\mathrm{d}x^k\mathrm{d}x^l \end{aligned}$$

in terms of the invariant line element. As we saw in chapter 4.1, the Riemann curvature tensor is invariant under a gauge transformation. Therefore, we can express the metric of the proper detector frame in terms of the TT-gauged strain, which simplifies the calculations a lot. It turns out that the only non-vanishing component using eqn. 4.13 is given by

$$R_{0i0j} = -\frac{1}{2}\ddot{h}_{ij}^{TT},$$

so the metric now reads

$$\mathrm{d}s^2 = -\mathrm{d}t^2\big(1 - \frac{1}{2}\ddot{h}_{ij}^{\mathrm{TT}}(g)x^i x^j\big) + \mathrm{d}x^i\mathrm{d}x^j\delta_{ij}.$$

Finally, the metric of the proper detector frame in the long wavelength regime has only one non-zero component, namely

$$h_{00} = \frac{1}{2c^2}\ddot{h}_{ij}^{\mathrm{TT}}(g)x^i x^j. \tag{4.26}$$

Note that we have turned to SI units in the last equation.

4.5. Gravitational Waves and Tidal Forces

There are two ways a GW can couple to a cavity that is loaded with an electromagnetic field. The first way is a direct coupling via the Gertsenshtein effect, while the second one is an indirect interaction through the cavity walls. We describe these couplings in detail in chapter 2.1. Since the GW is an oscillation of spacetime, it exerts a tidal force on the surface resulting in a small deformation. In this chapter, we want to show how this tidal force can be calculated, following [11, 57].

Consider a particle A in the proper detector frame. We define a coordinate system such that the particle sits at the origin, i.e., it is located at $x^0 = \tau$ and $x^j = 0$. A second particle B has a small separation ξ^μ to A, so the system can be described via the equation of geodesic deviation (eqn. 4.15). We get

$$\frac{\mathrm{d}^2\xi^\mu}{\mathrm{d}\tau^2} + 2\Gamma^\mu_{0\beta}(x)\frac{\mathrm{d}\xi^\beta}{\mathrm{d}\tau} + (\partial_\nu\Gamma^\mu_{00})(x)\xi^\nu = 0. \tag{4.27}$$

In the proper detector frame, by construction, we have at $x^j = 0$ that

$$\Gamma^\mu_{0\beta}(\tau, 0) = 0 \qquad \Rightarrow \qquad (\partial_\tau\Gamma^\mu_{0\beta})(\tau, 0) = 0. \tag{4.28}$$

Substituting this into equation 4.27 and evaluating at $x^j = 0$, we get

$$\frac{\mathrm{d}^2\xi^i}{\mathrm{d}\tau^2} + \xi^j(\partial_j\Gamma^i_{00}) = 0.$$

Note that we only consider the spatial components of the displacement. Using equation 4.28, we can write the Riemann tensor as

$$R^i{}_{0j0} = \partial_j \Gamma^i_{00}.$$

After renaming $\xi^i \to x^i$, the equation of geodesic deviation becomes

$$\frac{\mathrm{d}^2 x^i}{\mathrm{d}\tau^2} = -x^j R^i{}_{0j0}.$$

This equation describes the trajectory of a (nearby) particle B as seen from an observer sitting at particle A. Since force and acceleration are equivalent, we can directly translate it into a force density. Note that for one specific particle, we have

$$F^i = m\frac{\mathrm{d}^2 x^i}{\mathrm{d}\tau^2} = -mx^j R^i{}_{0j0}.$$

In the continuum limit, this can be written as a force density [38, 57]

$$f_i = -\rho(x) R_{0i0j}(x) x_j. \tag{4.29}$$

Note that this equation is valid in the proper detector frame and the Riemann tensor can be calculated in an arbitrary gauge.
Finally, we want to compute the force density 4.29 for the special case of a GW travelling in z-Direction. We therefore insert eqn. 4.17 into eqn. 4.29. For a GW with a wavelength much longer than the detector, we can drop the spatial dependence and replace $\cos(\omega_g t - k_z z)$ with $e^{i\omega_g t}$. The resulting generalized force density reads

$$f(t) = -\frac{1}{2}\omega_g^2 M V_{\mathrm{cav}}^{1/3}\big(h_+\Gamma_+ + h_\times\Gamma_\times\big)e^{i\omega_g t} =: F(t)e^{i\omega_g t}$$

where we have defined the normalized GW coupling strength parameters[1] as

$$\Gamma_+ := \frac{V_{\mathrm{cav}}^{-1/3}}{M}\int_{V_{\mathrm{cav}}} \mathrm{d}^3x\rho(\vec{x})\big(x\xi_{l,x}(\vec{x}) - y\xi_{l,y}(\vec{x})\big) \tag{4.30}$$

$$\Gamma_\times := \frac{V_{\mathrm{cav}}^{-1/3}}{M}\int_{V_{\mathrm{cav}}} \mathrm{d}^3x\rho(\vec{x})\big(x\xi_{l,y}(\vec{x}) + y\xi_{l,x}(\vec{x})\big) \tag{4.31}$$

and M is again the cavity mass. We will later need the fourier transform $F(\omega)$, which is given by

$$F(\omega) = -\frac{1}{2}\omega_g^2 M V_{\mathrm{cav}}^{1/3}\big(h_+\Gamma_+ + h_\times\Gamma_\times\big)2\pi\delta(\omega). \tag{4.32}$$

[1] We have adopted the notation from [5]

5. The Equations of Motion

As mentioned earlier, the GW can couple to an electromagnetic resonator in two different ways. First, there is a indirect coupling via a mechanical deformation of the cavity walls. This can be treated with a combination of elasticity theory and cavity perturbation theory. A detailed treatment can be found in chapter 3.4 and 3.5. Another possible interaction is the direct coupling of the GW to the electromagnetic field, also known as the inverse Gertsenshtein effect [27, 28]. When we derive the fundamental equations of motions governing the interaction of a GW with a SCRF cavity, we must consider both effects. We start with a detailed treatment of the Gertsenshtein effect and use it as a starting point to derive the Lagrangian of the full system. This Lagrangian can be then splitted into two separate parts which finally lead to the equations of motion in the usual manner.

5.1. The Gertsenshtein Effect

In 1962, Mikhail E. Gertsenshtein discovered that an electromagnetic wave travelling through a static transverse magnetic field can induce a GW with the same frequency [27]. The coupling was further investigated by Yakov B. Zel'dovic in 1973 [28]. Sometimes, this effect is therefore called Gertsenshtein-Zel'dovic effect, but we will just refer to it as the Gertsenshtein effect as it is common in the literature.
In particular, we are interested in the opposite interaction, namely of a GW propagating through an electromagnetic field. By the fundamental principle of time reversal symmetry, this should induce a photon with the same frequency as the GW. We call this the inverse Gertsenshtein effect. The starting point is the Einstein-Maxwell action of the form [31]

$$S_{\mathrm{EM}} = \int \mathrm{d}^4x\sqrt{-g}\Big(-\frac{1}{4}g^{\mu\alpha}g^{\nu\beta}F_{\mu\nu}F_{\alpha\beta} - g^{\mu\nu}j_\mu A_\nu\Big).$$

To apply linearized gravity (see chapter 4.1, in particular eqn. 4.2), we note that the determinant can be written as

$$g = \det(\eta_{\mu\nu} + h_{\mu\nu}) = -1 + h_{00} - h_{11} - h_{22} - h_{33} = -1 - h$$

where $h := h_\alpha{}^\alpha$ is defined as the trace of the strain. It directly follows that $\sqrt{-g} = 1 + h/2 + \mathcal{O}(h^2)$, so we can write the action as

$$\begin{aligned} S_{\mathrm{EM}} &= \int \mathrm{d}^4x\Big(1+\frac{h}{2}\Big)\Big(-\frac{1}{4}(\eta^{\mu\alpha} - h^{\mu\alpha})(\eta^{\nu\beta} - h^{\nu\beta})F_{\mu\nu}F_{\alpha\beta} - (\eta^{\mu\nu} - h^{\mu\nu})j_\mu A_\nu\Big) \\ &= S_{\mathrm{FLAT}} + S_{\mathrm{SOURCE}} + S_{\mathrm{COUPLING}} \end{aligned}$$

After rearranging all terms in the interaction and integrating by parts, we can identify the various segments of the action as

$$\begin{aligned} S_{\text{FLAT}} &= \int \mathrm{d}^4x \Big(-\frac{1}{4}\eta^{\mu\alpha}\eta^{\nu\beta}F_{\mu\nu}F_{\alpha\beta}\Big) \\ S_{\text{SOURCE}} &= \int \mathrm{d}^4x \Big(-j^\mu A_\mu\Big) \\ S_{\text{COUPLING}} &= \int \mathrm{d}^4x \Big(-\frac{1}{2}j^\mu_{\text{eff}}A_\mu - \frac{h}{2}j^\mu A_\mu + h^{\mu\nu}j_\mu A_\nu\Big), \end{aligned}$$

where the effective current j^μ_{eff} is given by

$$j^\mu_{\text{eff}} = \partial_\nu\big(\frac{h}{2}F^{\mu\nu} + h^\nu{}_\alpha F^{\alpha\mu} - h^\mu{}_\alpha F^{\alpha\nu}\big). \tag{5.1}$$

Note that a GW does not only couple to the electromagnetic field, but also to the residual current j^μ. We can therefore not just add j^μ_{eff} to the maxwell equations.
The current, however, is supposed to vanish, as we consider an evacuated cavity without any residual moving charges. We can read off the remaining Lagrangian from the action and find

$$\mathcal{L}_{\text{EM}} = -\frac{1}{4}\eta^{\mu\alpha}\eta^{\nu\beta}F_{\mu\nu}F_{\alpha\beta} - \frac{1}{2}j^\mu_{\text{eff}}A_\mu \tag{5.2}$$

From here, we can in principle start to add cavity perturbation theory in order to obtain the full Lagrangian. But before we do this, we want to have a closer look on the j^μ_{eff}. The equations of motion following from S_{EM} are not directly obvious, because the effective current is a function of the gauge field, i.e. $j^\mu_{\text{eff}} = j^\mu_{\text{eff}}(A_\mu)$. While the terms $S_{\text{FLAT}} + S_{\text{SOURCE}}$ lead to the familiar Maxwell equations

$$\partial_\mu F^{\mu\nu} = j^\nu,$$

we have to be careful evaluating S_{COUPLING}. We therefore start by considering the variation, which reads

$$\begin{aligned} \delta S_{\text{COUPLING}} = -\int \mathrm{d}^4x \Big(-\frac{1}{2}\partial_\rho \frac{\partial(j^\mu_{\text{eff}}A_\mu)}{\partial(\partial_\rho A_\nu)} + \frac{1}{2}\partial_\rho\partial_\sigma \frac{\partial(j^\mu_{\text{eff}}A_\mu)}{\partial(\partial_\rho\partial_\sigma A_\nu)} \\ + \frac{1}{2}j^\nu_{\text{eff}} + \frac{h}{2}j^\nu - h^{\mu\nu}j_\mu\Big)\delta A_\nu. \end{aligned}$$

after partial integration. Using basic index manipulations, it is now straightforward to show the identity

$$\partial_\rho\partial_\sigma \frac{\partial(j^\mu_{\text{eff}}A_\mu)}{\partial(\partial_\rho\partial_\sigma A_\nu)} = \partial_\rho \frac{\partial(j^\mu_{\text{eff}}A_\mu)}{\partial(\partial_\rho A_\nu)} + j^\nu_{\text{eff}}.$$

Hence, we can cancel the derivative terms and get

$$\delta S_{\text{COUPLING}} = -\int \mathrm{d}^4x \Big(j^\nu_{\text{eff}} - \frac{h}{2}j^\nu + h^{\mu\nu}j_\mu\Big)\delta A_\nu.$$

So we finally end up with the modified Maxwell equations

$$\partial_\mu F^{\mu\nu} = j^\nu + j^\nu_{\text{eff}} + \frac{h}{2}j^\nu - h^{\mu\nu}j_\mu.$$

Without residual currents, they reduce to $\partial_\mu F^{\mu\nu} = j^\nu_{\text{eff}}$. We can see that, although the current depends on the gauge field, we obtain the same form of the Maxwell equations in vacuum as for a normal current.
However, there is one important difference between the effective current in eqn. 5.1 and a normal current. When we consider the behaviour under coordinate transformation, we find

$$j'^\mu_{\text{eff}} = \frac{\mathrm{d}x'^\mu}{\mathrm{d}x^\alpha} j^\alpha_{\text{eff}} + \frac{\mathrm{d}x'^\mu}{\mathrm{d}x^\alpha}\frac{\mathrm{d}x^\gamma}{\mathrm{d}x'^\nu}\frac{\mathrm{d}^2x'^\nu}{\mathrm{d}x^\beta \mathrm{d}x^\gamma}\frac{h}{2}F^{\alpha\beta},$$

so, unlike j^μ, the effective current does not transform as a proper tensor. This implies that we cannot use the invariance condition (see chapter 4.1), which has guaranteed that a tensor is invariant under gauge transformations in linearized theory if it vanishes in flat space. So j^μ_{eff} is not gauge independent and we have to evaluate it in the proper detector frame to get physically reasonable results.

5.2. The Full Lagrangian

We now consider the full Lagrangian of the heterodyne cavity (HC) system. It consists of both the electromagnetic Lagrangian $\mathcal{L}_{\text{EM}}$ in eqn. 5.2 and the mechanical Lagrangian in eqn. 3.57. Due to the appearance of the gauge field in the current term, we cannot simply integrate out the spatial degrees of freedom in $\mathcal{L}_{\text{EM}}$. We therefore start with

$$L_{\text{HC}} = \int_{V_{\text{cav}}} \mathrm{d}V \Big[-\frac{1}{4}F'_{\mu\nu}F'^{\mu\nu} - \frac{1}{2}j^\mu_{\text{eff}}A'_\mu \Big] + \sum_l \big(\frac{1}{2}M\dot{q}_l^2(t) - \frac{1}{2}M\omega_l q_l^2(t) + q_l(t)f_l(t)\big), \tag{5.3}$$

where a prime denotes that the fields are perturbed by the deformation $q_l(t)$. The wall displacement is not just governed by the GW, but also, as we show later, by the electromagnetic field in the cavity. Thus, it is much larger than the GW strain and we can assume $h(t) \ll q_l(t) \ll e_n(t), b_n(t)$. The perturbation of the gauge field leads to an additional term of order $\mathcal{O}(hq_l)$, which can be neglected. Therefore, the gauge field can be considered as unperturbed. We split the Lagrangian into

$$\mathcal{L}_{\text{EM}} = -\frac{1}{4}F_{\mu\nu}F^{\mu\nu} - \frac{1}{2}j^\mu_{\text{eff}}A_\mu \tag{5.4}$$

$$L_{\text{mech}} = \frac{1}{2}\sum_n 2U_n(e'^2_n(t) - b'^2_n(t)) + \sum_l \Big(\frac{1}{2}M\dot{q}_l^2(t) - \frac{1}{2}M\omega_l^2 q_l^2(t) + q_l(t)f_l(t)\Big), \tag{5.5}$$

where $\mathcal{L}_{\text{EM}}$ governs the dynamics of the electromagnetic fields and L_{mech} the displacement. Note that we have integrated out the spatial degrees of freedom in eqn. 5.5, using the invariant

$$\frac{1}{4}F'_{\mu\nu}F'^{\mu\nu} = \frac{1}{2}\Big(\frac{1}{\mu_0}\vec{B}'^2(t,\vec{x}) - \varepsilon_0\vec{E}'^2(t,\vec{x})\Big)$$

of the field strength tensor as well as eqn. 3.7 and eqn. 3.17. Furthermore, note that we have removed the primes in eqn. 5.4. The reason is that we will apply cavity perturbation theory on the level of the equations of motions, which will turn out to be more convenient. For reasons of consistency, both should lead to the same physics. As we will in chapter 5.2.2, this is indeed the case.

5.2.1. Equation of Motion for the Electromagnetic Field

We start with the equations of motion (EoM) governing the dynamics of the electromagnetic field. We have already derived them in chapter 5.1 and found the modified Maxwell equations $\partial_\mu F^{\mu\nu} = j^\nu_{\text{eff}}$. As usual, they can be written as

$$\begin{aligned} \nabla \vec{E} &= \rho_{\text{eff}} \\ \nabla \times \vec{B} - \frac{1}{c^2}\partial_t \vec{E} &= \vec{j}_{\text{eff}} \end{aligned}$$

where $\rho_{\text{eff}} := j^0_{\text{eff}}$ is the effective charge density. We can now take the curl of Ampéres law in order to derive the wave equation. Consider the interim result

$$-\Delta\vec{B} + \nabla(\nabla\vec{B}) - \frac{1}{c^2}\partial_t \nabla \times \vec{E} = \nabla \times \vec{j}_{\text{eff}}.$$

When we apply the mode decomposition 3.7, it is not directly obvious that $\nabla\vec{B}_n = 0$. For irrotational modes, this is in general not true. But, we argued in chapter 3.1 and appendix B, that it is not possible to resonantly enhance the irrotational modes. They are therefore irrelevant for our analysis. So, we proceed as usual with $\nabla\vec{B}_n = 0$ and write

$$\sum_m \Big(b_m(t)\Delta\vec{B}_m(\vec{x}) - \frac{1}{c^2}\ddot{b}_m(t)\vec{B}_m(\vec{x})\Big) = -\nabla \times \vec{j}_{\text{eff}}.$$

Using $\Delta\vec{B}_n = -\omega_n^2/c^2\vec{B}_n$ together with eqn. 3.17 and integrating both sides over $\int_{V_{\text{cav}}} \mathrm{d}^3x\vec{B}_n(\vec{x})$ leads to

$$\ddot{b}_n(t) + \omega_n^2 b_n(t) = J_n(t). \tag{5.6}$$

The projected current on the right hand side is defined by

$$J_n(t) := \frac{c^2}{2U_n}\int_{V_{\text{cav}}} \mathrm{d}^3x \frac{1}{\mu_0}\vec{B}_n(\vec{x})\nabla \times \vec{j}_{\text{eff}}(t,\vec{x}). \tag{5.7}$$

At this stage, we can impose cavity perturbation theory. When $b_n(t)$ is replaced by $b'_n(t)$ (see eqn. 3.48), we can write eqn. 5.6 as

$$\begin{aligned} &\ddot{b'}_n + \omega_n'^2 b'_n \\ &\quad = \ddot{b}_n - \frac{1}{2}\mathcal{C}_{nn}\ddot{b}_n + \sum_{m\neq n}\beta_{nm}\frac{U_m}{U_n}\ddot{b}_m + \omega_n^2\big(1-\frac{1}{2}\mathcal{C}_{nn}\big)^2\big(b_n - \frac{1}{2}\mathcal{C}_{nn}b_n + \sum_{m\neq n}\beta_{nm}\frac{U_m}{U_n}b_m\big). \end{aligned}$$

In leading order, eqn. 5.6 can be used to rewrite the time derivatives as $\mathcal{C}_{nm}\ddot{b}_m = -\mathcal{C}_{nm}\omega_m^2 b_m + \mathcal{O}(q_l^2)$. Further calculations and the use of eqn. 3.44 and eqn. 3.59 give

$$\ddot{b}_n + \omega_n^2 b_n = \omega_n^2 V_{\text{cav}}^{-1/3}\sum_l q_l\Big(C^l_{nn}b_n + \sum_{m\neq n}\sqrt{\frac{U_m}{U_n}}C^l_{nm}b_m\Big) + J_n(t).$$

In a heterodyne setup, only the pump mode ($n = 0$) and the signal mode ($n = 1$) contribute to the dynamics. Furthermore, we assume that only one mechanical mode is relevant and couples to the GW. In the following, this mode is denoted again as q_l, meaning that l is now some fixed

integer. The result is a set of two coupled EoMs describing the dynamics of the pump mode as well as of the signal mode, i.e.

$$\ddot{b}_0(t) + \omega_0^2 b_0(t) = \omega_0^2 V_{\text{cav}}^{-1/3} q_l(t)\Big(C_{00}^l b_0(t) + \sqrt{\frac{U_1}{U_0}} C_{01}^l b_1(t)\Big) + J_0(t) \tag{5.8}$$

$$\ddot{b}_1(t) + \omega_1^2 b_1(t) = \omega_1^2 V_{\text{cav}}^{-1/3} q_l(t)\Big(C_{11}^l b_1(t) + \sqrt{\frac{U_0}{U_1}} C_{01}^l b_0(t)\Big) + J_1(t). \tag{5.9}$$

To solve these equations, we need a third EoM for the mechanical mode. The derivation of this differential equation is devoted to the next section.

5.2.2. Equation of Motion for the Displacement Field

To derive an EoM for the displacement field, we have to use the Lagrangian from eqn. 5.5. We will see that the resulting interaction between the GW and the displacement field is determined not only by the tidal force (eqn. 4.32), but also by a back-action term induced by the electromagnetic field itself. The term was first described in [5], but is not discussed in [4].
We start by inserting the perturbed expansions 3.47 and 3.48 into the mechanical Lagrangian 5.5. By considering only the leading order terms, we get

$$\begin{aligned}&\sum_n U_n({e'_n}^2 - {b'}_n^2)\\ &\quad= \sum_n U_n\Big(e_n^2 + 2\sum_{m\neq n}\frac{\omega_n\omega_m}{\omega_m^2-\omega_n^2}\mathcal{C}_{nm}\frac{U_m}{U_n}e_n e_m - b_n^2 + \mathcal{C}_{nn}b_n^2 - 2\sum_{m\neq n}\frac{\omega_n^2}{\omega_m^2-\omega_n^2}\mathcal{C}_{nm}\frac{U_m}{U_n}b_n b_m\Big).\end{aligned}$$

As in the previous chapter, we can assume that only the pump and signal mode contribute to the Lagrangian and all other modes can be neglected. Including the decomposition 3.59 of the connection coefficients, we can write the mechanical Lagrangian as

$$L_{\text{mech}} = U_0(e_0^2 - b_0^2) + U_1(e_1^2 - b_1^2) + \frac{1}{2}M\dot{q}_l^2 - \frac{1}{2}M\omega_l^2 q_l^2 + q_l(f_l + f_l^{\text{ab}}) \tag{5.10}$$

Again, only one mechanical mode with fixed index l is considered. We can see that the displacement is driven by an additional force density given by the back-action

$$f_l^{\text{ab}}(t) := V_{\text{cav}}^{-1/3}\Big(U_0 C_{00}^l b_0^2(t) + U_1 C_{11}^l b_1^2(t) + 2\sqrt{U_0 U_1}C_{01}^l b_0(t)b_1(t)\Big). \tag{5.11}$$

It gives rise to two self-coupling terms and one cross-coupling term, which will later have an influence on the resonance structure of the signal. From eqn. 5.10, it is straightforward to calculate the EoM. We finally end up with

$$\ddot{q}_l(t) + \omega_l^2 q_l(t) = \frac{1}{M}\Big(f_l(t) + f_l^{\text{ba}}(t)\Big). \tag{5.12}$$

Note that we can also derive eqn. 5.8-5.9 from the Lagrangian 5.10 (without the Gertsenshtein current). This must be the case, as both approaches shown here should lead to the same physics, except for the current which appears only in the electromagnetic Lagrangian 5.4. So the formalism is consistent.

5.3. The Full Set of Equations

So far, we have derived the equations 5.8, 5.9 and 5.12 which describe the dynamics of a heterodyne cavity system responding to a passing GW. However, as already shown in [5], there are still some missing components which have to be added by hand. First, we have to include a dissipative terms as in eqn. 3.23 and 3.55. But there is also an additional oscillator driving the cavity which have to be considered. In an idealized case, this external driver should only couple to the pump mode. However, there is always a small leakage to the signal mode which cannot be avoided. As in [43], we denote the coupling of the oscillator the the signal mode as ϵ. A typical value for MAGO is $\epsilon = \mathcal{O}(10^{-7})$.
When we add the additional terms to the Lagrangian, we have to be careful about the correct normalizations and also have to account for the energy loss due to the finite quality factors. The final coupled system of EoM reads

$$\ddot{b}_0 + \frac{\omega_0}{Q_0}\dot{b}_0 + \omega_0^2 b_0 = \omega_0^2 V_{\text{cav}}^{-1/3} q_l \Big(C_{00}^l b_0 + \sqrt{\frac{U_1}{U_0}} C_{01}^l b_1 \Big) + J_0 + \frac{\omega_0}{Q_0}\sqrt{\frac{U_d}{U_0}}\dot{b}_d \tag{5.13}$$

$$\ddot{b}_1 + \frac{\omega_1}{Q_1}\dot{b}_1 + \omega_1^2 b_1 = \omega_1^2 V_{\text{cav}}^{-1/3} q_l \Big(C_{11}^l b_1 + \sqrt{\frac{U_0}{U_1}} C_{01}^l b_0 \Big) + J_1 + \epsilon\frac{\omega_1}{Q_1}\sqrt{\frac{U_d}{U_1}}\dot{b}_d. \tag{5.14}$$

$$\ddot{q}_l + \frac{\omega_l}{Q_l}\dot{q}_l + \omega_l^2 q_l = \frac{1}{M}\Big(f_l + f_l^{\text{ba}} \Big). \tag{5.15}$$

and can be considered, together with eqn. 5.11, as one of the main results of this thesis. In the following chapters, we will solve this set of equations for the special case of a monochromatic GW propagating in z-direction.

5.4. The Projected Current

Before we solve the system 5.13-5.15, we want to take a closer look on the projected current $J_n(t)$. As already discussed, it is not invariant under gauge transformation and we therefore have to choose a gauge which properly describes the physical effects of a passing GW. In chapter 4.4, we argued that the proper detector frame is the correct choice for this task. So inserting the strain 4.26 into eqn. 5.1 yields

$$\begin{aligned}
\rho_{\text{eff}} = j^0_{\text{eff}} &= -\partial_i\big(\frac{1}{2}h_{00}F^{0i}\big) + \partial_i\big(h_{00}F^{0i}\big) = \frac{1}{2}\nabla(h_{00}\vec{E}) \\
j^i_{\text{eff}} &= -\partial_\nu\big(\frac{1}{2}h_{00}F^{i\nu}\big) - \partial_0\big(h_{00}F^{0i}\big) = -\frac{1}{2}\big(\partial_t(h_{00}\vec{E})\big)^i - \frac{1}{2}\big(\nabla\times(h_{00}\vec{B})\big)^i
\end{aligned}$$

In the heterodyne case, the GW couples to the pump mode ($n = 0$), so we can identify the E- and B-field with $\vec{E}_0(t,\vec{x})$ and $\vec{B}_0(t,\vec{x})$. The result is

$$\rho_{\text{eff}}(t,\vec{x}) = \frac{1}{2}\nabla(h_{00}(t,\vec{x})\vec{E}_0(t,\vec{x})) \tag{5.16}$$

$$\vec{j}_{\text{eff}}(t,\vec{x}) = -\frac{1}{2}\partial_t(h_{00}(t,\vec{x})\vec{E}_0(t,\vec{x})) - \frac{1}{2c^2}\nabla\times(h_{00}(t,\vec{x})\vec{B}_0(t,\vec{x})), \tag{5.17}$$

where we turned to SI-units. Before using $\vec{j}_{\text{eff}}$ to calculate the generalized current J_n, we consider the boundaries of the resonator. Since the cavity is assumed to have a superconducting shell, we can argue that the effective current will be compensated by the shell electrons. This is

approximately true because the typical GW frequency is much smaller than the pump mode frequency, so we can use the adiabatic approximation (see also chapter 3.4, where we argued that the shell deformation can be treated as constant in cavity perturbation theory for the same reason). From these considerations, we can deduce the boundary condition $\vec{n} \times \vec{j}_{\text{eff}}(t, \vec{x})|_S = 0$ for the effective current. This allows us to simplify the projected current J_n. Expanding the integrand in eqn. 5.7 as

$$\vec{B}_n(\vec{x})\nabla \times \vec{j}_{\text{eff}}(t, \vec{x}) = -\nabla(\vec{B}_n(\vec{x}) \times \vec{j}_{\text{eff}}(t, \vec{x})) + \vec{j}_{\text{eff}}(t, \vec{x})\nabla \times \vec{B}_n(\vec{x}) \tag{5.18}$$

and using Gauss's theorem, we find

$$J_n(t) = -\frac{c^2}{2U_n}\int_{\partial V_{\text{cav}}} \mathrm{d}\vec{S}\frac{1}{\mu_0}\vec{B}_n \times \vec{j}_{\text{eff}} + \frac{c^2}{2U_n}\int_{V_{\text{cav}}} \mathrm{d}^3x\frac{1}{\mu_0}\vec{j}_{\text{eff}}\nabla \times \vec{B}_n.$$

Due to the boundary condition, we can argue that $\vec{n} \cdot (\vec{B}_n \times \vec{j}_{\text{eff}})|_S = -\vec{B}_n \cdot (\vec{n} \times \vec{j}_{\text{eff}})|_S = 0$, so the surface term vanishes. Applying eqn. 3.15 and inserting the effective current 5.17 yields

$$\begin{aligned} J_n(t) = -\frac{1}{4}\frac{\omega_n}{U_n}\Big[&\int_{V_{\text{cav}}} \mathrm{d}^3x\varepsilon_0\vec{E}_n(\vec{x})(\partial_t h_{00}(t, \vec{x})\vec{E}_0(t, \vec{x})) \\ &+ \int_{V_{\text{cav}}} \mathrm{d}^3x\frac{1}{\mu_0}\vec{E}_n(\vec{x})(\nabla \times (h_{00}(t, \vec{x})\vec{B}_0(t, \vec{x})))\Big] \end{aligned}$$

From now on, we consider the special case of a monochromatic GW propagating in z-direction. That means, we insert the strain 4.26 in the proper detector frame assuming that the GW has the same form as in eqn. 4.17. It is convenient to use complex notation, i.e. to replace $\cos(\omega_g t)$ with $e^{i\omega_g t}$. Although we are so far working in real space, we will convert the differential equations into complex space in chapter 6.1. Then, the strain can be decomposed as

$$h_{00}(t, \vec{x}) = -\frac{\omega_g^2}{2c^2}\big(h_+(x^2 - y^2) + 2h_\times xy\big)e^{i\omega_g t} =: -\frac{\omega_g^2}{2c^2}H_0(\vec{x})e^{i\omega_g t}$$

with $H_0(\vec{x}) = h_+(x^2 - y^2) + 2h_\times xy$. We can also decompose the pump field using eqn. 3.7, i.e. $\vec{E}_0(t, \vec{x}) = e_0(t)\vec{E}_0(\vec{x})$ and $\vec{B}_0(t, \vec{x}) = b_0(t)\vec{B}_0(\vec{x})$. It is sufficient to set $e_0(t) = b_0(t) = e^{i\omega_0 t}$, since the pump field is later supposed to be stabilized. The projected current can be then finally written as

$$J_n(t) = H\sqrt{\frac{U_0}{U_n}}\frac{\omega_g^2}{8c^2}\Big(i\omega_n(\omega_0 + \omega_g)\eta_{0n}^{\text{E}} + \omega_n^2\eta_{0n}^{\text{B}}\Big)e^{i(\omega_0+\omega_g)t} \tag{5.19}$$

where we have defined the normalized overlap factors

$$\eta_{0n}^{\text{E}} := \frac{1}{H\sqrt{U_0U_n}}\int_{V_{\text{cav}}} \mathrm{d}^3xH_0(\vec{x})\varepsilon_0\vec{E}_0(\vec{x})\vec{E}_n(\vec{x}) \tag{5.20}$$

$$\eta_{0n}^{\text{B}} := \frac{1}{H\sqrt{U_0U_n}}\int_{V_{\text{cav}}} \mathrm{d}^3xH_0(\vec{x})\frac{1}{\mu_0}\vec{B}_0(\vec{x})\vec{B}_n(\vec{x}). \tag{5.21}$$

We also have introduced a GW normalization H defined as

$$H := \sqrt{\frac{1}{V_{\text{cav}}}\int_{V_{\text{cav}}} \mathrm{d}^3xH_0^2(\vec{x})}. \tag{5.22}$$

Note that the overlap factors are dimensionless and can in principle be optimized to be of order $\mathcal{O}(1)$. The GW normalization, however, includes the strain and has dimension $[H] = \mathrm{m}^2$. It has a typical order of $\mathcal{O}(\lesssim 10^{-20}\,\mathrm{m}^2)$.
We will need the Fourier transformation of the projected current (eqn. 5.19) in chapter 6.2. It can be written as

$$J_n(\omega) := H\omega_g^2\sqrt{\frac{U_0}{U_n}}\big(\kappa_n\eta_{0n}^{\mathrm{E}} + \lambda_n\eta_{0n}^{\mathrm{B}}\big)2\pi\delta(\omega - (\omega_0 + \omega_g)) \tag{5.23}$$

with coefficients

$$\kappa_n := i\frac{\omega_n}{8c^2}(\omega_0 + \omega_g) \tag{5.24}$$

$$\lambda_n := \frac{\omega_n^2}{8c^2} \tag{5.25}$$

Eqn. 5.24 and 5.25 show, that the couplings of the GW to the electric and magnetic fields are equal for $\omega_n \approx \omega_0 + \omega_g$. For different values, the magnetic coupling remains constant while the electric coupling scales with ω_g. It is important to note that this is an artefact of the long wavelength approximation, where we assumed $\omega_g \ll \omega_0, \omega_1$ (for n=1). The scaling of κ is therefore small in the considered frequency regime. In case it is necessary to describe the Gertsenshtein coupling for GW in the GHz regime, this formalism breaks down and we have to use the full metric expansion 4.23-4.25. This has been done e.g. in [31, 4].

6. Solving the Equations of Motion

In this chapter we want to solve eqn. 5.13-5.15 for a monochromatic GW interacting with the heterodyne cavity detector. We will show, that a full treatment of the dynamics leads to an additional back-action term in the denominator of the Breit-Wigner response of the signal mode. This will lead to a suppressed signal close to the mechanical resonances. We will further calculate all couplings for the MAGO cavity using numerical simulations with COMSOL and CST. We then justify why it is sufficient to consider only one resonant mode in eqn. 5.13-5.15. The calculations presented in this chapter are mainly based [5]. However, we will go into much more detail and make more general assumptions. For example, we will not assume that the diagonal components of the coupling coefficients vanish and also include the Gertsenshtein effect.

6.1. Lorentz Force Detuning

In general, eqn. 5.13-5.15 are very hard to solve. It is therefore expedient to make a couple of assumptions in order to simplify the equations of motion.
We start by neglecting all fast oscillating terms. In particular, we will neglect terms with $e^{i\omega_0 t}$ or $e^{i\omega_1 t}$ in case there is another term oscillating with $e^{i\omega_g t}$. This is justified since we assume $\omega_g \ll \omega_0, \omega_1$ and take the time-average in the end of the calculation, where fast oscillating terms vanish due to the Riemann-Lebesgue lemma.
Another helpful simplification is that we assume the external oscillator to be perfectly resonant to the pump mode and to dominate over the perturbative signal. This is true for general GWs as their signal is more than twenty orders of magnitude weaker as the oscillator amplitude. Within this framework, we can directly solve eqn. 5.13 by setting $b_0(t) = \cos(\omega_0 t)$.
It is further convenient to convert the EoM's into complex notation. To properly convert the quadratic terms, we use the identity

$$\mathrm{Re}\big(A\big)\mathrm{Re}\big(B\big) = \frac{1}{2}\mathrm{Re}\big(AB + AB^*\big).$$

Since all functions in eqn. 5.13-5.15 are supposed to be approximately monochromatic, we can factorize out the peak frequency from the solutions. An appropriate ansatz is therefore given by

$$b_0(t) = b_d(t) = \mathrm{Re}\big(e^{i\omega_0 t}\big) \tag{6.1}$$
$$b_1(t) = \mathrm{Re}\big(A_1(t)e^{i(\omega_0+\omega_g)t}\big) \tag{6.2}$$
$$q_l(t) = \mathrm{Re}\big(Q_l(t)e^{i\omega_g t}\big) \tag{6.3}$$
$$f_l(t) = \mathrm{Re}\big(F_l(t)e^{i\omega_g t}\big) \tag{6.4}$$
$$J_1(t) = \mathrm{Re}\big(K_1(t)e^{i(\omega_0+\omega_g)t}\big). \tag{6.5}$$

Inserting these assumptions into the right hand side of eqn. 5.15 yields

$$\frac{1}{M}\Big[F_l(t)e^{i\omega_g t} + \frac{V_{\text{cav}}^{-1/3}}{2}U_0 C_{00}^l\big(1+e^{i2\omega_0 t}\big) + \frac{V_{\text{cav}}^{-1/3}}{2}U_1 C_{11}^l\big(|A_1(t)|^2 + A_1^2(t)e^{i2(\omega_0+\omega_g)t}\big) + V_{\text{cav}}^{-1/3}\sqrt{U_0U_1}C_{01}^l\big(A_1(t)e^{i(2\omega_0+\omega_g)t} + A_1(t)e^{i\omega_g t}\big)\Big].$$

Neglecting all fast oscillating terms, we can rearrange eqn. 5.15 as[1]

$$\ddot{Q}_l(t) + \alpha_l\dot{Q}_l(t) + \beta_l\omega_l^2 Q(t) = \frac{1}{M}\Big[(F_l(t)+S(t))e^{i\omega_g t} + \frac{V_{\text{cav}}^{-1/3}}{2}U_0C_{00}^l\Big]e^{-i\omega_g t} \tag{6.6}$$

with the function

$$S(t) := \frac{V_{\text{cav}}^{-1/3}}{2}\big(U_1C_{11}^l|A_1(t)|^2e^{-i\omega_g t} + 2\sqrt{U_0U_1}C_{01}^lA_1(t)\big). \tag{6.7}$$

We will need $S(t)$ later. For now, we want to investigate the influence of the constant term $V_{\text{cav}}^{-1/3}U_0C_{00}^l$. The coefficients α_l and β_l are given by

$$\alpha_l := 2i\omega_g + \frac{\omega_l}{Q_l} \tag{6.8}$$

$$\beta_l := \omega_l^2 - \omega_g^2 + i\omega_g\frac{\omega_l}{Q_l}. \tag{6.9}$$

Performing a Fourier transformation of eqn. 6.6 gives

$$Q_l(\omega) = \frac{1}{M}\frac{1}{\beta_l - \omega^2 + i\omega\alpha_l}\Big(F_l(\omega) + S(\omega) + 2\pi\frac{V_{\text{cav}}^{-1/3}}{2}U_0C_{00}^l\delta(\omega+\omega_g)\Big) \tag{6.10}$$

We can transform this back into time space. The last term gives rise to a constant deformation of the cavity walls. We find

$$q_l(t) = q_l'(t) + \frac{V_{\text{cav}}^{-1/3}U_0C_{00}^l}{2M}$$

with $q_l'(t)$ defined as the time-dependent part of $q_l(t)$ given by

$$q_l'(t) := \text{Re}\Big(\frac{1}{2\pi M}\int \text{d}\omega\frac{F_l(\omega)+S(\omega)}{\beta_l-\omega^2+i\omega\alpha_l}e^{i(\omega+\omega_g)t}\Big).$$

A constant and small shift leads to a change of the eigenmodes according to cavity perturbation theory (see chapter 3.4). However, this shift is not time-dependent and can be therefore simply absorbed into the eigenfrequency and eigenmodes of the cavity. Experimentally, we have to tune the oscillator and readout such that they stay on resonant with the pump and signal mode respectively.
The constant shift of the cavity walls due to the electromagnetic fields is known as *Lorentz Force Detuning*. It is mentioned in [3] as well, but it is not further specified there. The shift of the eigenfrequencies can be calculated and reads

$$\omega_0' = \omega_0\Big(1 - \frac{1}{2}\frac{V_{\text{cav}}^{-1/3}U_0C_{00}^l}{2M}C_{00}^l\Big) \qquad \omega_1' = \omega_1\Big(1 - \frac{1}{2}\frac{V_{\text{cav}}^{-1/3}U_0C_{00}^l}{2M}C_{11}^l\Big),$$

[1] We use the same symbol Q_l for the displacement and the quality factor. To distinguish them, we always write $Q_l(t)$ or $Q_l(\omega)$ to show that the displacement is time-dependent while the quality factor Q_l is constant in time.

so also the frequency difference $\omega_1 - \omega_0$ changes.
In our further analysis, however, we will ignore the Lorentz Force Detuning and simply assume that the shift is already contained in b_0, b_1 and ω_0, ω_1. An immediate consequence is that the remaining wall displacement is only governed by the GW and hence, $q_l(t)$ and $b_1(t)$ are of order $\mathcal{O}(h)$. In leading order, we can therefore neglect the first term of $S(t)$ in eqn. 6.7. The solution 6.10 for $Q_l(\omega)$ can be then written compactly as

$$Q_l(\omega) = \frac{1}{M}\frac{F_l(\omega) + V_{\text{cav}}^{-1/3}\sqrt{U_0 U_1}C_{01}^l A_1(\omega)}{\beta_l - \omega^2 + i\omega\alpha_l}. \tag{6.11}$$

6.2. The Signal PSD for Monochromatic Gravitational Waves

In order to find a signal PSD, the remaining task is to solve eqn. 5.14 together with eqn. 6.11. Since we have absorbed the back-action of the signal mode into the eigenmodes and eigenfrequencies, we argued in the previous chapter that both q_l and b_1 are of order $\mathcal{O}(h)$ now. However, this is strictly speaking not correct since the oscillator has a small coupling to the signal mode as well. So we also expect a field of order ϵ in the signal mode, which oscillates with frequency ω_0. The readout is assumed to be able to separate this oscillation from the GW frequency at $\omega_0 + \omega_g$. That means, we can neglect the first term of eqn. 5.14 as it is of order $\mathcal{O}(h^2)$.
By the same argument, we could also neglect the oscillator-to-signal mode coupling, i.e. the last term in eqn. 5.14. But, it is reasonable to keep this term as there could be phase noise according to the oscillator which we want to consider later. Hence, we have to solve

$$\ddot{b}_1(t) + \frac{\omega_1}{Q_1}\dot{b}_1(t) + \omega_1^2 b_1(t) = V_{\text{cav}}^{-1/3}\sqrt{\frac{U_0}{U_1}}\omega_1^2 C_{01}^l q_l(t) b_0(t) + J_1(t) + \varepsilon\frac{\omega_1}{Q_1}\sqrt{\frac{U_d}{U_1}}\dot{b}_d(t).$$

By converting it into complex notation and using eqn. 6.1-6.5, we can rewrite this differential equation as

$$\begin{aligned}&\ddot{A}_1(t) + \alpha_1\dot{A}_1(t) + \beta_1 A_1(t)\\ &\quad= \Big(\sqrt{\frac{U_0}{U_1}}\gamma_1 Q_l(t)e^{i(\omega_0+\omega_g)t} + K_1(t)e^{i(\omega_0+\omega_g)t} + \epsilon i\omega_0\frac{\omega_1}{Q_1}\sqrt{\frac{U_d}{U_1}}e^{i\omega_0 t}\Big)e^{-i(\omega_0+\omega_g)t}\end{aligned}$$

with constants

$$\alpha_1 := \frac{\omega_1}{Q_1} + 2i(\omega_0 + \omega_g) \tag{6.12}$$

$$\beta_1 := \omega_1^2 - (\omega_0 + \omega_g)^2 + i\frac{\omega_1}{Q_1}(\omega_0 + \omega_g) \tag{6.13}$$

$$\gamma_1 := V_{\text{cav}}^{-1/3}\omega_1^2 C_{01}^l. \tag{6.14}$$

A Fourier transformation leads to

$$A_1(\omega)(-\omega^2 + i\omega\alpha_1 + \beta_1) = \sqrt{\frac{U_0}{U_1}}\gamma_1 Q_l(\omega) + K_1(\omega) + i2\pi\epsilon\frac{\omega_1}{Q_1}\omega_0\sqrt{\frac{U_d}{U_1}}\delta(\omega + \omega_g).$$

This equation can be easily solved by using eqn. 6.11. The result for $A_1(\omega)$ reads

$$A_1(\omega) = \sqrt{\frac{U_0}{U_1}}\frac{\gamma_1 F_l(\omega)}{M\Lambda_1(\omega)} + \frac{J_1(\omega + (\omega_0 + \omega_g))}{\Lambda_2(\omega)} + i2\pi\epsilon\frac{\omega_1}{Q_1}\omega_0\sqrt{\frac{U_d}{U_1}}\frac{\delta(\omega + \omega_g)}{\Lambda_2(\omega)}, \tag{6.15}$$

where we have expressed the projected Gertsenshtein current again in terms of $J_1(\omega)$. The resonance structures are given in terms of $\Lambda_1(\omega)$ and $\Lambda_2(\omega)$. We obtain

$$\Lambda_1(\omega) := \big(\beta_1 - \omega^2 + i\omega\alpha_1\big)\big(\beta_l - \omega^2 + i\omega\alpha_l\big) - \gamma_1\gamma_l \tag{6.16}$$

$$\Lambda_2(\omega) := \Lambda_1(\omega)\big(\beta_l - \omega^2 + i\omega\alpha_l\big)^{-1} \tag{6.17}$$

with the new constant

$$\gamma_l = \frac{1}{M} V_{\mathrm{cav}}^{-1/3} U_0 C_{01}^l. \tag{6.18}$$

We can immediately see a strong damping in the resonance function 6.16 due to the term $\gamma_1\gamma_l$. It appears because we have included the back-action of the electromagnetic field from the passing GW in our calculation, which gives an additional contribution to the displacement. Note that this phenomenon was already considered in [5], but not in [4].
We can recast eqn. 6.15 in terms of $b_1(\omega) = A_1(\omega - (\omega_0 + \omega_g))$ and plug in eqn. 4.32 and 5.23, i.e.

$$b_1(\omega) = \sqrt{\frac{U_0}{U_1}}\Bigg(- \frac{\omega_g^2}{2}\frac{V_{\mathrm{cav}}^{1/3}\gamma_1(h_+\Gamma_+ + h_\times\Gamma_\times)}{\Lambda_1(\omega - (\omega_0+\omega_g))} + H\omega_g^2\frac{\kappa_1\eta_{01}^{\mathrm{E}} + \lambda_1\eta_{01}^{\mathrm{B}}}{\Lambda_2(\omega - (\omega_0+\omega_g))}\Bigg) 2\pi\delta(\omega - (\omega_0+\omega_g)) + i\epsilon\frac{\omega_1}{Q_1}\omega_0\sqrt{\frac{U_d}{U_1}}\frac{2\pi\delta(\omega-\omega_0)}{\Lambda_2(\omega - (\omega_0+\omega_g))}$$

With eqn. 3.27-3.28 and 3.30, we can translate this result into a PSD. Note that, using the time average, we find

$$\langle b_1^2(t)\rangle = \langle \mathrm{Re}\big(A_1(t)e^{i(\omega_0+\omega_g)t}\big)^2\rangle = \frac{1}{2}\langle \mathrm{Re}\big(|A_1(t)|^2 + A_1^2(t)e^{i2(\omega_0+\omega_g)t}\big)\rangle \approx \frac{1}{2}\langle |A_1(t)|^2\rangle, \tag{6.19}$$

where fast oscillating terms are again neglected. The signal PSD then yields

$$S_{\mathrm{sig}}(\omega) = \frac{\omega_1\omega_g^4 U_0}{Q_{\mathrm{cpl}}}\Bigg|\underbrace{\frac{1}{2}\frac{\omega_1^2 C_{01}^l(h_+\Gamma_+ + h_\times\Gamma_\times)}{\Lambda_1(\omega - (\omega_0+\omega_g))}}_{\text{Mechanical Coupling}} - \underbrace{\frac{H(\kappa_1\eta_{01}^{\mathrm{E}} + \lambda_1\eta_{01}^{\mathrm{B}})}{\Lambda_2(\omega - (\omega_0+\omega_g))}}_{\text{Gertsenshtein Coupling}}\Bigg|^2 4\pi^2\delta(\omega - (\omega_0+\omega_g)). \tag{6.20}$$

It scales, apart from the complicated resonance structure, with $S_{\mathrm{sig}} \sim \omega_g^4$, so the signal increases for higher frequencies. Eqn. 6.20 also highlights the different couplings of the GW to the heterodyne system. In the mechanical term, we have two couplings for the two GW polarizations and in the Gertsenshtein term, we distinguish between the coupling to the E- and B-Field.
The oscillator PSD can be written independently because it has a peak at the pump mode frequency and is therefore well separated from the signal. We find

$$S_{\mathrm{osc}}(\omega) = \epsilon^2\frac{Q_1}{Q_{\mathrm{cpl}}}\frac{\omega_1^3}{Q_1^3}\omega_0^2\frac{U_d S_{b_d}(\omega)}{|\Lambda_2(\omega - (\omega_0+\omega_g))|^2}, \tag{6.21}$$

where we kept the spectral density for $S_{b_d}(\omega)$ general for later purposes when we consider phase noise from the oscillator (see chapter 7.4). For a monochromatic source, we simply have $S_{b_d}(\omega) = 4\pi^2\delta(\omega - \omega_0)$.
To conclude this discussion, we finally integrate eqn. 6.20 using eqn. 3.25 to get the total signal power. The assumed delta-nature of the GW spectrum simplifies the resonance structure and we end up with

$$P_{\mathrm{sig}} = \frac{\omega_1}{Q_{\mathrm{cpl}}}\omega_g^4 U_0\left|\frac{1}{2}\frac{\omega_1^2 C_{01}^l(h_+\Gamma_+ + h_\times\Gamma_\times)}{\beta_1\beta_l - \gamma_1\gamma_l} - \frac{\beta_l H(\kappa_1\eta_{01}^{\mathrm{E}} + \lambda_1\eta_{01}^{\mathrm{B}})}{\beta_1\beta_l - \gamma_1\gamma_l}\right|^2. \tag{6.22}$$

6.3. Gravitational Wave - Mechanical Coupling

In this chpter we investigate the coupling between the GW and the mechanical eigenmodes of the cavity. We already computed the corresponding coupling parameters in chapter 4.5. They are given by

$$\Gamma_+ := \frac{V_{\text{cav}}^{-1/3}}{M} \int_{V_{\text{cav}}} \mathrm{d}^3x \rho(\vec{x}) \big(x\xi_{l,x}(\vec{x}) - y\xi_{l,y}(\vec{x})\big)$$
$$\Gamma_\times := \frac{V_{\text{cav}}^{-1/3}}{M} \int_{V_{\text{cav}}} \mathrm{d}^3x \rho(\vec{x}) \big(x\xi_{l,y}(\vec{x}) + y\xi_{l,x}(\vec{x})\big).$$

Note that the displacement field should be appropriately normalized (see eqn. 3.53). For an arbitrary field $\xi'_l(\vec{x})$, this can be done by calculating

$$\vec{\xi}_l(\vec{x}) = \vec{\xi}'_n(\vec{x}) \times \left(\frac{1}{M} \int_{V_{\text{cav}}} \mathrm{d}^3x \vec{\xi}^2_n(\vec{x}) \rho(\vec{x}) \right)^{-\frac{1}{2}}. \tag{6.23}$$

From general considerations (see e.g. [38]), it is known that GWs have the strongest coupling to the quadrupole modes of a spherical cavity. For MAGO, we therefore expect to find a few well defined modes with particularly strong coupling. Furthermore, the GW is uniform over the cavity volume due to the long wavelength approximation. The mechanical modes, instead, have much shorter wavelength and the number of nodes increases for higher eigenfrequencies. This suppresses the overlap integral and we expect a scaling such as [4]

$$|\Gamma_i(\omega_l)| \sim \frac{1}{\omega_l^2}.$$

However, the MAGO cavity is not a sphere and the GW will therefore have at least a small

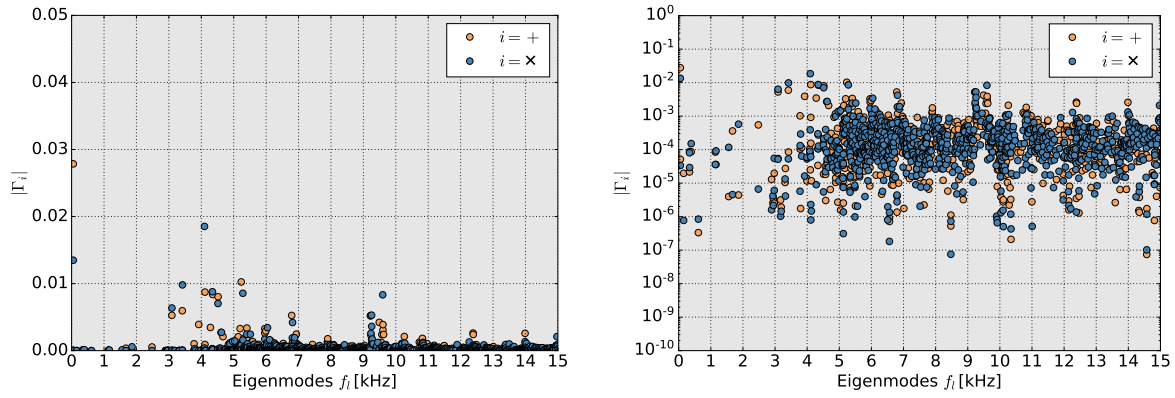

(a) *Linear Plot* **(b)** *Logarithmic Plot*

Figure 6.1.: *This plot shows the coupling coefficients for the coupling of a GW propagating in z-direction of the cavity to the mechanical eigenmodes. (a): Linear plot of the coupling: It can be seen that there are a few well defined modes with particularly strong coupling. They correspond to the quadrupole modes. (b): Exponential plot of the coupling which better shows the distribution of all modes.*

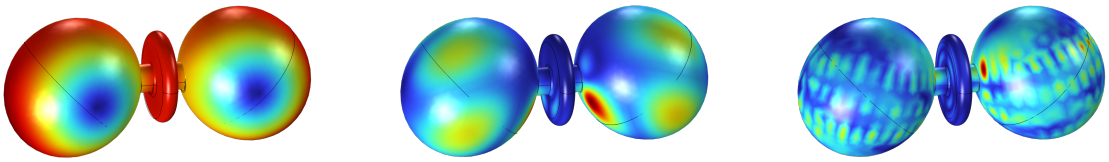

(a) $\omega_l = 0.051\,kHz$, $\Gamma_+ = -0.028$ **(b)** $\omega_l = 4.098\,kHz$, $\Gamma_\times = -0.019$ **(c)** $\omega_l = 9.597\,kHz$, $\Gamma_\times = -0.008$

Figure 6.2.: *This plot shows the modes with the strongest coupling to a GW propagating in z-direction, which corresponds to the direction along the central cylinder. The red regions are strongly displaced while the blue ones have a smaller offset. We show the displacement in arbitrary units, since the field is normalized in the pre-processing. (a): Lowest lying mode with* $\omega_l = 0.051\,kHz$ *and a strong coupling* $|\Gamma_+| = 0.028$*: It is a mode of the coupled system and cannot be directly identified with a mode on the sphere. (b): Quadrupolar mode with* $\omega_l = 4.098\,kHz$ *and* $|\Gamma_\times| = 0.019$*: This is an example of an uncoupled mode which corresponds to spherical eigenmodes. (c): Higher order mode with* $\omega_l = 9.597\,kHz$ *and* $|\Gamma_\times| = 0.008$*: The displacement field changes on very small scales, so there might already be subtle numerical issues which we could not yet identify. To confirm the results, an analysis with higher resolution is needed, which was not the scope of this master thesis.*

coupling to all modes. We could therefore search for differences and similarities between the mechanical modes of MAGO-like and spherical cavities. For this reason, we did a numerical evaluation of eqn. 4.30 and eqn. 4.31 for the first 1,000 mechanical eigenmodes. The displacement fields were computed with COMSOL. Both for reasons of time and data size, we were forced to use a rough grid ($N_x \times N_y \times N_z = 30 \times 30 \times 90$) for the displacement field. It turned out that this resolution was sufficient for all modes up to $\sim 15\,\mathrm{kHz}$, which corresponds to the first 860 eigenmodes. We had to discard all higher solutions where the number of the wave nodes was too large to be resolved.

We show the results of the analysis in figure 6.1 both in a linear and a logarithmic plot. In the linear plot (fig. 6.1a), we can see that there are a few well defined modes that strongly couple to the incoming GW. Furthermore, the coupling strength of these modes drops towards higher frequencies. In the logarithmic plot (fig. 6.1b), this decrease is less pronounced, but the distribution of the couplings is better resolved.

It is again important to note that we only consider GWs that propagate along the z-axis of the cavity. For future analysis, it is important to take GWs from other directions into account as well. For generally coupled spheres, this has already been done in [3]. It was not within the scope of this master thesis to do the same for the MAGO geometry and has to be postponed to future work.

6.4. Mechanical - Electromagnetic Coupling

As discussed in detail in chapter 3.5, the coupling between the mechanical displacement and the electromagnetic modes is governed by the dimensionless connection coefficient

$$C_{01}^{l} = \frac{V_{\mathrm{cav}}^{1/3}}{2\sqrt{U_0 U_1}} \int_{\partial V_{\mathrm{cav}}} \mathrm{d}\vec{S} \cdot \vec{\xi}_l(\vec{x}) \Big[\frac{1}{\mu_0} \vec{B}_0(\vec{x}) \vec{B}_1(\vec{x}) - \epsilon_0 \vec{E}_0(\vec{x}) \vec{E}_1(\vec{x}) \Big]. \tag{6.24}$$

Note that, unlike the other couplings, it is described by a surface integral. It can be solved numerically by using the approximation

$$C_{01}^{l} \approx \frac{V_{\mathrm{cav}}^{1/3}}{2\sqrt{U_0 U_1}} \int_{i=1}^{N} \frac{A_{\mathrm{cav}}}{N} \Delta_l(\vec{x}_i) \Big[\frac{1}{\mu_0} \vec{B}_n(\vec{x}_i) \vec{B}_m(\vec{x}_i) - \varepsilon_0 \vec{E}_n(\vec{x}_i) \vec{E}_m(\vec{x}_i) \Big], \tag{6.25}$$

where we discretize the cavity as a lattice with N points. The displacement Δ_l is given by

$$\Delta_l(\vec{x}_i) = \vec{n}(\vec{x}_i) \cdot \vec{\xi}_l(\vec{x}_i),$$

where $\vec{n}$ is the shell normal field and $\vec{\xi}$ is normalized corresponding to eqn. 6.23.
It is argued in [4] that the mechanical modes couple to the electromagnetic modes through the cavity surface and therefore allow for a frequency independent scaling, i.e. $|C_{01}^{l}(\omega_l)|^2 \sim 1$. Thus, there are also mechanical modes at higher orders with large coupling $|C_{01}^{l}|^2 \sim \mathcal{O}(1)$. This is different to the GW-electromagnetic couplings that we discussed in the previous chapter, which decrease for higher modes.
As for the GW-mechanical coupling, we have plotted the first 860 coupling coefficients for the TE_{011} mode of the MAGO cavity in figure 6.3. The scaling independence is not clearly

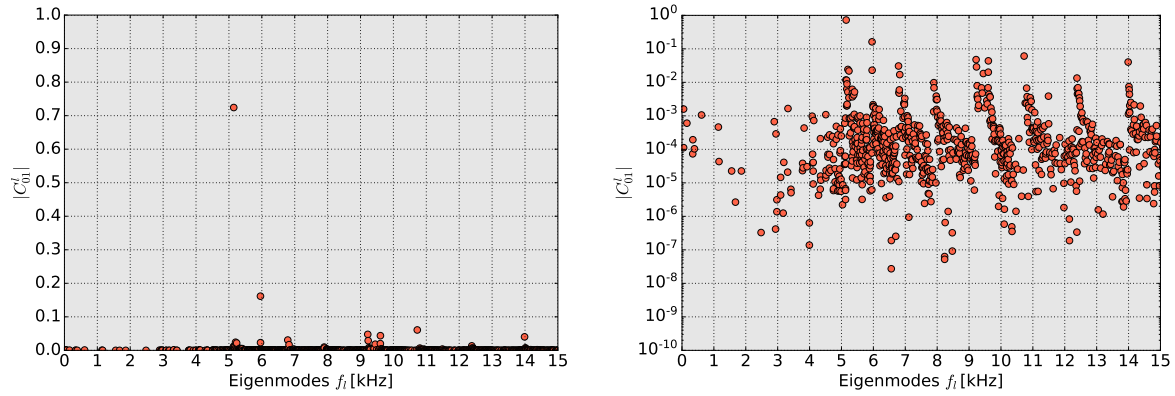

(a) *Linear Plot* **(b)** *Logarithmic Plot*

Figure 6.3.: *This plot shows the connection coefficients for the coupling between the mechanical and electromagnetic modes. We show the coefficients for the first 860 mechanical modes and the symmetric and antisymmetric fields of the electromagnetic TE_{011} mode. (a): Linear plot of the coupling: It can be seen that most couplings are very small with one clear outlier at $\omega_l = 5.147\,kHz$. (b): Exponential plot of the coupling: Up to $\sim 5\,kHz$, the couplings are randomly distributed. Above, we can see a clear pattern and a higher mode density, which could correspond to spherical modes of the two cells.*

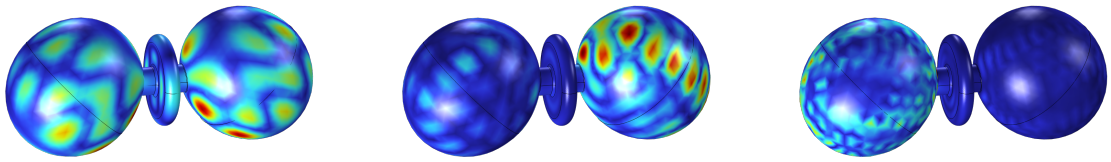

(a) $\omega_l = 5.147\,kHz$, $C_{01}^l = 0.724$ **(b)** $\omega_l = 5.958\,kHz$, $C_{01}^l = 0.162$ **(c)** $\omega_l = 10.726\,kHz$, $C_{01}^l = 0.061$

Figure 6.4.: *This plot shows the mechanical modes with the strongest coupling to the electromagnetic TE_{011} modes. The red regions are strongly displaced while the blue ones have a smaller offset. We show the displacement in arbitrary linear units, since the field is normalized in pre-processing. (a): This mode with $\omega_l = 5.147\,kHz$ has a surprisingly strong coupling of $C_{01}^l = 0.724$, which is much higher then all other couplings. We do not provide a further analysis here, but we note that a high symmetry together with an optimal match between the peak displacement and the B-field amplitudes could be responsible for the high overlap. (b): Higher mode with $\omega_l = 5.958\,kHz$ and $C_{01}^l = 0.162$. (c): Very high mode with $\omega_l = 10.726\,kHz$ and $C_{01}^l = 0.061$: Note that the small scaling of the displacement field could cause numerical errors and the calculation may not be sufficiently accurate.*

pronounced and there is one considerable outlier at $\omega_l = 5.147\,\mathrm{kHz}$. We show the modes of the strongest couplings in figure 6.4.
The logarithmic plot (figure 6.3b) shows that the couplings are randomly distributed up to 5 kHz. Above, the density suddenly increases and the distribution shows an underlying pattern. A further analysis of the behaviour was not the scope of this master thesis and has to be postponed to future work. However, a yet speculative explanation is that the low modes correspond to modes of the full system whereas the higher ones (above $\sim 5\,\mathrm{kHz}$) could be identified with spherical modes. The behaviour was already expected by the MAGO collaboration [2], although they did not provide simulations of their own.
It should be noted that three different software tools were used to evaluate eqn. 6.25. The electromagnetic fields are simulated with CST whereas COMSOL is used for the mechanical displacement. Finally, the sum is calculated with Python. This procedure is inefficient and in the future, it is advisable to make the calculations with only one program. It would make the analysis much faster such that also other properties of the eigenmodes could be analyzed without considerable effort.

6.5. Gravitational Wave - Electromagnetic Coupling

Finally, we also include an analysis of the Gertsenshtein coupling. As shown in chapter 5.4, the coupling can be parametrized by two overlap factors

$$\eta_{01}^{\mathrm{E}} := \frac{1}{H\sqrt{U_0 U_1}} \int_{V_{\mathrm{cav}}} \mathrm{d}^3x H_0(\vec{x}) \varepsilon_0 \vec{E}_0(\vec{x}) \vec{E}_1(\vec{x}) \tag{6.26}$$

$$\eta_{01}^{\mathrm{B}} := \frac{1}{H\sqrt{U_0 U_1}} \int_{V_{\mathrm{cav}}} \mathrm{d}^3x H_0(\vec{x}) \frac{1}{\mu_0} \vec{B}_0(\vec{x}) \vec{B}_1(\vec{x}). \tag{6.27}$$

Since the electromagnetic field is fixed to the symmetric and antisymmetric TE_{011}-mode, the overlap factors depend on the GW only. Again, we assume that the GW propagates along the z-direction and postpone an analysis of other directions to future work.
We can evaluate the integrals 6.26 and 6.27 numerically using the E- and B-fields from the CST simulation. It is instructive to choose a fixed polarization, such that we have four different values

$$\eta_{01}^{\mathrm{E},+} \approx 0.15 \qquad \eta_{01}^{\mathrm{E},\times} \approx 0.23 \qquad \eta_{01}^{\mathrm{B},+} \approx 0.32 \qquad \eta_{01}^{\mathrm{B},\times} \approx -0.08.$$

Note that the overlap factors can also become negative. The numerical calculation confirms that the couplings are of order $\mathcal{O}(0.1)$ for both polarizations. For the sensitivity estimates, we assume a mixed polarization and set $\eta_{01}^{\mathrm{E,B}} = 0.2$.
For the signal power, the strain norm H is important as well. It is given in eqn. 5.22 and can be parametrized for a GW propagating in z-direction as

$$H^{+} = h_{+} \times \sqrt{\frac{1}{V_{\mathrm{cav}}} \int_{V_{\mathrm{cav}}} \mathrm{d}^3x (x^2 - y^2)^2} \approx h_{+} \times 12.08\,\mathrm{m}^2$$
$$H^{\times} = h_{\times} \times \sqrt{\frac{1}{V_{\mathrm{cav}}} \int_{V_{\mathrm{cav}}} \mathrm{d}^3x (2xy)^2} \approx h_{\times} \times 12.26\,\mathrm{m}^2,$$

where we have distinguished between the different polarizations. We will use $h_{+} = h_{\times} =: h_0$ and $H = H^{+} = H^{\times} = h_0 \times 12\,\mathrm{m}^2$ in the remaining analysis.

6.6. A Comment on Multiple Modes

So far we assumed that the signal power is driven only by one mechanical mode. In the experiment, however, we expect many different modes to contribute. This has important effects on the signal power and on the damping term $\gamma_1\gamma_l$.
From the analytic perspective, it is not sufficient to just add up the signal powers of the individual modes, as the resonant functions change as well. A careful reanalysis of the calculations shown in chapter 5 and 6 for multiple modes yields

$$\Lambda_1^k(\omega) = (\beta_1 - \omega^2 + i\omega\alpha_1)(\beta_k - \omega^2 + i\omega\alpha_k) - (\beta_k - \omega^2 + i\omega\alpha_k) \sum_l \frac{\gamma_l\gamma_1}{\beta_l - \omega^2 + i\omega\alpha_l}$$
$$\Lambda_2(\omega) = \beta_1 - \omega^2 + i\omega\alpha_1 - \sum_l \frac{\gamma_l\gamma_1}{\beta_l - \omega^2 + i\omega\alpha_l},$$

where k labels the resonance function for the fixed eigenmode k. For simplicity, we assumed that there is always one specific mode that dominates the signal. This allows us to consider only the $k = l$-terms in the sum and to calculate the total power by adding up the most dominant modes. However, it should be noted that a more detailed analysis is required here, which we postpone to future work.

6.7. Signal Power

In this chapter, we provide numerical calculations for the total noise power. As in [4], we assume $h_0 = 10^{-20}$, which is a rather optimistic strain[2]. An overview about all parameters that have

[2] Note that the highest strain measured in GW interferometers is $h_0 \sim \mathcal{O}(10^{-21})$.

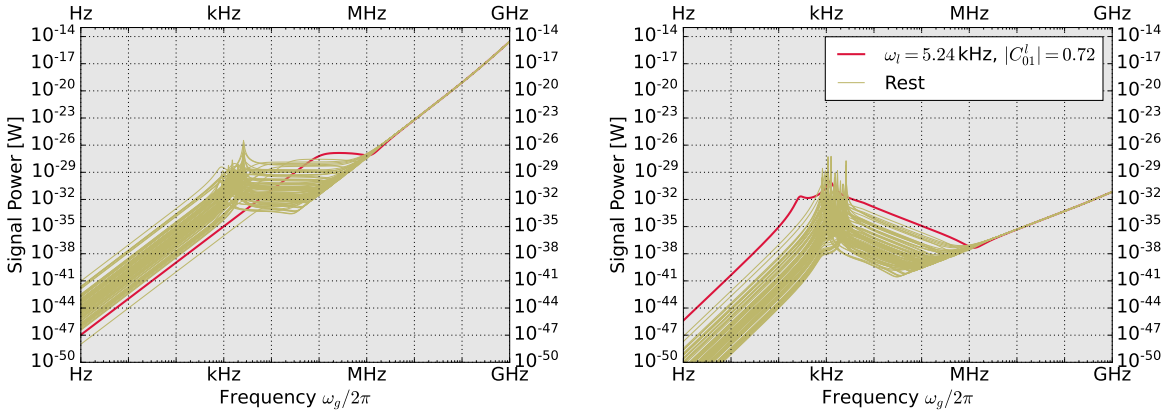

(a) *Scanning* **(b)** *Broadband*

Figure 6.5.: *Signal power for the* 98 *modes with the strongest couplings. The mode with highest coupling* $|C_{01}^l| \approx 0.72$ *dominates in the broadband experiment, but not in the scanning setup.*

been used can be found in Appendix E.

First of all, we analyse the contributions of the various mechanical eigenmodes to the signal. Without damping, it can be shown from general considerations that the mode with the strongest coupling to the GW should dominate. In order to investigate whether this is also the case when damping is included, we have calculated the signal power (eqn. 6.22) for the 98 eigenmodes with the largest couplings[3] for $|C_{01}^l|$, $|\Gamma_+|$ and $|\Gamma_\times|$. The result is shown in figure 6.5. We see that there is no mode that dominates over the whole frequency space. For instance, the mode with the strongest coupling ($|C_{01}^l| \approx 0.72$ at $\omega_l \approx 5.24\,\mathrm{kHz}$) only dominates in the $100\,\mathrm{kHz} - 1\,\mathrm{MHz}$ range. So the damping term $\gamma_l\gamma_1$ has a strong influence on the hierarchy of contributions to the total signal from different modes. Since it is $\gamma_1\gamma_l \sim |C_{01}^l|^2$, this is not surprising because modes with high couplings are also considerably damped.

Note that above $\sim 1\,\mathrm{MHz}$, the Gertsenshtein effect starts to dominate and the mechanical coupling becomes irrelevant. This behaviour can be found for both the scanning as well as the broadband approach, where the frequency difference is held fixed at 50 Hz, which corresponds to the lowest lying mechanical mode. This is different to the results of [4], where the mechanical coupling dominates over the full frequency range. However, [4] assumed idealized coupling parameters ($\sim \mathcal{O}(1)$) and neglected the damping. In figure 6.6, we show the results with and without the damping term in the resonance function. Both the mechanical and Gertsenshtein signals are shown for the simulated couplings and a more optimistic case where we assumed $|C_{01}^l| = 1$ and $|\Gamma_+| = |\Gamma_\times| = 0.5$ for one mode at $\omega_l = 5\,\mathrm{kHz}$[4]. We see that the latter leads to a mechanical signal that is about six orders of magnitude stronger than the simulations. A careful optimization of the cavity design in order to enhance the couplings can therefore lead to a much better sensitivity. However, it has to be noted that the mechanical noise will also increase. We will put that into account in chapter 8.

Furthermore, since the Gertsenshtein effect is independent of the mechanical couplings, we can see that it is much more dominant above 1 MHz for the simulated values. In the optimistic

[3] More precisely, we have chosen all mechanical eigenmodes with $|C_{01}^l| > 0.001$, $|\Gamma_+| > 0.0001$ and $|\Gamma_\times| > 0.0001$.
[4] Note that we will later keep the simulated values for the mechanical noise.

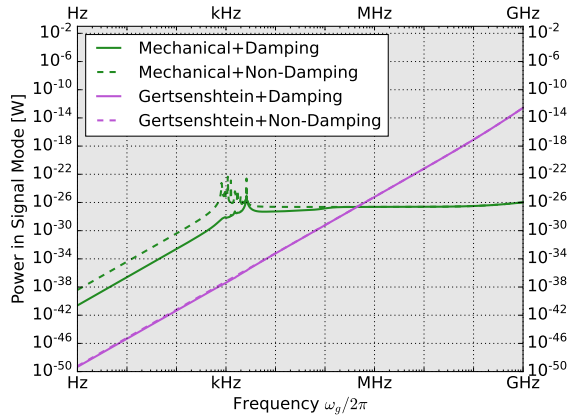

(a) *Simulated Values*
98 strongest couplings

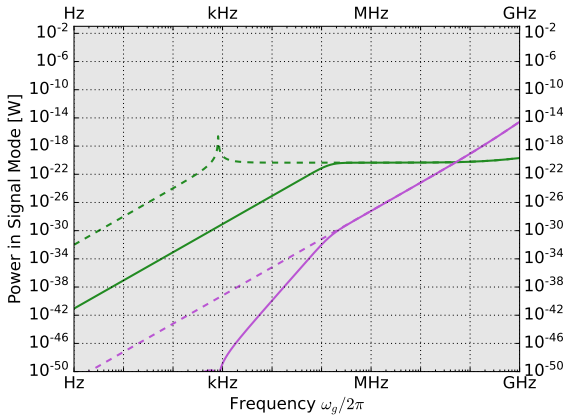

(b) *Optimistic case*
$|C^l_{01}| = 1$, $|\Gamma_+| = |\Gamma_\times| = 0.5$.

Figure 6.6.: *Signal power for the mechanical and the Gertsenshtein coupling. We show the results for both the damping and the non-damping case. (a): Simulated values for the couplings: The Gertsenshtein effect starts to dominate already at* $\sim 1\,MHz$*. (b): Optimistic coupling (for* $\omega_l = 5\,kHz$*): The signal is about six orders of magnitude stronger at higher frequencies and the Gertsenshtein effect, dominates above* $\sim 100\,MHz$*. Note that the influence of the damping on the Gertsenshtein effect is considerably stronger for the optimistic values.*

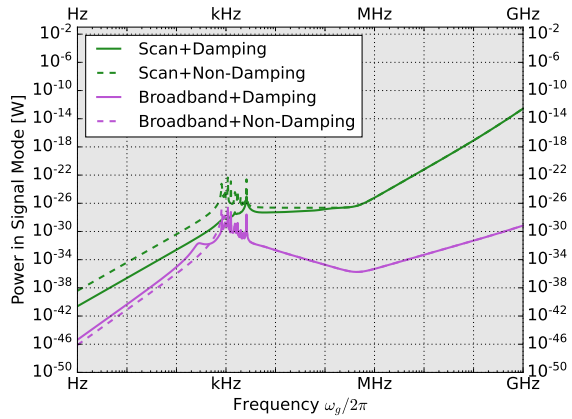

(a) *Simulated Values*
98 strongest couplings

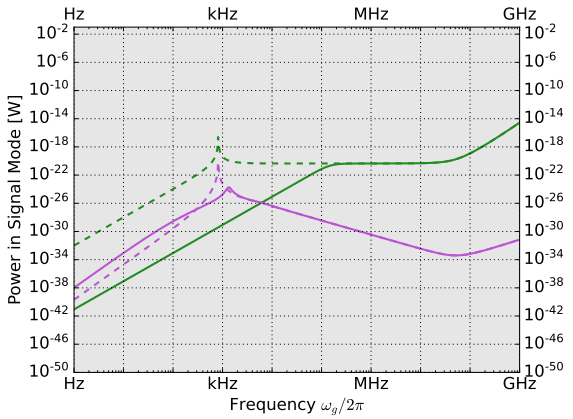

(b) *Optimistic case*
$|C^l_{01}| = 1$, $|\Gamma_+| = |\Gamma_\times| = 0.5$.

Figure 6.7.: *Signal power for the combined couplings. We show the results for a scanning and broadband (*$\omega_l = 5.24\,kHz$*) experiment and distinguish between the damping and non-damping case. (a): Simulated values for the couplings: One remarkable result is that the damping can enhance the signal in the broadband case. (b): Optimistic coupling (for* $\omega_L = 5\,kHz$*). The signal is considerably stronger, in particular for the broadband measurement.*

case, it starts to dominate much later at $\sim 100\,\mathrm{MHz}$. This explains, why the results of [4], where optimistic values based on ideal spherical cavities are chosen, are different. It should be noted that the long wavelength approximation breaks down at $\sim 1\,\mathrm{GHz}$ (see chapter 4.4), so the predicted Gertsenshtein signal may not be sufficiently accurate at higher frequencies. We postpone a detailed analysis to future work.
The combined signal is shown in figure 6.7, both for a scanning and a broadband ($\omega_l = 5.24\,\mathrm{kHz}$) experiment. A remarkable feature is that in the broadband case, the damping can lead to a higher signal. This can happen because ω_l is held fixed in the resonance function $\Lambda_1(\omega)$ and the damping term $\gamma_1\gamma_l$ comes with a minus sign, so it reduces the value in the denominator of 6.20. For the optimistic coupling, the broadband approach is a little more sensitive than the scanning approach at low frequencies. However, this is due to the fact that we overcouple and therefore have a larger accessible bandwidth at the readout, which also enhances some noise sources (see chapter 7 for further details).

7. Noise Sources

An important property of the heterodyne setup is the response to various noise sources. An investigation of the most important sources has already been done by the MAGO collaboration [2] and in [4]. Our treatment, however, is much more detailed. We start with a discussion of mechanical noise, which is supposed to be the strongest source since it couples to the same mechanical eigenfrequencies as the GW. Furthermore, two different kinds of thermal noise will be described as well as amplifier and oscillator phase noise. We will conclude with a discussion of other noise sources that are much less dominant and therefore negligible. This chapter greatly benefits from previous studies such as [3, 5, 43].
To compare our results with these studies, all noise sources are plotted with and without the damping term. In the non-damping case, we set $\gamma_1\gamma_l = 0$ in the resonance functions, such that the results are comparable with [4].
It is further argued in [4], that overcoupling is preferred in a broadband (i.e. broadband) search and we therefore assume $Q_{\mathrm{cpl}} = 10^5$, $Q_{\mathrm{int}} = 10^{10}$, while $Q_{\mathrm{cpl}} = Q_{\mathrm{int}} = 10^{10}$ in the scanning case. However, we have to be careful at lower frequency differences where the bandwidth of the signal mode might overlap with the pump mode. To avoid this, we adjust the coupling quality factor for each frequency step such that

$$Q_{\mathrm{cpl}}(\omega_g) = \max\left(10^5,\ \frac{2\omega_0}{\omega_g}\right).$$

This can lead to chaotic seeming curves for the broadband sensitivity in the lower frequency regime ($\lesssim 10\,\mathrm{kHz}$).

7.1. Mechanical Noise

Besides a passing GW, there are also several other mechanisms that can lead to an excitation of the mechanical cavity modes. The most dominant one is expected to come from external vibrations of the cryogenic cooling system [3], although attempts to isolate the cavity from this system were already made by the MAGO collaboration. So in the future, this influence could possibly be reduced such that it is lower than the unavoidable thermal noise. However, there are also seismic noise and thermal excitations that cannot be avoided completely. The latter is discussed in chapter 7.2 in more detail.
We can easily model the mechanical noise as an additional force density with a flat spectrum that couples to the mechanical modes via eqn. 6.11. The resulting PSD directly follows from eqn. 6.15 and reads

$$S_{\mathrm{mech}}(\omega) = \frac{\omega_1}{Q_{\mathrm{cpl}}} U_0 V_{\mathrm{cav}}^{-2/3} \frac{|C_{01}^l|^2}{M^2} \frac{\omega_1^4 S_{f_l}(\omega - \omega_0)}{|\Lambda_1(\omega - (\omega_0 + \omega_g))|^2}. \tag{7.1}$$

Note that we have to use $f_l(\omega) = F_l(\omega - \omega_g)$ and $q_l(t) = Q_l(\omega - \omega_g)$, since the mechanical noise has no specific frequency ω_g. For the function $S_{f_l}(\omega)$, we assume the same model as in [4, 43].

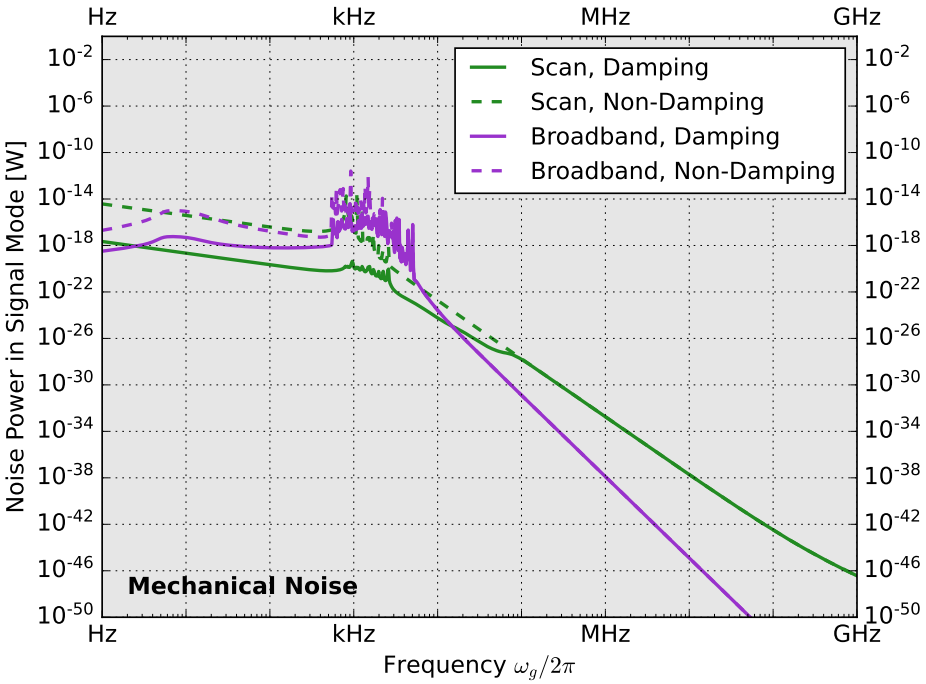

Figure 7.1.: *This is a plot of the total mechanical noise power. It is obtained by integrating eqn. 7.5 over the bandwidth of the signal mode. In the scanning case, we assume critical coupling by setting $Q_{cpl} = 10^{10}$, whereas we overcouple in the broadband case. The damping is assumed to be influenced by the lowest lying mode ($\omega_l = 50\,Hz$) only. To compare this plot to figure 3 from [4], note that we considering the additional sub-kHz modes of MAGO here which significantly change the shape of the curve. However, the orders of magnitude agree.*

According to a measurement from light-shining-through-wall experiments at FNAL [67, 68], it is possible to reduce the wall displacement of loaded cavities to $q_{\mathrm{rms}} \sim 0.1\,\mathrm{nm}$, where q_{rms} is the root mean square of $q(t)$. Setting $A_1(\omega) = 0$, we can derive the PSD

$$S_{q_l}(\omega) = \frac{1}{M^2} \frac{S_{f_l}(\omega)}{(\omega_l^2 - \omega^2)^2 + (\omega\omega_l/Q_l)^2}$$

from eqn. 6.11. For the Breit-Wigner shape, it is reasonable to impose the narrow-bandwidth approximation since $S_{f_l}(\omega)$ is spatially flat. From standard functional analysis, we know that

$$\frac{(\omega\omega_l/Q_l)^2}{(\omega_l^2 - \omega^2) + (\omega\omega_l/Q_l)^2} \longrightarrow \pi \frac{\omega_l}{Q_l} \delta\Big(\omega - \frac{\omega_l^2}{\omega}\Big) = \frac{\pi\omega_l}{2Q_l}\big(\delta(\omega - \omega_l) + \delta(\omega + \omega_l)\big) \tag{7.2}$$

so the time averaged displacement of mode l becomes

$$\langle q_l^2 \rangle = \frac{1}{(2\pi)^2} \int \mathrm{d}\omega S_{q_l}(\omega) = \frac{1}{4\pi M^2} \frac{Q_l}{\omega_l^3} S_{f_l}(\omega_l), \tag{7.3}$$

where we assumed $S_{f_l}(\omega_l) = S_{f_l}(-\omega_l)$. The squared wall displacement scales with $\langle q_l^2 \rangle \sim 1/\omega_l^3$, which means that the largest contribution comes from the lowest lying frequency. In [3], it is

therefore argued that $q_{\mathrm{rms}} = \sqrt{\langle q_{\mathrm{min}}^2(t)\rangle}$ where $q_{\mathrm{min}}(t)$ is the displacement of the lowest lying mode with frequency ω_{min}. We deduce that $S_{f_l}(\omega_{\mathrm{min}})$ becomes

$$S_{f_l}(\omega_{\mathrm{min}}) = 4\pi M^2 \omega_{\mathrm{min}}^3 \frac{q_{\mathrm{rms}}^2}{Q_l}. \tag{7.4}$$

Currently there are no available vibrational measurements for SRF cavities with cryogenic cooling systems for higher modes. In [4], it was argued that most mechanical noise sources decrease at least with $S_{f_l}(\omega) \sim 1/\omega$, so we assume $S_{f_l}(\omega) = S_{f_l}(\omega_{\mathrm{min}}) \times \omega_{\mathrm{min}}/\omega$. Plugging this into eqn. 7.1, we end up with

$$S_{\mathrm{mech}}(\omega) = \frac{\omega_1}{Q_{\mathrm{cpl}}} U_0 V_{\mathrm{cav}}^{-2/3} |C_{01}^l|^2 \frac{q_{\mathrm{rms}}^2}{Q_l} \frac{4\pi\omega_{\mathrm{min}}^3 \omega_1^4}{|\Lambda_1(\omega - (\omega_0 + \omega_g))|^2} \frac{\omega_{\mathrm{min}}}{\omega - \omega_0}, \qquad \omega - \omega_0 > \omega_{\mathrm{min}}. \tag{7.5}$$

Note that although the frequency ω_g appears in the resonance function, the noise is independent of the GW frequency. This can be found by explicitly calculating $\Lambda_1(\omega - (\omega_0 + \omega_g))$, which yields

$$\Lambda_1(\omega - (\omega_0 + \omega_g)) = \left(\omega_1^2 - \omega^2 + i\omega\frac{\omega_1}{Q_1}\right)\left(\omega_l^2 - (\omega - \omega_0)^2 + i(\omega - \omega_0)\frac{\omega_l}{Q_l}\right) - U_0 V_{\mathrm{cav}}^{-2/3} \omega_1^2 \frac{(C_{01}^l)^2}{M}.$$

Without the back-action term, this function agrees with the resonance structure of eqn. 17 in [4]. The integrated power of the thermal noise is shown in figure 7.1.

7.2. Thermal Noise

Thermal noise appears in two different channels: thermal vibration of the mechanical modes and thermal occupation of the electromagnetic modes. The former can be treated as an additional irreducible contribution to the mechanical noise. We follow [4] to derive the corresponding PSD. From 5.3, we can read off the Hamiltonian

$$H = \frac{1}{2} M \dot{q}_l^2 + \frac{1}{2} M \omega_l^2 q_l^2(t)$$

of one mechanical mode. It can be connected to the wall temperature via the equipartition theorem [4, 69]. We get

$$\left\langle q_l \frac{\partial H}{\partial q_l} \right\rangle = M\omega_l^2 \langle q_l^2(t)\rangle = k_{\mathrm{B}} T,$$

where k_{B} is the Boltzmann constant. Using 7.3, we can derive the thermal PSD

$$S_{f_{\mathrm{th}}}(\omega_l) = 4\pi M \frac{\omega_l}{Q_l} k_{\mathrm{B}} T.$$

It can be inserted into eqn. 7.1 in order to arrive at

$$S_{\mathrm{th}}^{(\mathrm{mech})}(\omega) = \frac{\omega_1}{Q_{\mathrm{cpl}}} U_0 V_{\mathrm{cav}}^{-2/3} \omega_1^4 \frac{|C_{01}^l|^2}{M} \frac{\omega_l}{Q_l} \frac{4\pi k_{\mathrm{B}} T}{|\Lambda_1(\omega - (\omega_0 + \omega_g))|^2}. \tag{7.6}$$

Unlike $S_{\mathrm{mech}}(\omega)$ in eqn. 7.5, the thermal noise can be reduced by increasing the cavity mass M. On the other hand, the thermal occupation of the electromagnetic modes can be modeled as an

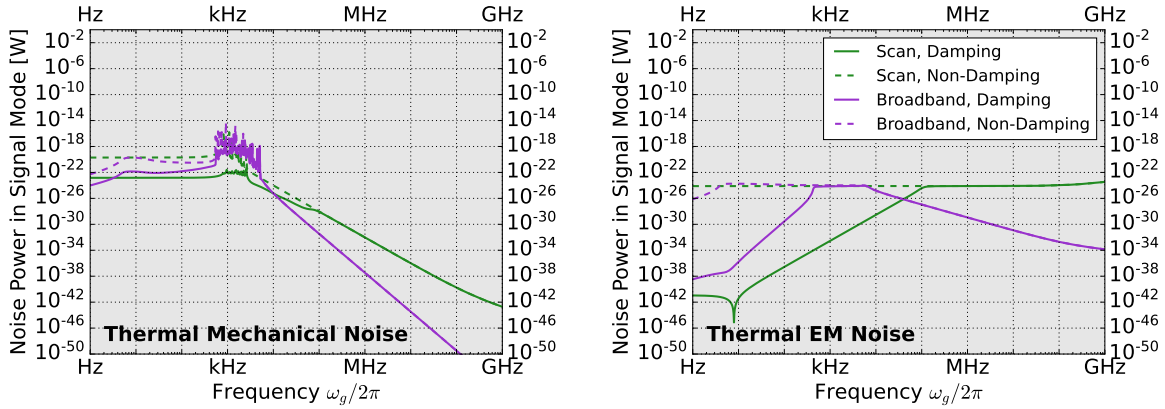

Figure 7.2.: *These plots show the total power of the thermal noise. On the left, the mechanical contribution is calculated by integrating eqn. 7.6 over the bandwidth of the signal mode. On the right, the electromagnetic contribution is shown by integrating over eqn. 7.8. In the scanning case, we assume critical coupling by setting $Q_{cpl} = 10^{10}$, whereas we overcouple in the broadband case. The damping of the thermal noise is assumed to be influenced by the lowest lying mode ($\omega_l = 50\,Hz$) only.*

additional external oscillator. We already know the PSD of such an oscillator from eqn. 6.21 and we can easily adapt it for the thermal noise such that

$$S_{\mathrm{th}}(\omega) = \frac{Q_1}{Q_{\mathrm{cpl}}}\frac{\omega_1^3}{Q_1^3}\frac{\omega^2 U_{\mathrm{th}} S_{b_{\mathrm{th}}}(\omega)}{|\Lambda_2(\omega-(\omega_0+\omega_g))|^2}. \tag{7.7}$$

The PSD $S_{\mathrm{th}}(\omega)$ of the thermal occupation can be derived similarly to $S_{f_l}(\omega_{\mathrm{min}})$ (eqn. 7.4). The idea is to attach a temperature T via the equipartition theorem to an unperturbed signal mode. That means, we consider eqn. 5.14 without the influence of a GW but with a thermal driving field, i.e.

$$\ddot{b}_1 + \frac{\omega_1}{Q_{\mathrm{int}}}\dot{b}_1 + \omega_1^2 b_1 = \frac{\omega_1}{Q_{\mathrm{int}}}\sqrt{\frac{U_{\mathrm{th}}}{U_1}}\dot{b}_{\mathrm{th}}$$

Fourier transformation and expressing the solution in terms of a PSD (using eqn. 6.19) yields

$$U_1 S_{b_1}(\omega) = \frac{1}{2}\frac{(\omega\omega_1/Q_{\mathrm{int}})^2}{(\omega^2-\omega_1^2)^2+(\omega\omega_1/Q_{\mathrm{int}})^2} U_{\mathrm{th}} S_{b_{\mathrm{th}}}(\omega).$$

The thermal spectrum is supposed to be flat compared to the Breit-Wigner resonance. By applying the narrow-bandwith approximation given in eqn. 7.2 again, we can calculate $\langle b_1^2(t)\rangle$ following the same arguments. The result can then be inserted into the equipartition theorem, using the Hamiltonion $H = U_1(e_1^2(t) + b_1^2(t))$ (compare with eqn. 5.5 or [5]). We find

$$\left\langle b_1 \frac{\partial H}{\partial b_1} \right\rangle = 2U_1\langle b_1^2\rangle = \frac{1}{4\pi}\frac{\omega_1}{Q_{\mathrm{int}}} U_{\mathrm{th}} S_{b_{\mathrm{th}}}(\omega) = k_{\mathrm{B}}T.$$

Together with eqn. 7.7, we finally obtain

$$S_{\mathrm{th}}(\omega) = \frac{Q_{\mathrm{int}}}{Q_{\mathrm{cpl}}}\frac{\omega_1^2}{Q_1^2}\frac{4\pi k_{\mathrm{B}} T\omega^2}{|\Lambda_2(\omega-(\omega_0+\omega_g))|^2}. \tag{7.8}$$

Note that the PSD agrees with the results from [3, 4] if we neglect the back-action (i.e. $\gamma_1\gamma_l = 0$). The integrated power of both types of thermal noise is shown in figure 7.2. An alternative way to derive the thermal noise PSD is described in appendix C.

7.3. Amplifier Noise

The amplifier noise is an irreducible noise source that arises at the readout of the system. Two main contributions are quantum zero-point fluctuations as well as back-action and imprecision noise associated with the amplifier [3]. As in [3, 4, 70], we assume that the noise can be reduced to its quantum limit, so we only have to consider the PSD

$$S_{\mathrm{amp}}(\omega) = 4\pi\hbar\omega.$$

This has been achieved for instance at GHz frequencies in [71]. Note that the spectral shape is only valid within the readout bandwidth. So the total power arising from the amplifier noise is the integral over the FWHM of the readout, i.e.

$$P_{\mathrm{amp}} = \int_{\omega_{\mathrm{cpl}}-\omega_{\mathrm{cpl}}/Q_{\mathrm{cpl}}}^{\omega_{\mathrm{cpl}}+\omega_{\mathrm{cpl}}/Q_{\mathrm{cpl}}} \mathrm{d}\omega\, 4\pi\hbar\omega = 8\pi\hbar\omega_{\mathrm{cpl}}\frac{\omega_{\mathrm{cpl}}}{Q_{\mathrm{cpl}}}. \tag{7.9}$$

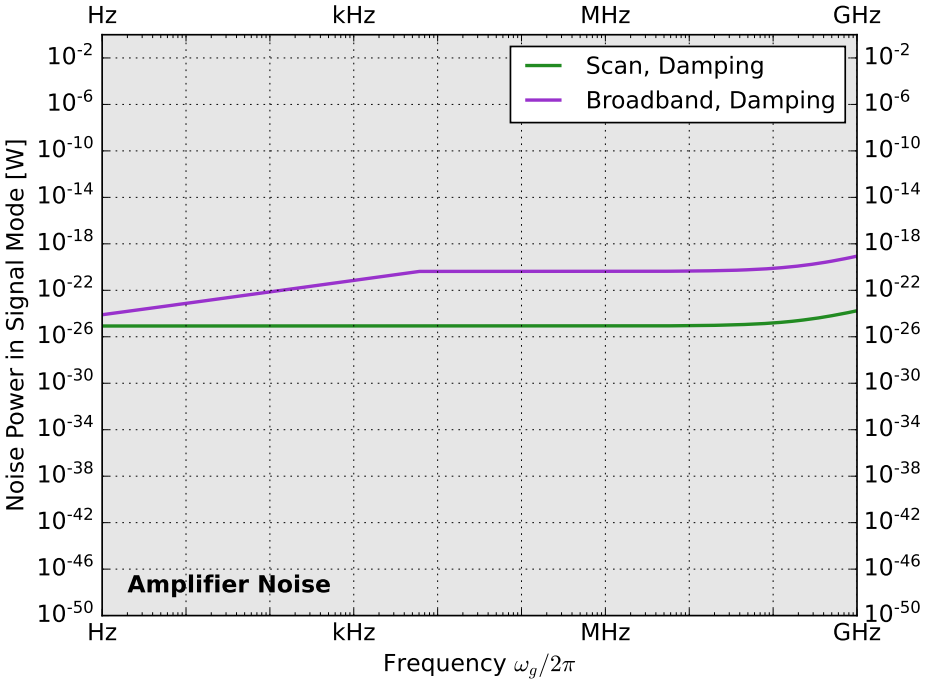

Figure 7.3.: *This plot shows the total power of the amplifier noise that is calculated in eqn. 7.9. In the scanning case, we assume critical coupling by setting $Q_{cpl} = 10^{10}$ whereas we overcouple in the broadband case. Note that $Q_{cpl} = 10^{10}$ is adjusted in case of overcoupling such that the pump and signal mode do not overlap. Therefore, the amplifer noise increases for the first $\sim 10\,kHz$. Since the noise appears in the readout system, it is the same for the damping and non-damping case.*

The power P_{amp} is shown in figure 7.3. In the broadband case, amplifier noise is the largest contribution to the total noise for high frequencies.

7.4. Oscillator Phase Noise

We have already discussed in detail the coupling of an external oscillator to the pump mode that has a small leakage to the signal mode in chapter 6. For a monochromatic oscillator, this leakage can be easily distinguished from the signal as there is no overlap in frequency space. However, the oscillator PSD might have a broad spectrum in general, which leads to a significant noise in the signal bandwidth.
We again follow the ansatz from [3, 43] and consider an oscillator with an additional phase $\varphi(t)$ such that

$$b_{\text{d}}(t) = e^{i\omega_0 t + i\varphi(t)} \approx e^{i\omega_0 t} + i\varphi(t)e^{i\omega_0 t},$$

where we assumed $\varphi(t) \ll 1$ in the last step. This function gives rise to the PSD

$$S_{b_{\text{d}}}(\omega) = 4\pi^2\delta(\omega - \omega_0) + S_\varphi(\omega - \omega_0).$$

The first term is again the monochromatic part of the input signal and can be neglected. We keep the second term which describes the power leakage to frequencies other than ω_0. Using

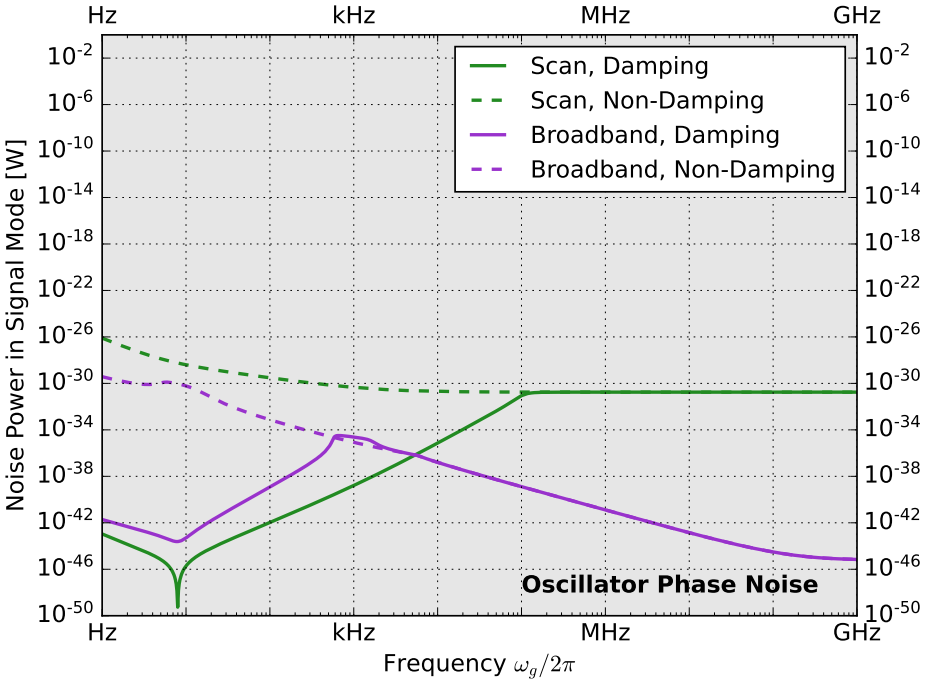

Figure 7.4.: *This plot shows the signal power of oscillator noise. It is obtained by integrating eqn. 7.10 over the bandwidth of the signal mode. In the scanning case, we assume critical coupling by setting $Q_{cpl} = 10^{10}$ whereas we overcouple in the broadband case. The damping is assumed to be influenced by the lowes lying mode ($\omega_l = 50\,Hz$) only. Note that the scanning, non-damping case agrees with the results from [3].*

eqn. 6.21, we obtain

$$S_{\mathrm{ph}}(\omega) = \epsilon^2 \frac{Q_1}{Q_{\mathrm{cpl}}} \frac{\omega_1^3}{Q_1^3} U_d \omega^2 \frac{S_\varphi(\omega - \omega_0)}{|\Lambda_2(\omega - (\omega_0 + \omega_g))|^2}. \tag{7.10}$$

The phase PSD can be approximated by a function of the form [3, 72]

$$S_\varphi(\omega) = \frac{1}{10^{15}\,\mathrm{Hz}} + \frac{1}{10^{11}} \frac{1}{\omega} + \frac{10^{-10}\,\mathrm{Hz}}{\omega^2} + \frac{10^{-8}\,\mathrm{Hz}^2}{\omega^3}.$$

It is a superposition of four distinguishable effects. The first term corresponds to white noise, while the $1/\omega$ component is due to flicker-noise[1]. Finally, the $1/\omega^2$ and $1/\omega^3$ contributions can be attached to the Leeson effect. It dominates for small frequency splittings between the pump and signal mode [3, 73, 74].
The strength of the oscillator phase noise can be controlled by the mode coupling ϵ. It was experimentally shown in [2, 40] for MAGO-like geometries, that couplings of $\epsilon \sim \mathcal{O}(10^{-7})$ can be achieved such that the PSD is suppressed by a factor of $\mathcal{O}(10^{-14})$. We will adopt this value for the rest of this thesis. The total power of the oscillator phase noise in the signal mode is shown in figure 7.4.

7.5. Other Noise Sources

In this chapter, we want to give a short discussion of other possible noise sources. For the MAGO-like design, they are suppressed compared to the noise discussed in the previous chapters. However, there could be alternative cavity designs where they play a role.
The first effect we consider here is called *Field Emission*. It arises from free electrons inside the cavity that are accelerated by high electric surface fields [3]. These electrons can come from imperfections in the cavity wall, which mostly appear at sharp edges or corners. Along their way through the cavity, the electrons emit energy in three different ways: Synchrotron radiation while they are accelerated, transition radiation when they hit the cavity wall and bremsstrahlung when they are decelerated inside the wall. A further discussion is given in [3], where it is argued that the Field Emission PSD at the signal mode ω_1 can be parametrized as

$$\frac{S_{\mathrm{fe}}(\omega_1)}{4\pi k_{\mathrm{B}} T} \approx \frac{P_{\mathrm{tot}}}{0.1\,\mathrm{W}} \times \begin{cases} 1 & \text{synchrotron radiation} \\ 10^{-6} & \text{transition radiation} \\ 10^{-5} & \text{bremsstrahlung.} \end{cases}$$

Here, P_{tot} is the total energy and $S_{\mathrm{fe}}(\omega_1)$ is compared to the thermal noise at temperature T. For $P_{\mathrm{tot}} \lesssim 0.1\,\mathrm{W}$, the noise from field emission is negligible. We note that modern cavity fabrication techniques can significantly reduce the total energy such that $P_{\mathrm{tot}} < 10\,\mathrm{W}$ up to surface fields of $\sim 60\,\mathrm{MV/m}$ [3]. In many cases, field emission is not even detectable at these field strengths [3, 75]. The shell of the MAGO cavity has a smooth geometry, even in the coupling system, so the noise is also negligible. However, if we should use retractable fins with sharp edges in order to tune the frequency difference between the pump and signal mode in the future, field emission could become relevant.
The next effect we want to discuss is a *Cavity Frequency Drift*. It occurs due to low frequency deformations from seismic noise or fluctuations of the wall temperature and largely depends on

[1] Sometimes also called 1/f noise or pink noise

the technical details of the cavity[2] [43]. The initial eigenmodes change such that the coupling and readout systems are not perfectly matched to the pump and signal mode. In [43], it was argued that the shift can be monitored with active feedback mechanisms and controlled with large precision in order to separate it from the signal. Hence, it is negligible compared to the other mechanical noise sources.
In [3], it is mentioned that nonlinearities in the response of the cavity walls to the pump mode fields could lead to radiation with frequencies corresponding to integer multiples of ω_0. This is, however, no problem for the heterodyne setup, as $\omega_1 - \omega_0 \ll \omega_0$ and we can therefore separate the noise from the signal mode.
There are a bunch of other effects that could be described here, for example multipacting and thermal breakdown [3, 76, 77]. However, they are well known today and can be controlled without having a considerable impact on the measurements. We therefore conclude that we only need to consider the noise sources mentioned in chapter 7.1-7.4.

7.6. The Total Noise

We can now combine all discussed noise sources to a total noise PSD given by

$$S_{\mathrm{tot}}(\omega) = S_{\mathrm{mech}}(\omega) + S_{\mathrm{th}}^{(\mathrm{mech})}(\omega) + S_{\mathrm{th}}(\omega) + S_{\mathrm{amp}}(\omega) + S_{\mathrm{ph}}(\omega)$$

and compute the sensitivity of the MAGO-like cavity. Before we do this in chapter 8, however, we want to compare the contributions of the different noises. Figure 7.5 shows the power of all noise sources for the broadband and scanning case respectively. It may be surprising that the noise in the broadband measurement is overall stronger, which seems to be different from the results in [4]. The reason is that we do not show the PSD but the total power in the signal

[2]For instance, it depends on the cavity's hysteresis.

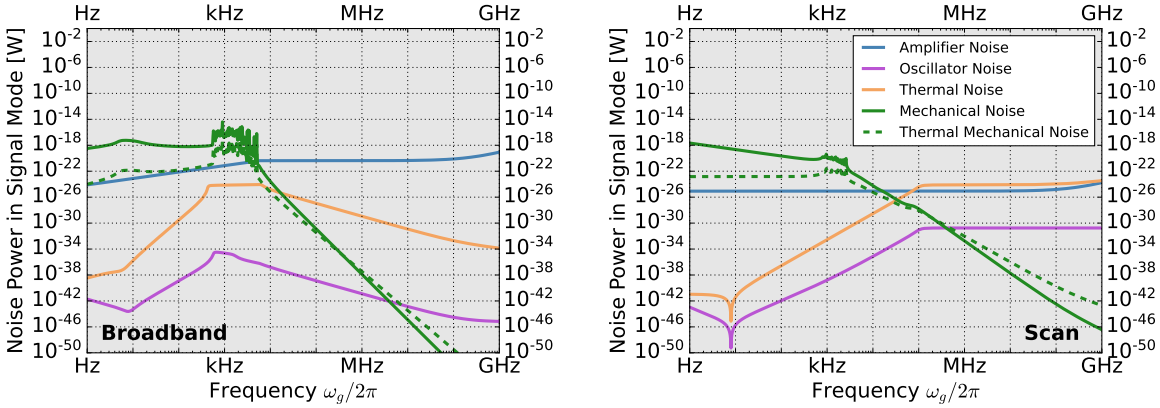

Figure 7.5.: *These plots show all contributions to the noise power. In the scanning case, we assume critical coupling by setting $Q_{cpl} = 10^{10}$ whereas we overcouple in the broadband case. We assume that the damping of the thermal and oscillator noise is only influenced by the lowest lying mode ($\omega_l = 50\,Hz$). We see that mechanical noise is the biggest contribution at low frequencies whereas thermal and amplifier noise dominate at high frequencies.*

mode, which depends on the coupling quality factor Q_{cpl}. As we pointed out at the beginning of this chapter, we overcouple in the broadband case ($Q_{\mathrm{cpl}} \sim 10^5$), which results in a much broader signal mode bandwidth. For $\omega_1 \sim 1\,\mathrm{GHz}$, the PSD has to be multiplied with a factor of $\omega_1/Q_{\mathrm{cpl}}(\omega) \sim 10\,\mathrm{kHz}$ to obtain the total power. For the scanning-case, where $Q_{\mathrm{cpl}} \sim 10^{10}$, the factor yields $\omega_1/Q_{\mathrm{cpl}} \sim 0.1\,\mathrm{Hz}$.
Besides the differences in the order of magnitude, figure 7.5 clearly shows the effect of damping for lower frequencies. The strongest effect can be seen for the thermal and oscillator phase noise, which drop by twelve orders of magnitude to below 100 kHz compared to the non-damping calculations (see also fig. 7.2 and fig. 7.4). The mechanical noise is influenced as well since the Breit-Wigner peaks of the resonances are much weaker than for the non-damping case.
When we consider the major noise contribution dependent on the frequency, we obtain the same result as in [4]. Both in the broadband and the scanning case, mechanical noise dominates up to $\sim 10\,\mathrm{kHz}$. For higher frequencies, amplifier noise dominates for the broadband setup and thermal EM noise for the scanning setup. Oscillator phase noise is negligible over the full parameter space since it is at least eight orders of magnitude below the leading contribution.
In future experiments, it may be possible that mechanical noise from the cryogenic system or seismic vibrations could be reduced below the thermal limit, which is represented by the dashed lines in figure 7.5. This would again significantly enhance the sensitivity at low frequencies. In our further analysis, we will include the optimistic assumption of a fully reduced noise in order to show the potential of future developments of the experiment.

8. Sensitivity Estimates

In this chapter, we finally want to compare the noise and signal powers to estimate the sensitivity of the MAGO cavity to GW signals. This has already been done in [4] for two ideal spheres with arbitrary coupling. We calculate the sensitivity by setting the signal-to-noise ratio to one, i.e.

$$\mathrm{SNR} = \frac{P_{\mathrm{sig}}}{P_{\mathrm{noise}}}\sqrt{\tau} = 1,$$

where τ is the integration time. By factorizing out the strain h_0 from the signal power, i.e. $P_{\mathrm{sig}} = h_0 \times P^h_{\mathrm{sig}}$, we obtain

$$h_{\mathrm{min}} = \frac{P_{\mathrm{noise}}}{P^h_{\mathrm{sig}}}\frac{1}{\sqrt{\tau}}.$$

We start with a discussion of the MAGO sensitivity in chapter 8.1 and subsequently compare the results to [4] in chapter 8.2.

8.1. MAGO Sensitivity

Once the MAGO prototype will arrive in Hamburg, we will start with basic measurements at room temperature ($T \approx 293\,\mathrm{K}$). The material properties of niobium (Young's modulus, Poisson ration etc.) are currently not available for the cooled cavity. Therefore, considering a damped signal with simulated coupling coefficients at room temperature is the most realistic setup.
However, it is clear that the quality factors will significantly shrink such that there is no chance to reach a physically interesting region. For that reason, we will, as in previous chapters, use the room temperature properties of niobium, but assume $T = 1.8\,\mathrm{K}$ as well as superconducting walls.
In figure 8.1, we show the results for a scanning and broadband ($\omega_l = 5.24\,\mathrm{kHz}$) experiment. Additionally, we include the sensitivity for the case that the mechanical noise can be reduced to the thermal limit (see chapter 7.2). It can be seen that the broadband approach is not sufficiently sensitive for GW detection. Even a scanning measurement can only reach strains beyond $h_0 \sim 10^{-20}$ in the MHz-regime. However, we note that this is just the sensitivity of a prototype with small couplings to the GW. An optimization of the couplings could considerably enhance the sensitivity in the future. The biggest advantage of an improved experimental setup would be that it could operate, at least, across 6 orders of magnitude in frequency space.[1] Furthermore, it has a small size and low costs.
In figure 8.2, we show the single contributions from the mechanical coupling and the Gertsenshtein effect. For the optimistic couplings, it shows the same behaviour that we already know from earlier results, namely that the latter is only dominant at very high frequencies in the GHz regime. We point out that the long wavelength approach breaks down for these short

[1] We saw that the Gertsenshtein effect becomes dominant above $\sim 100\,\mathrm{MHz}$, so the frequency range can be much larger. To further investigate this regime, the full metric of the proper detector frame must be taken into account.

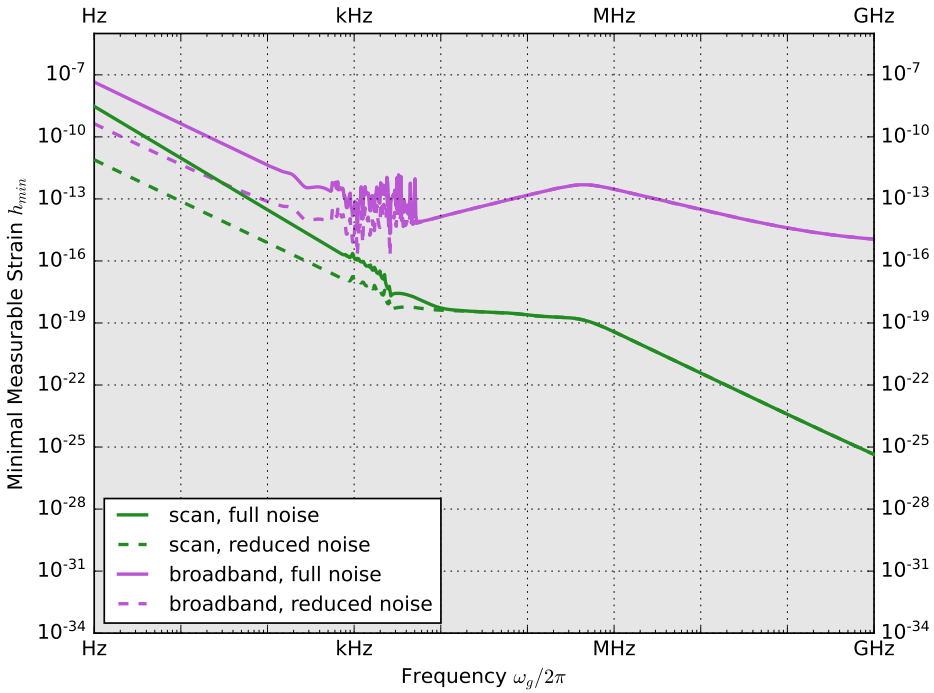

Figure 8.1.: *In this plot we show the sensitivity reach for the MAGO-like cavity at $T = 1.8\,K$ for different scenarios. First, we distinct between a scanning and broadband (non-scan, $\omega_l = 5.24\,kHz$) experiment. Second, we also show the case where mechanical noise can be reduced to the thermal limit (dashed lines). Note that the broadband approach is the most realistic case for the MAGO cavity, as a scan over a large frequency region is not feasible with the design (see chapter 2.3 and 2.5). It is, however, much less sensitive and does not reach the interesting region for new physics (see chapter 9). If we were able to include a scanning mechanism, the prospective reach would be about $\sim \mathcal{O}(10^{-22})$ above 10 MHz.*

wavelengths and more detailed calculations are required. However, when we consider the results for the simulated couplings, we see that the Gertsenshtein effect is already important at $\sim \mathcal{O}(1\,\mathrm{MHz})$, where our calculations are still valid.
Finally, we show the sensitivities for the case of a vanishing damping term in figure 8.3. The mechanical contribution is slightly stronger, but the result is still comparable to the case where the damping is included. We therefore conclude, that our improved calculations are important to better estimate the signal, but they do not significantly change the signal reach of the detector.
In each plot, we again show the case where the mechanical signal can be reduced below the thermal limit. We see that this would lead to some improvements at low frequencies, but it does not have a considerable impact to the sensitivity. Note that we used modern results to estimate the average shell displacement due to external vibrations (i.e. $q_{\mathrm{rms}} = 0.1\,\mathrm{nm}$). The original MAGO cavity could be much more vulnerable to these sources, which would further reduce the sensitivity.
Altogether, we see that the MAGO cavity is particularly suited to probe the frequency region above $\sim 10\,\mathrm{kHz}$, where GW could be only explained with new physics. In chapter 9, we will

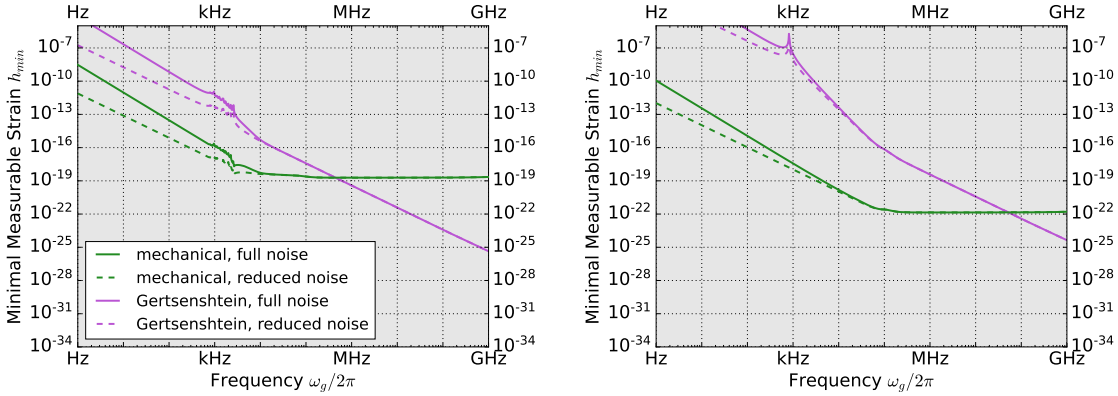

(a) *Simulated Values*
98 strongest couplings

(b) *Optimistic case*
$|C^l_{01}| = 1$, $|\Gamma_+| = |\Gamma_\times| = 0.5$.

Figure 8.2.: *These plots show the contributions from the mechanical coupling and the Gertsenshtein effect in case of a scanning setup. As we already showed in chapter 6.7, the Gertsenshtein effect is much weaker at low frequencies, where the mechanical coupling dominates. At high frequencies, however, the Gertsenshtein effect makes the largest contribution. (a): Calculation for the simulated values: Here, the mechanical coupling dominates below* $\sim 1\,MHz$. *(b): Optimistic case where we assumed a very high coupling (at* $\omega_l = 5\,kHz$*): The Gertsenshtein effect is much less dominant here and is only important above* $\sim 100\,MHz$. *However, we point out that we applied the long wavelength approach, which becomes less valid in this regime.*

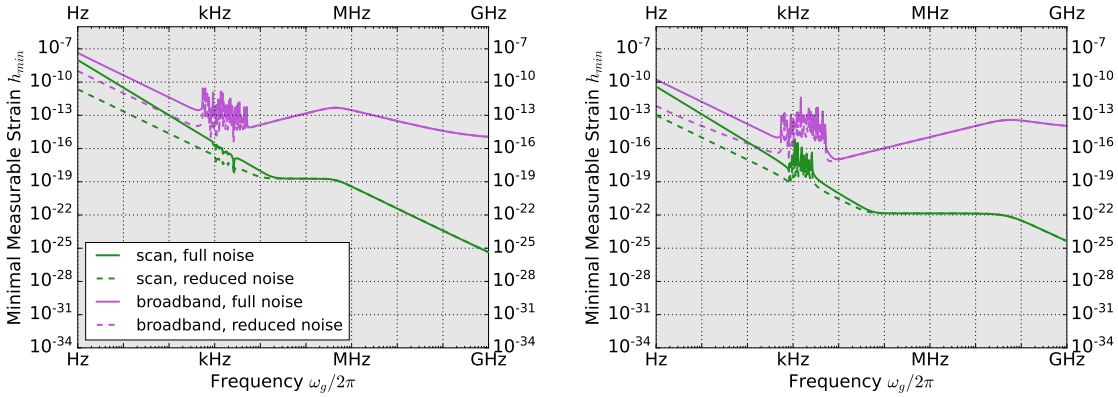

(a) *Simulated Values*
98 strongest couplings

(b) *Optimistic case*
$|C^l_{01}| = 1$, $|\Gamma_+| = |\Gamma_\times| = 0.5$.

Figure 8.3.: *In these plots we show the results without the damping term. (a): Sensitivity for the simulated value: This plot can be directly compared with figure 8.1. It shows that the damping term only has a small influence on the total sensitivity. (b): Sensitivity for the optimistic case (high coupling at* $\omega_l = 5\,kHz$*): This plot is comparable to figure 5 in [4]. The resonances of the mechanical noise are not damped and therefore have an effect on the sensitivity. We point out that the Gertsenshtein effect may be less dominant at high frequencies, since we imposed the long wavelength approach.*

discuss some possible sources that may produce GWs at these frequencies. The possible strain that can be reached is about $\sim \mathcal{O}(10^{-19})$ for the simulated values and $\sim \mathcal{O}(10^{-22})$ for the original values. The Gertsenshtein effect may even allow for lower strains above 100 MHz, but we postpone a detailed evaluation to future work.

8.2. Comparison to Previous Results

In this chapter we want to compare our results to Berlin et al. [4], since the same type of heterodyne cavity detectors is discussed in this paper. We already pointed out that [4] considers perfect spherical cavities with an arbitrary coupling, neglecting its influence on the mechanical properties. Furthermore, they did not consider the back-action effect which has, as we saw in the previous chapter, some influence on the results. In figure 8.4, we show the sensitivity estimates of [4]. They can be directly compared with our results in figure 8.5. We see that both look similar to each other, yet they disagree on some important aspects. For instance, the gap between the full mechanical and reduced mechanical noise is considerably smaller in our plot. The reason for this difference is in the mechanical eigenfrequencies. In [4], they were calculated for ideal spherical cavities with a total volume of $V_{\text{cav}} = 30\,\text{L}$ (our cavity has $V_{\text{cav}} \approx 9.6\,\text{L}$) and the influence of the central coupling was neglected. With our setup, we found a lowest lying mode of $\sim 0.05\,\text{kHz}$, which is much below the value of $\sim 10\,\text{kHz}$ assumed in [4]. So, because it is governed by the lowest lying mode, the mechanical noise is less dominant and close to the thermal limit. We discussed the underlying theory in chapter 7.1.
Furthermore, the Gertsenshtein effect is suppressed over the full frequency range in fig. 8.4,

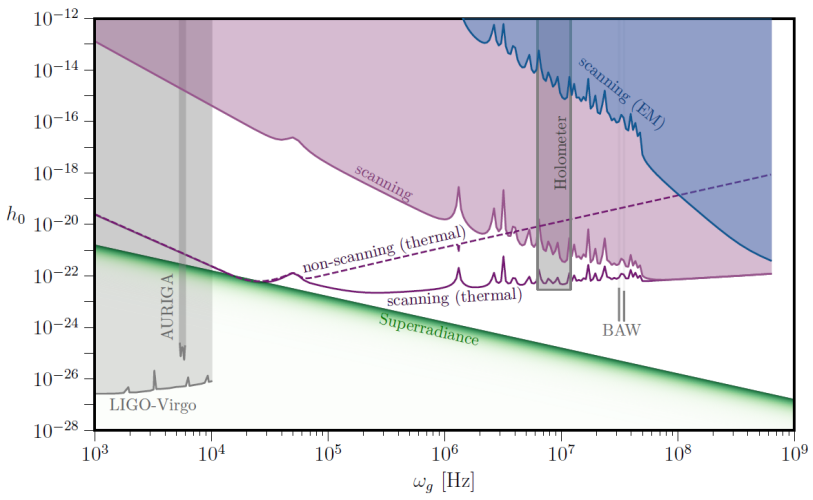

Figure 8.4.: *This plot is taken from [4] and shows the sensitivity reach of heterodyne cavities for scanning and broadband setups. The calculations were made for perfect spheres and an arbitrary coupling which was neglected for the mechanical modes. The sensitivities can be compared with figure 8.5, which shows the same plot with our results. Note that also the strain of possible black hole superradiance sources is shown here, which we will study in chapter 9. Also the frequency reach for some other GW experiments is shown. The label scanning (EM) refers to the Gertsenshtein coupling.*

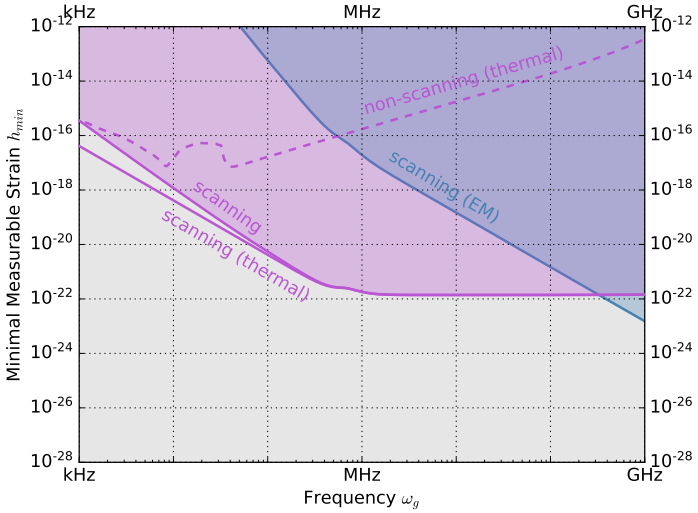

Figure 8.5.: *This plot shows the same sensitivities as in figure 8.4, but now for the MAGO-like cavity. We have chosen optimistic couplings, i.e.* $|C^l_{01}| = 1$, $\omega_l = 5\,kHz$ *and* $|\Gamma_+| = |\Gamma_\times| = 0.5$. *Both plots show comparable sensitivity reaches, although we included the damping from the back-action. However, there are some qualitative differences. The Gertsenshtein effect is much more important in our plot and the difference between mechanical and reduced mechanical scanning (i.e. only thermal vibrations included) is much less pronounced.*

whereas we find that it might dominate above $\sim 100\,\mathrm{MHz}$ even for optimistic couplings. It should be noted that the calculations for the Gertsenshtein coupling are more sophisticated in [4], because the full metric expansion of the proper detector frame is considered there. The result is therefore more accurate in the upper MHz-regime.
For the broadband estimates, [4] made a detailed optimization of the overcoupling. We have decided for a simpler approach by defining the bandwidth of the readout so that it does not overlap with the pump mode as long as it cannot be fixed s $Q_{\mathrm{cpl}} = 10^{-5}$ (more information can be found in chapter 7).
Another feature of figure 8.4 is that is shows the sensitivity regions of other important GW experiments such as LIGO/VIRGO, AURIGA (Weber bar experiment) and bulk-acoustic wave (BAW) resonators. Although they have a better sensitivity in a small region, the heterodyne approach is much more flexible and can probe several orders of magnitude in frequency space. We will see that it is sufficient to probe interesting regions of new physics, for instance black hole superradiance, in chapter 9.

9. Possible Sources

In this section, we want to give a short summary over possible sources of high frequency GW that could be detectable with SCRF cavities. We will focus on monocromatic sources, since a potential stochastic GW background is currently beyond the reach of the detector [4]. For more information on such a background, see e.g. [59, 78, 79].
The first part will be dedicated to primordial black holes and the second part to the more speculative idea of black hole superradiance. We then compare the expected strains with the experimental sensitivity.

9.1. Primordial Black Hole Mergers

In extensions of the ΛCDM-model, primordial black holes (PBH) may have formed within the first second after the big bang from the collapse of small scale density perturbations. A general pedagogical introduction can be found in [80]. Their mass could in principle range from $\sim \mathcal{O}(10^{-19})M_\odot$ to $\sim \mathcal{O}(10^4)M_\odot$, setting them apart from common black holes which always have more than several solar masses. A lower bound for the mass comes from Hawking radiation, because very light PBHs would have been evaporated since they were formed 13.8 billion years ago [81]. Also upper bounds could be made due to constraints on small scale perturbations from the freeze-out value of the proton-neutron ratio at the time of big bang nucleosynthesis [82]. However, higher masses are theoretically possible and were recently considered as potential explanations for the accelerated structure formation observed by the James Webb Space Telescope [83].
As they are hard to detect, PBHs could contribute a significant part of the dark matter content in the universe. Detailed bounds can be found in figure 1 of [81]. One remarkable insight of this plot is that in the mass range of $10^{-16} - 10^{-10}M_\odot$, PBHs could even explain all the dark matter. In this case, the mass of a PBH would be comparable to the mass of an asteroid with a size of a few kilometer.
If PBHs are large enough, they could be in principle detected by microlensing events during the transit of a background star. A recent analysis of data from the Optical Gravitational Lensing Experiment (OGLE) found six ultrashort timescale events that could only be explained by some earth mass objects [84]. As the origin of free floating planets is scarcely understood, it was argued in [85] that those events could instead come from PBHs. From the obeserved rate, an abundance of about $\sim 1\%$ of dark matter could be derived. This strongly motivates further searches for earth mass PBHs, for instance via GWs from merging events.
In order to detect PBH mergers, there must exist a mechanism for binary formation. There are two possible explanations: First, binaries could have been formed in the early universe when two PBHs were formed sufficiently close to each other [46, 86]. The other possibly mechanism could be tidal capture in dense environments [87, 88, 89]. It was argued in [81], however, that this late time production is subdominant for light PBHs.
The GW frequency originating from a PBH binary increases when the constituents approach.

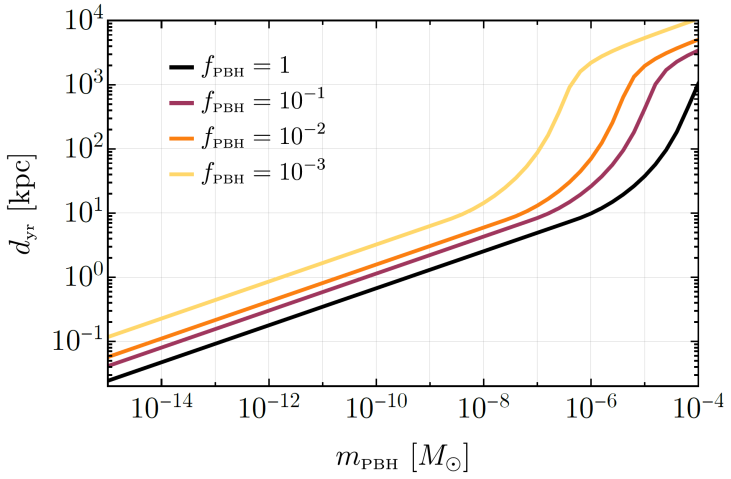

Figure 9.1.: *This plot is taken from [81] and shows the diameter of a sphere around the earth, where one merging event per year of a PBH binary with mass m_{PBH} can be expected. The merging rate also takes into account local density fluctuations from the milky way. Here, f_{PBH} denotes the relative abundance of PBHs relative to the case where they would describe the whole dark matter content in the universe. We assume the pessimistic case of $f_{PBH} = 10^{-3}$.*

A maximum is reached when the distance between them corresponds to the innermost stable circular orbit (ISCO). The GW frequency f_{ISCO} is then given by [81, 11, 46]

$$f_{\mathrm{ISCO}} = \frac{4400\,\mathrm{Hz}}{(m_1 + m_2)/M_\odot}.$$

We can also compute the characteristic GW strain during the inspiraling phase for an arbitrary frequency $f_{\mathrm{GW}} < f_{\mathrm{ISCO}}$. It is given by

$$h_0 \approx \frac{4}{D}\left(\frac{G\mathcal{M}}{c^2}\right)^{\frac{5}{3}}\left(\frac{\pi f_{\mathrm{GW}}}{c}\right)^{\frac{2}{3}},$$

where $\mathcal{M}$ is the chirp mass

$$\mathcal{M} := \left(\frac{(m_1 m_2)^3}{m_1 + m_2}\right)^{\frac{1}{5}}$$

and D the distance to the observer. For simplicity, we will assume $m_1 = m_2 =: m_{\mathrm{PBH}}$ in the following. We can then express h_0 as

$$h_0 \approx 9.77 \cdot 10^{-34} \times \left(\frac{f_{\mathrm{GW}}}{1\,\mathrm{GHz}}\right)^{\frac{2}{3}}\left(\frac{m_{\mathrm{PBH}}}{10^{-12} M_\odot}\right)^{\frac{5}{3}}\left(\frac{D}{1\,\mathrm{kpc}}\right)^{-1}. \tag{9.1}$$

However, the GW signal from an inspiraling PBH is not constant. We can express the coalescence time, i.e. the time until the f_{ISCO} is reached, as [11]

$$\tau(f) = 83\,\mathrm{sec} \times \left(\frac{m_{\mathrm{PBH}}}{10^{-12} M_\odot}\right)^{-\frac{5}{3}}\left(\frac{f}{\mathrm{GHz}}\right)^{-\frac{8}{3}}.$$

From this formula, it is straightforward to compute the time $\Delta\tau_{12} = \tau(f_1) - \tau(f_2)$ a binary emits GW in a certain frequency band between $f_1 > f_2$. This is important, since the heterodyne cavity has its highest sensitivity only for a small frequency band that corresponds to the difference between the pump and signal mode. A passing gravitational wave needs some time to pump the maximum energy into the signal mode, which is called the *ringup time*. It is defined as the inverse width of the Breit-Wigner curve, i.e. $\tau_{\mathrm{ru}} := 1/\Gamma_1 = 2\pi f_1/Q_1$. So for a given distance D and mass m_{PBH}, the maximum frequency and therefore also the maximum strain (eqn. 9.1) is constrained by

$$\tau\Big(f_1 + \frac{\Gamma_1}{2}\Big) - \tau\Big(f_1 - \frac{\Gamma_1}{2}\Big) > \tau_{\mathrm{ru}} = \frac{1}{\Gamma_1}$$

To estimate the characteristic distance $D(m_{\mathrm{PBH}})$ of a merging event, we need the merging rate, which is strongly dependent on the mass and abundance of the PBHs. More on that can be found in [81], where also the plot given in figure 9.1 is explained in more detail.

9.2. Black Hole Superradiance

We start with a very general setup where some particle is reflected by a potential barrier. Superradiance occurs when the amplitude of the outgoing state is higher then the amplitude of the initial state. This can only happen in the framework of relativistic quantum mechanics, for instance by applying the Klein-Gordon equation. In [90], it is argued that for a light scalar particle with charge e and frequency ω that is scattered at a potential barrier with strength V, the reflection amplitude R is related to the initial and transmitted amplitudes I and T via

$$|R|^2 = |I|^2 - \frac{\omega - eV}{\omega}|T|^2.$$

In this case, the superradiance condition (i.e. the condition to have $|R|^2 > |I|^2$), is given by

$$0 < \omega < eV.$$

The phenomenon can be understood in terms of quantum field theory. The high energy of the barrier can induce the spontaneous creation of particle-antiparticle pairs, which scatter with the incoming particle. Interestingly, this is not possible for fermionic particles, where a similar calculation leads to [90]

$$|R|^2 = |I|^2 - |T|^2.$$

This idea can be now applied to a spinning black hole with mass M_{BH} and spin $0 < |a_*| < 1$. Scalar particles can have bound states with the black hole that are comparable to the bound states in a hydrogen atom with quantum numbers n,l,m [91]. Therefore, the wavelength of the particle must be sufficiently large (several kilometers), so the mechanism is only possible for very light particles. The energy of a state with principal quantum number n is given by

$$\omega = m_p\left(1 - \frac{(r_g m_p)^2}{2n^2\hbar^2c^2}\right)$$

where m_p is the mass of the scalar particle and r_g the Schwarzschildt radius $r_g := 2GM/c^2$. Spinning black holes have an ergosphere, which is a region where the rotation of the black hole drags spacetime around it, i.e. no static observer is allowed [90]. If a particle enters the

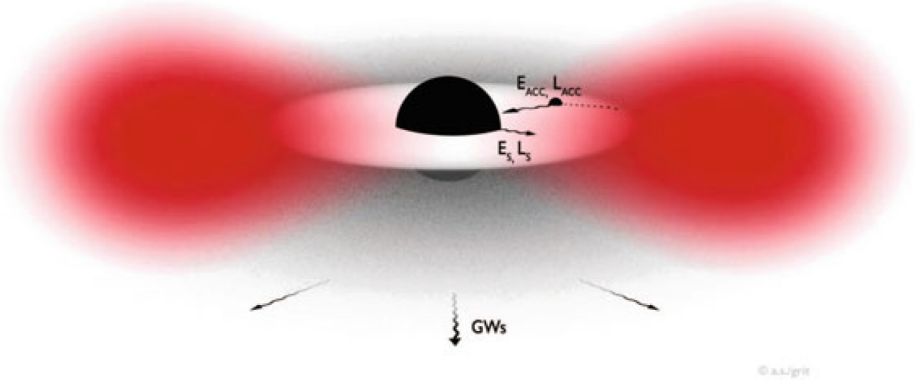

Figure 9.2.: *This plot is taken from [90] and shows the principle of superradiance. A light boson cloud builds up via superradiant instability of a rotating black hole and subsequently emits GW through annihilation and level transition. The emitted GW's are typically very coherent and could reach frequencies above* 1 *MHz, if the black hole is sufficiently light, i.e.* $M_{BH} \ll 1M_{\odot}$*. This is only possible for PBH's, so the mechanisms needs the existence of two speculative concepts.*

ergoregion, a direct interaction between the mass and the spacetime is possible via the Penrose process [92]. This interaction can be considered as a scattering at a barrier, with a superradiance condition that yields [91]

$$\frac{\omega}{m} < \omega^{+}, \tag{9.2}$$

where m is the magnetic quantum number and ω^{+} is defined by

$$\omega^{+} := \frac{1}{2}\left(\frac{a_*}{1+\sqrt{1-a_*^2}}\right)\frac{1}{r_g}.$$

The additional energy of the particle is taken from the black hole mass and angular momentum. When we now consider the scalar field in a bound state, it is constantly scattered in the ergoregion and thus reduces the angular momentum of the black hole. The energy is carried by the particles such that the occupation number of the bound state increases. This process is called *superradiant instability*, which continues until the superradiance condition (eqn. 9.2) is no longer satisfied. The maximum occupation number $N_{\max}$ only depends on the mass M_{BH} and the difference Δa_* between the initial and final spin. It is given by [91]

$$N_{\max} \approx 10^{76} \times \left(\frac{\Delta a_*}{0.1}\right)\left(\frac{M_{\mathrm{BH}}}{10M_{\odot}}\right)^2.$$

Note that the superradiant instability only requires a single spontaneous pair production in the vicinity of the black hole. It would therefore occur for each black hole with sufficiently large spin, if an appropriate light scalar field exists.
Such as a hydrogen atom can radiate photons, a bosonic cloud around a black hole emits GWs. This radiation can occur through three different channels: Level transition, annihilation of scalar particles or a collapse of the whole cloud due to the self interaction of the particles. The

latter appears when the energy transfer in the ergoregion becomes comparable to the binding energy of the field and is called *bosenova*. It leads to a short GW signals and the superradiant growth restarts [91]. We will focus here on the annihilation process, where the GW frequency is $\omega_g \approx 2m_p$. Signals from these processes are typically very coherent. A sketch of the full principle of GW production through black hole superradiance is given in figure 9.2.
The typical strain size for a black hole at distance D is given by [4, 93]

$$h_0 \approx 10^{-23} \times \left(\frac{\Delta a_*}{0.1}\right)\left(\frac{1\,\mathrm{kpc}}{D}\right)\left(\frac{M_{\mathrm{BH}}}{1\,M_\odot}\right)\left(\frac{\alpha}{0.2}\right)^7,$$

where the parameter α is defined through

$$\alpha := \frac{GM_{\mathrm{BH}}m_p}{\hbar c^3} \approx 0.2 \times \left(\frac{M_{\mathrm{BH}}}{1\,M_\odot}\right)\left(\frac{m_p}{3\times 10^{-11}\,\mathrm{eV}}\right). \tag{9.3}$$

We follow [4] and choose $D \gtrsim 1\,\mathrm{kpc}$ as well as $\alpha = 0.2$, such that $M_{\mathrm{BH}}(m_p) = M_{\mathrm{BH}}(\omega_g)$. According to [93], the superradiance condition can be rewritten as

$$\alpha \leq \frac{m}{2}\left(\frac{a_*}{1+\sqrt{1-a_*^2}}\right)$$

such that the minimum spin, where the superradiance disappears, becomes

$$a_*^{\min} = \frac{4m\alpha}{m^2+4\alpha^2}.$$

By choosing $a_*^{max} = 0.9$, we can then compute Δa_* for $l = m = 1$. The strain then simply follows from

$$h_0 \lesssim 10^{-23} \times \left(\frac{\omega_p}{91.1\,\mathrm{kHz}}\right)^{-1}\left(\frac{\Delta a_*}{0.1}\right). \tag{9.4}$$

Note that for high frequencies $\omega_g \gg 1\,\mathrm{MHz}$, the black hole mass must be $M_{BH} \ll 1M_\odot$. This is only possible for PBHs, so the superradiant emission of high frequency GW needs the existence of two speculative concepts. However, heterodyne cavity experiments would be particularly sensitive to these signals. To see this, consider the drift rate of the frequency, which can be calculated by [94]

$$\dot{\omega_g} \approx 7 \times 10^{-15}\frac{\mathrm{Hz}}{\mathrm{s}} \times \left(\frac{\alpha}{0.1}\right)^{17}\left(\frac{\omega_g}{1\,\mathrm{kHz}}\right).$$

For $\alpha = 0.1$, $\omega_0 = 1\,\mathrm{GHz}$ and $Q_1 = 10^5$, that means that the GW signal remains within the cavity bandwidth for $t \approx 10^5 a \times (\mathrm{MHz}/\omega_g)^2$ and is therefore very coherent [4] .

9.3. Comparison with Sensitivities

We can now compare the predicted sensitivities for PBHs and black hole superradiance with the sensitivity of MAGO. The result is shown in figure 9.3. We included the scanning sensitivity for the original as well as the optimistic couplings (i.e. $|C_{01}^l| = 1$, $\omega_l = 5\,\mathrm{kHz}$ and $|\Gamma_+| = |\Gamma_\times| = 0.5$). The PBH distances are taken from figure 9.1 and can be considered as upper bounds. A real signal may therefore be slightly stronger. Although the strains should be in principle measurable for some masses, the signal is to short to reach the ring-up time. Hence, MAGO is not able to

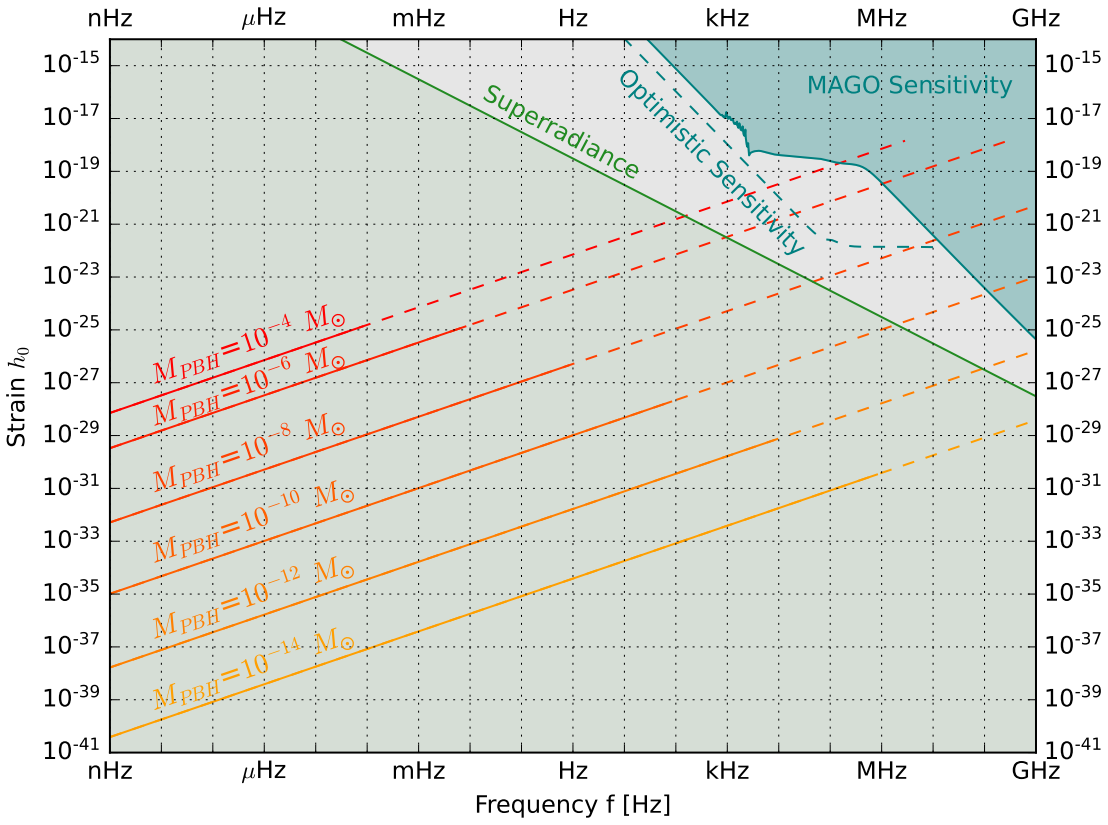

Figure 9.3.: *This plot shows the ability of MAGO to detect GW sources from new physics. Both the original sensitivity as well as the sensitivity for optimistic couplings ($|C^l_{01}| = 1$, $\omega_l = 5\,kHz$ and $|\Gamma_+| = |\Gamma_\times| = 0.5$) are included. We show two possible types of sources. The first are PBH mergers with six different masses from $10^{-4}\,M_\odot$ to $10^{-14}\,M_\odot$. The solid line shows the frequency and strain for a PBH merger with sufficiently large coherence time such that MAGO could in principle measure the signal. On the other hand, the strain rapidly grows before the merging event and would reach the detector sensitivity. However, the signal is too short to be resonantly amplified. The dashed line therefore shows the PBH strain when the frequency changes faster than the cavity ring-up time. When $f_{PBH} = f_{ISCO}$, the PBH merger has reached the ringdown and the signal suddenly stops. A better source would be superradiance, since it produces coherent and strong signals. The plot shows that the MAGO sensitivity (with optimistic couplings) only has to be improved by one order of magnitude to reach the interesting region.*

detect PBHs and they cannot be considered as promising candidates for the detector.
Superradiance, however, would produce very coherent strains with a sufficient strength that can be in principle detected. MAGO currently does not have enough sensitivity, but it only has to be optimized by one order of magnitude to reach the interesting region. We therefore conclude that MAGO has the ability to probe new physics and will be in particular able to confirm superradiance or exclude an important part of the parameter space.
In any case, if MAGO detects a signal, it would definitely come from a source that is not predicted by the standard model of particle physics and cosmology.

10. Conclusion

In this thesis, we investigated in detail how GWs interact with the electromagnetic field of a heterodyne cavity detector. We started with a detailed theoretical analysis of the interaction, where we focused on the special case of monochromatic GWs propagating in z-direction. The calculations were conducted in the proper detector frame, which is particularly important for the Gertsenshtein coupling, because it is not gauge invariant. We further used a particular type of cavity perturbation theory, which allowed us derive the mechanical couplings. The result was a formula for the supplied signal power in the signal mode induced by a GW, which reads

$$P_{\mathrm{sig}} = \frac{\omega_1}{Q_{\mathrm{cpl}}}\omega_g^4 U_0 \left| \frac{1}{2}\frac{V_{\mathrm{cav}}^{1/3}\gamma_1(h_+\Gamma_+ + h_\times\Gamma_\times)}{\beta_1\beta_l - \gamma_1\gamma_l} - \frac{\beta_l H(\kappa_1\eta_{01}^{\mathrm{E}} + \lambda_1\eta_{01}^{\mathrm{B}})}{\beta_1\beta_l - \gamma_1\gamma_l} \right|^2 .$$

This formula contains both the Gertsenshtein effect (coupling constants: η_{01}^{E}, η_{01}^{B}) as well as the mechanical coupling (coupling constants: C_{01}^l, Γ_+, $\Gamma_\times$), and shows that they can interfere both constructive and destructive. The parameters are given by

$$\begin{aligned}
\kappa_1 &= i\frac{\omega_1}{8c^2}(\omega_0 + \omega_g) \\
\lambda_1 &= \frac{\omega_1^2}{8c^2} \\
\beta_1 &= \omega_1^2 - (\omega_0 + \omega_g)^2 + i\frac{\omega_1}{Q_1}(\omega_0 + \omega_g) \\
\beta_l &= \omega_l^2 - \omega_g^2 + i\omega_g\frac{\omega_l}{Q_l} \\
\gamma_1 &= V_{\mathrm{cav}}^{-1/3}\omega_1^2 C_{01}^l \\
\gamma_l &= \frac{1}{M}V_{\mathrm{cav}}^{-1/3}U_0 C_{01}^l .
\end{aligned}$$

Unlike in Berlin et al. [4], we found a damping term $\gamma_1\gamma_l$ that significantly flattens the Breit-Wigner curve of the resonance, because it contains a factor $\omega_1^2 \sim \mathcal{O}(10^{18}\,\mathrm{Hz})$. We point out that this term is not new and was already considered by the MAGO collaboration [2, 5].
Although the damping reduces the total signal at frequencies below $\sim \mathcal{O}(1\,\mathrm{MHz})$, it does the same for the noise sources. Therefore, it does not dominantly effect the detector sensitivity and the conclusions of Berlin et al. [4] can be reproduced. Only some small scale effects like mechanical resonances are flattened due to the damping.
In addition to the theoretical analysis, we also applied our formalism to the original MAGO design. For simplicity, we used the material parameter for niobium at room temperature,[1] but assumed that the cavity is operated in a superconducting state which allowed to use the expected high quality factors. For the thermal noise, we have chosen a temperature of $T = 1.8\,\mathrm{K}$.
We provided a detailed investigation of the interaction by calculating over 800 coefficients for

[1] Since for a temperature of 2 K, not all values of the required parameters are known (see table 2.1).

the GW-mechanical and mechanical-EM coupling. They behave as expected, i.e. the GW-mechanical coupling decreases for higher resonances whereas the mechanical-EM coupling remains approximately at the same strength[2]. Furthermore, we could show that the mechanical modes that correspond to spherical eigenmodes start at $\sim 4\,\mathrm{kHz}$. At lower frequencies, we found a bunch of resonances that are related to the fully coupled system.
With these parameters, we were able to calculate the sensitivity. We considered both a scanning search and a broadband search, for which the frequency difference between the pump and signal mode is fixed. The latter is much less sensitive, but easier to realise since no tuning mechanism is needed.
In Berlin et al. [4], the lowest lying mode was assumed to be at $\sim 10\,\mathrm{kHz}$. However, we found that the lowest lying mode of the real cavity can be found at $\sim 0.05\,\mathrm{kHz}$, which resulted in a much weaker mechanical noise. For this noise, we made the same assumptions as in [3, 4]. Since the couplings turned out to be weaker than expected, we repeated the signal and sensitivity calculations with optimistic values $|C^l_{01}| = 1$, $\omega_l = 5\,\mathrm{kHz}$ and $|\Gamma_+| = |\Gamma_\times| = 0.5$.
Furthermore, we compared the results with expected strains from exotic objects beyond the standard model of particle physics and cosmology. In particular, we considered PBHs and black hole superradiance. It turned out that the latter might be within the reach of future optimized MAGO detectors, implying that they indeed potentially enable finding new physics. We did not consider a stochastic GW background, but MAGO detectors may also enable its detection in the future.
Once the MAGO cavity has arrived in Hamburg in Spring 2023, the first step will be to get familiar with the detector and to characterize the main parameters. This includes the mechanical and electromagnetic spectrum as well as the tunability and tuning mechanism. We did some preparations by simulating the spectrum of the MAGO cavity for a hammer blow at a fixed position and by considering the difference $\Delta\omega = \omega_1 - \omega_0$ between the pump and signal mode for slightly modified geometries. The results of these simulations can be compared to the real cavity in order to improve the model and subsequent simulations. An outlook and further ideas for future research on this experiment are laid out in chapter 11.

[2] Neglecting the two outliers at $\omega_l = 5.147\,\mathrm{kHz}$ and $\omega_l = 5.958\,\mathrm{kHz}$

11. Outlook

In this thesis, we provided a solid theoretical background for heterodyne GW experiments that we intend to become the foundation of future research. While working on this thesis, many interesting questions arose, which could become topics of future bachelor, master or even doctoral theses. Future students will benefit from a quickly growing research group at DESY/UHH and an improved knowledge of the MAGO prototype. In the following, we want to consider some possible open tasks for the theoretical part of the collaboration.

One of the most restrictive assumptions we adopt for this thesis was to consider only monochromatic GWs that propagate in z-direction. For future research, it is necessary to look at more general GWs that propagate along an arbitrary axis. Also the assumption of a monocromatic nature could be dropped and possible signals from a stochastic GW background could be investigated. Although it was argued in Berlin et al. [4] that such a background should be too weak to be detected with the first generation of heterodyne experiments, this must not be the case for future generations. The influence of the GW direction of propagation can be measured by the coupling coefficients. Two of those, the GW-mechanical as well as the GW-electromagnetic coupling, are sensitive to a change of direction. In Berlin et al. [4], such an analysis was already carried out for the GW-mechanical coupling and two ideal spheres. It could be repeated and applied to the MAGO design, and extended for GW couplings.

Furthermore, we have calculated the coupling constants for a static system configuration. In the original system, it was possible to change the cavity geometry, i.e. to deform the boundary conditions. Therefore, the coupling constants $\eta^{\mathrm{E}}_{01}(\gamma)$, $\eta^{\mathrm{B}}_{01}(\gamma)$, $\Gamma_{+}(\gamma)$, $\Gamma_{\times}(\gamma)$, $C^{l}_{01}(\gamma)$ are functions of an appropriate geometry parameter γ that describes the deformation of the initial configuration. This could be, for instance, the thickness or radius of the central tuning cell. A future analysis should include this dependence and investigate how the couplings change w.r.t. γ. The same issues have to be considered for the mechanical vibrations that are also assumed to remain unchanged so far.

At various points in this thesis, we mentioned that the simulation methods used might still be very inefficient and at some points inaccurate. With COMSOL, CST and Python, three different software and analysis tools were used to obtain the required results. To improve the speed of the analysis, it might be preferable to use only one tool. For instance, the electromagnetic eigenmodes could be also simulated with COMSOL and without using CST, which would avoid the cumbersome process of matching the coordinate grids. Furthermore, the resolution was chosen such that the calculation time and data size could be handled appropriately ($N_x \times N_y \times N_z = 30 \times 30 \times 90$ for MAGO). This caused some problems for higher order mechanical modes, as the typical scale at which the displacement field changes became smaller than the grid point distance. It was sufficient for this work as the primary focus was the theoretical background. However, a future analysis will require an improvement of the simulation methods.

In chapter 2.5, we showed that a breaking of the symmetry of the cavity geometry leads to much more flexibility concerning the scanning region. However, it is not clear if this is a feasible approach since the coupling constants rapidly decrease. Another problem is that additional

intermediate modes begin to appear between the symmetric and antisymmetric TE_{011} modes when the frequency difference is too large. This could lead to an energy leakage into modes with particularly high coupling to the pump mode. Therefore, an appropriate analysis of the cross-talk and all relevant mode couplings is required to appropriately estimate the total signal in the signal mode.
Also, alternative cavity geometries could be investigated, which should preserve the symmetry but allow for a larger scanning region. They could make use of different tuning mechanisms like retractable fins or movable parts inside the cavity[1]. However, the MAGO cavity is already the outcome of an optimization process [2] and it also has to be noted that the quality factor highly depends on the chosen geometry. So both the quality factor as well as the couplings have to be optimized simultaneously. Furthermore, alternative tuning mechanisms may cause additional noise sources. Retractable fins, for instance, add sharp features to the inner walls and could lead to enhanced field emission (see chapter 7.5 and [3]). These arguments are the reason why we only investigated variations of the original MAGO cavity. In future studies with focus on the cavity geometry, there would be more time to take all effects into account and hence to look at geometries different to the MAGO design.
One feature of the geometry that we ignored so far are the flanges that couple the oscillator and the readout to the cavity. In a perfect cavity design, they should be negligible. In figure 2.3, however, we see that they are very thick compared to the cavity and it is expected that they have a considerable influence on the mechanical modes. We therefore recommend to add them to the 3D model in future analysis to improve match of experiment and simulation. In particular, if the flange is located at an antinode of a mechanical excitation, it could change the whole mode and lead to different solutions than shown in this thesis.
Finally, we point out that one cavity might not be able to cover the full frequency range from

[1]This approach was already chosen for instance in axion searches like ADMX [29].

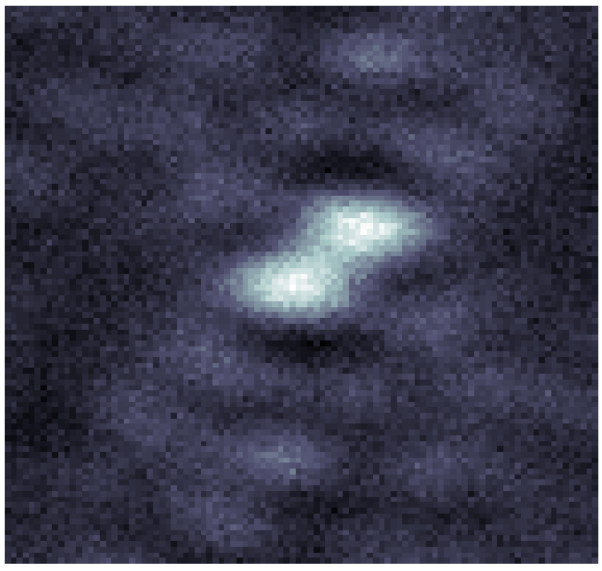

Figure 11.1.: *This picture is taken from [2] and shows the possible resolution of a network of ten MAGO cavities. The two sources have an angular separation of* $\Delta\theta = \Delta\phi = 0.1$. *The whole picture covers one square degree of the sky.*

1 kHz to 1 GHz. Further, it would be not possible to locate the origin of the GW on the sky, as we only measure the coupling strength which can in general not unambiguously be attached to a certain direction. A solution would be to use multiple cavities, in best case at different places on the earth to additionally filter unwanted noise sources. An intelligent configuration would both allow for a localisation of the GW source and an enhanced sensitivity. We also point out that a search focused on a potential stochastic GW background requires at least two cavities that have to be cross-correlated [2]. Alternatively, one could use a MAGO cavity in conjunction with other experiments like Weber bar detectors or interferometers.
Adding more MAGO cavities could enhance the resolution of the detector and therefore allow for making pictures of the sky in the GW band. In [2], it is pointed out that this would also enhance the sensitivity about N times, where N is the number of cavities. Figure 11.1 shows a possible picture of two close GW sources on the sky taken by an array of $N = 10$ MAGO cavities. If these sources have a separation of $\Delta\theta = \Delta\phi \sim 0.1°$, this configuration would already be able to separate them. A further investigation of the possibilities offered by MAGO arrays is urgently needed as the low costs of a single detector allow to use them in the foreseeable future.
We conclude that there are many opportunities for future research not only at the experimental level. However, it is important to point out that we need experimental data from the first MAGO run in order to match the simulations with the real cavity. Since the measurements will be conducted at room temperature, we will still be forced to extrapolate towards low temperatures ($T \approx 1.8\,\mathrm{K}$), which will, however, be sufficient to confirm the models. For instance, the comparison allows for an investigation of whether the flanges have an important influence on the mechanical modes or not. With the acquired experience, we can then start to address the questions mentioned above. The cavity will arrive shortly after this thesis is finished, so this project will directly continue.

12. Acknowledgements

Last but not least, I would like to thank all the people who helped me during my time as a master student. First, I want to thank my supervisor Gudrid Moorgat-Pick, who gave this exciting topic to me that will hopefully lead to further fruitful research within the Quantum Universe Cluster of Excellence. She thus gave me the opportunity to experience the development of a small research collaboration from the very beginning. Furthermore, she extensively supported my ambitions to continue my studies abroad, which now will be possible at the University of Geneva. In this regard, I also want to thank Jochen Liske, who supported me in this as well.
I am very thankful to Krisztian Peters, Marc Wenskat and Andreas Ringwald for many helpful discussions and Fabian Balzer for his numerous comments on the first draft of this thesis. To my parents, I owe dept of gratitude for their emotional and financial support through all the ups and downs of the last years. I am grateful to my love Insa, who helped me through the stressful finale phase of this work. You came when I needed you most and never left my side.

A. Basic Tools from Elasticity Theory

In this chapter, we want to review the basic tools from elasticity theory, that allow us to find an equation of motion for a driven isotropic elastic solid. A more comprehensive treatment can be found in standard textbooks such as [52] or [53].

A.1. The General Formalism

Consider a point $\vec{x}$ in an unstressed, continuous solid body. Applying a force $\vec{F}$ leads to a deformation, which results in a translation of a mass at point $\vec{x}$ to a new position $\vec{x'}$ given by

$$\vec{x} \longrightarrow \vec{x'} = \vec{x} + \vec{u}(\vec{x}),$$

where $\vec{u}(\vec{x})$ is called the *displacement vector*.
To describe a deformation, we must consider the change of the displacement vector from one location to another. This change can be quantified by a second rank tensor defined as the gradient of the displacement vector

$$W_{ij} = \partial_j u_i.$$

We can decompose this tensor into its irreducible parts, i.e.

$$\begin{aligned} W_{ij} &= \frac{1}{3}\delta_{ij}W_{kk} + \frac{1}{2}(W_{ij} + W_{ji}) - \frac{1}{3}\delta_{ij}W_{kk} + \frac{1}{2}(W_{ij} - W_{ji}) \\ &=: \frac{1}{3}\delta_{ij}\theta + \Sigma_{ij} + R_{ij}, \end{aligned}$$

where

$$\begin{aligned} \theta &:= W_{kk} = \mathrm{Tr}(W) && \text{(Expansion)} \\ \Sigma_{ij} &:= \frac{1}{2}(W_{ij} - W_{ji}) - \frac{1}{3}\delta_{ij}W_{kk} && \text{(Shear)} \\ R_{ij} &:= \frac{1}{2}(W_{ij} - W_{ji}) && \text{(Rotation).} \end{aligned}$$

Each of these tensors describes a certain type of deformation. To understand why the trace θ, for instance, describes an expansion, consider a small volume element V of a solid body. After a deformation $\vec{x} \longrightarrow \vec{x'} = \vec{x} + \vec{u}(\vec{x})$, the surface vector $\mathrm{d}\vec{S}$ is displaced by the vector $\vec{u}(\vec{x})$. During that process, it sweeps out a volume $\mathrm{d}\vec{S} \cdot \vec{u}$ [53]. The full volume change can be obtained by integrating over the surface ∂V of V, i.e.

$$\delta V = \int_{\partial V} \mathrm{d}\vec{S} \cdot \vec{u} = \int_V \mathrm{d}V \nabla\vec{u} = \nabla\vec{u} \int_V \mathrm{d}V = \nabla\vec{u} \cdot V = \theta V.$$

In the third equality, we used that V is considered as a small volume, so $\nabla\vec{u}$ is approximately constant. We observe that the trace of W describes the fractional change of the volume since

$$\theta = \frac{\delta V}{V}.$$

In contrast, the shear tensor Σ_{ij} is traceless and therefore describes a deformation without volume change. Clearly, due to the principle axis theorem, it is always possible to find a coordinate system in which the shear tensor is diagonal. In this system, it describes a stretch or a squeeze along each direction, but the net volume change sums up to zero. This is what is called shear.
Finally, we want to understand the rotation tensor. Therefore, consider a rotation

$$\vec{u} = \vec{\omega} \times \vec{x} \qquad \Leftrightarrow \qquad \vec{\omega} = \frac{1}{2}\nabla \times \vec{u},$$

which can be rewritten as

$$\omega_i = \frac{1}{2}(\nabla \times \vec{u})_i = \frac{1}{2}\epsilon_{ijk}\frac{1}{2}(\partial_j u_k - \partial_k u_j) = -\frac{1}{2}\epsilon_{ijk}R_{jk}.$$

Thus, the rotation is described by the antisymmetric part R_{ij}.
In most cases, the rotation is not relevant in elasticity theory since it does not produce any internal forces inside the solid body. Therefore, it is often neglected and only the so-called strain tensor

$$S_{ij} = W_{ij} - R_{ij} = \frac{1}{3}\delta_{ij}\theta + \Sigma_{ij} = \frac{1}{2}(W_{ij} + W_{ji})$$

is considered. It has nothing to do with the GW strain $h_{\mu\nu}$, although there are some conceptional similarities.
Now that we have a tensor describing the displacement, we need a tensor describing its origin. This so-called stress tensor can be constructed by considering two small regions in a solid body which are in contact with each other. The first region exerts a force $\mathrm{d}\vec{F}$ on the second one through a contact surface with surface vector $\mathrm{d}\vec{S}$. Doubling the area $\mathrm{d}\vec{S}$ naturally doubles the force. Thus, there must be a linear relationship between $\mathrm{d}\vec{S}$ and $\mathrm{d}\vec{F}$. The transformation matrix is given by the fully symmetric stress-tensor

$$\mathrm{d}F_i = T_{ij}\mathrm{d}S_j.$$

Here, we use the convention of [53], whereas [52] defines T_{ij} with the opposite sign.
If the stress is determined by local conditions only, we can compute the total force by integrating

$$F_i = -\int_{\partial V} T_{ij}\mathrm{d}S_j = -\int_{\partial V} \vec{T}_i \mathrm{d}\vec{S} = -\int_V \nabla\vec{T}_i \mathrm{d}V = -\int_V (\partial_j T_{ij})\mathrm{d}V =: \int_V f_i \mathrm{d}V.$$

The force density can be therefore defined as

$$f_i = -\partial_j T_{ij}. \tag{A.1}$$

Since the stress tensor is symmetric, we can decompose it into a trace and a symmetric, traceless part

$$T_{ij} = \frac{1}{3}\delta_{ij}T_{kk} + \frac{1}{2}(T_{ij} + T_{ji}) - \frac{1}{3}\delta_{ij}T_{kk} =: \delta_{ij}P + T^s_{ij}$$

with

$$P = \frac{1}{3}T_{kk} \qquad \text{(Pressure)}$$

$$T^s_{ij} = \frac{1}{2}(T_{ij} + T_{ji}) - \frac{1}{3}\delta_{ij}T_{kk} \qquad \text{(Shear Stress)}.$$

In elasticity theory, one assumes a linear relationship between the stress and the strain tensor also on a non-infinitesimal level. Such a relation is governed by the fourth-rank elastic modulus tensor

$$T_{ij} = -Y_{ijkl} S_{kl}.$$

Since T_{ij} and S_{ij} are symmetric, Y_{ijkl} inherits the following symmetries

$$\begin{aligned} Y_{ijkl} &= Y_{jikl} = Y_{ijlk} \\ Y_{ijkl} &= Y_{klij}. \end{aligned}$$

For an isotropic medium, we assume that

$$\begin{aligned} P &\propto \theta \\ T^s_{ij} &\propto \Sigma_{ij}. \end{aligned}$$

In that case, the relation between S_{ij} and T_{ij} reduces to

$$T_{ij} = \delta_{ij} P + T^s_{ij} = -Y_{ijkl} S_{kl} = -K\theta\delta_{ij} - 2\mu\Sigma_{ij}$$

with the bulk modulus K and the shear modulus (or second Lamé coefficient) μ. Both constants are material dependent and fulfill $K, \mu > 0$.
This relation can be brought into a more useful form, using $S_{ij} = \frac{1}{3}\delta_{ij}\theta + \sigma_{ij}$ such that

$$T_{ij} = -(K - \frac{2}{3}\mu)\theta\delta_{ij} - 2\mu S_{ij} =: -\lambda\theta\delta_{ij} - 2\mu S_{ij} \tag{A.2}$$

with the first Lamé coefficient

$$\lambda = K - \frac{2}{3}\mu.$$

We now have all the tools to calculate $\vec{u}$.

A.2. Elastodynamics

Now, we want to consider a time-dependent force inducing elastodynamic waves in the medium. According to Newton's second law, a non-vanishing force density results in a time-dependent deformation

$$\vec{F} = \frac{\partial \vec{p}}{\partial t} = \frac{\partial (m\vec{v})}{\partial t} \qquad \Rightarrow \qquad \vec{f} = \frac{\partial (\rho\vec{v})}{\partial t} = \frac{\partial}{\partial t}\Big(\rho \frac{\partial \vec{u}}{\partial t}\Big).$$

The force density can be calculated using eqn. A.1 together with eqn. A.2. We obtain

$$f_i = -\partial_j(-\lambda\theta\delta_{ij} - 2\mu S_{ij}) = (\lambda + \mu)\partial_i(\nabla\vec{u}) + \mu\Delta u_i.$$

Thus, the equation of motion becomes

$$\frac{\partial}{\partial t}\Big(\rho \frac{\partial \vec{u}}{\partial t}\Big) = (\lambda + \mu)\nabla(\nabla\vec{u}) + \mu\Delta\vec{u}.$$

Note that ρ is time-dependent as well! To derive a linear wave equation, we decompose

$$\rho = \rho(\vec{x}) + \delta\rho(\vec{x}, t)$$

and assume:

- $\delta\rho$, $\vec{u}$ and $\frac{\partial\vec{u}}{\partial t}$ are small, we only need to expand up to first order in these quantities.
- $\rho(\vec{x})$ varies on much larger scales than $\vec{u}$ or $\frac{\partial\vec{u}}{\partial t}$ and can be therefore treated as constant.

These statements allow us to write

$$\frac{\partial}{\partial t}\Big(\rho\frac{\partial\vec{u}}{\partial t}\Big) = \frac{\partial}{\partial t}\Big(\rho(\vec{x})\frac{\partial\vec{u}}{\partial t} + \delta\rho(\vec{x},t)\frac{\partial\vec{u}}{\partial t}\Big) = \rho(\vec{x})\frac{\partial\vec{u}}{\partial t}$$

which leads to the wave equation

$$\rho(\vec{x})\frac{\partial\vec{u}}{\partial t} - (\lambda+\mu)\nabla(\nabla\vec{u}) - \mu\Delta\vec{u} = 0.$$

Note that $\rho(\vec{x})$ describes the density of the unperturbed solid only.
Finally, it is useful for us to assume that the elastodynamic wave is driven by an external force density (i.e. the gravitational wave). If we denote this external force with $\vec{f}$, the final version of the equation of motion yields

$$\rho(\vec{x})\frac{\partial\vec{u}}{\partial t} - (\lambda+\mu)\nabla(\nabla\vec{u}) - \mu\Delta\vec{u} = \vec{f}(\vec{x},t).$$

B. Further Calculations for Cavity Eigenmodes

In this chapter, we provide further calculations for the properties of general cavity eigenmodes. We start with a proof of the statement, that it is possible to find a space of eigensolutions such that $\vec{E}_n$ and $\vec{B}_n$ are either solenoidal or irrotational. After that, we show that it is not possible to resonantly enhance the irrotational modes. It is therefore sufficient to consider solenoidal modes only in a cavity experiment.

B.1. Solenoidal and Irrotational Modes

The goal of this chapter is to show that the eigensolutions $\vec{E}_n$ and $\vec{B}_n$ of the BVP

$$\begin{aligned} \Delta\vec{E}_n(\vec{x}) + k_n^2\vec{E}_n(\vec{x}) &= 0 & \nabla\cdot\vec{E}_n|_S &= 0 & \vec{n}\times\vec{E}_n|_S &= 0 \\ \Delta\vec{B}_n(\vec{x}) + k_n^2\vec{B}_n(\vec{x}) &= 0 & \vec{n}\cdot\vec{B}_n|_S &= 0 & \vec{n}\times(\nabla\times\vec{B}_n)|_S &= 0. \end{aligned}$$

can be written in terms of solenoidal and irrotational modes only. They are defined through

$$\left.\begin{aligned} \Delta\vec{E}_n^s + k_n^{E,s}\vec{E}_n^s &= 0 & \nabla\cdot\vec{E}_n^s &= 0 \\ \Delta\vec{B}_n^s + k_n^{B,s}\vec{B}_n^s &= 0 & \nabla\cdot\vec{B}_n^s &= 0 \end{aligned}\right\} \quad \text{solenoidal modes} \tag{B.1}$$

$$\left.\begin{aligned} \Delta\vec{E}_n^r + k_n^{E,r}\vec{E}_n^r &= 0 & \nabla\times\vec{E}_n^r &= 0 \\ \Delta\vec{B}_n^r + k_n^{B,r}\vec{B}_n^s &= 0 & \nabla\times\vec{B}_n^r &= 0 \end{aligned}\right\} \quad \text{irrotational modes.} \tag{B.2}$$

We want to proof this statement for a cavity with a single connected and closed surface, following again [48].
From the fundamental theorem of vector calculus[1], we know that each continuous and differentiable vector field in a closed region is uniquely determined by its vortices and sources inside that region as well as its normal and tangential components on the shell. This means, we can decompose the eigensolutions $\vec{E}_n$ and $\vec{B}_n$ of the Helmholtz equation as

$$\begin{aligned} \vec{E}_n &= \vec{E}_n^s + \vec{E}_n^r & \nabla\cdot\vec{E}_n^s &= 0 & \nabla\times\vec{E}_n^r &= 0 \\ \vec{B}_n &= \vec{B}_n^s + \vec{B}_n^r & \nabla\cdot\vec{B}_n^s &= 0 & \nabla\times\vec{B}_n^r &= 0. \end{aligned} \tag{B.3}$$

The remaining task now is to show that $\vec{E}_n^s$,$\vec{B}_n^s$ and $\vec{E}_n^r$,$\vec{B}_n^r$ are eigensolutions as well. Combining the decomposition with eqn. B.1, we find

$$\begin{aligned} \nabla\cdot\vec{E}_n &= \nabla\cdot\vec{E}_n^r & \nabla\times\vec{E}_n^r &= 0 & \vec{n}\times\vec{E}_n^r|_S &= 0 \\ \nabla\times\vec{E}_n &= \nabla\times\vec{E}_n^s & \nabla\cdot\vec{E}_n^s &= 0 & \vec{n}\times\vec{E}_n^s|_S &= 0 \\ \nabla\cdot\vec{B}_n &= \nabla\cdot\vec{B}_n^r & \nabla\times\vec{B}_n^r &= 0 & \vec{n}\cdot\vec{B}_n^r|_S &= 0 \\ \nabla\times\vec{B}_n &= \nabla\times\vec{B}_n^s & \nabla\cdot\vec{B}_n^s &= 0 & \vec{n}\cdot\vec{B}_n^s|_S &= 0. \end{aligned} \tag{B.4}$$

[1] also known as Helmholtz theorem

Since $\vec{E}_n$ and $\vec{B}_n$ are eigensolutions of the Helmholtz equation, we can write

$$\Delta\vec{E}_n + k_n^2\vec{E}_n = \Delta\vec{E}_n^r + k_n^2\vec{E}_n^r + \Delta\vec{E}_n^s + k_n^2\vec{E}_n^s = 0$$

and similarly for the B-field. For the solenoidal and irrotational modes, we therefore find

$$\begin{aligned} \Delta\vec{E}_n^r + k_n^2\vec{E}_n^r &= \vec{C}_\mathrm{E} & \qquad \Delta\vec{E}_n^s + k_n^2\vec{E}_n^s &= -\vec{C}_\mathrm{E} \\ \Delta\vec{B}_n^r + k_n^2\vec{B}_n^r &= \vec{C}_\mathrm{B} & \qquad \Delta\vec{B}_n^s + k_n^2\vec{B}_n^s &= -\vec{C}_\mathrm{B} \end{aligned}$$

where $\vec{C}_\mathrm{E}$ and $\vec{C}_\mathrm{B}$ are some vector fields. We can use fundamental identities for the nabla operator and the properties of solenoidal and irrotational modes (eqn. B.3) to write

$$\begin{aligned} \nabla\cdot(\nabla\cdot\vec{E}_n^r) + k_n^2\vec{E}_n^r &= \vec{C}_\mathrm{E} \\ -\nabla\times(\nabla\times\vec{B}_n^s) + k_n^2\vec{B}_n^r &= -\vec{C}_\mathrm{B}. \end{aligned}$$

Evaluating these equations on the shell gives

$$k_n^2\vec{E}_n^r|_S = \vec{C}_\mathrm{E}|_S \qquad\qquad k_n^2\vec{B}_n^r|_S = -\vec{C}_\mathrm{B}|_S.$$

Using equation B.4, we can formulate two boundary value problems which fully determine $\vec{C}_\mathrm{E}$ and $\vec{C}_\mathrm{B}$. They have the form

$$\begin{aligned} \nabla\cdot\vec{C}_\mathrm{E} &= 0 & \qquad \nabla\times\vec{C}_\mathrm{E} &= 0 & \qquad \vec{n}\times\vec{C}_\mathrm{E}|_S &= 0 \\ \nabla\cdot\vec{C}_\mathrm{B} &= 0 & \qquad \nabla\times\vec{C}_\mathrm{B} &= 0 & \qquad \vec{n}\cdot\vec{C}_\mathrm{B}|_S &= 0. \end{aligned}$$

According to the Helmholtz theorem, this uniquely determines $\vec{C}_\mathrm{E}$ and $\vec{C}_\mathrm{B}$ to vanish inside the cavity, i.e. $\vec{C}_\mathrm{E} = \vec{C}_\mathrm{B} = 0$. This means that $\vec{E}_n^s$,$\vec{B}_n^s$ and $\vec{E}_n^r$,$\vec{B}_n^r$ are indeed eigensolutions to the Helmholtz equation as well, so the proof is completed. Furthermore, we also see that

$$k_n^{E,r} = k_n^{E,s} = k_n^{B,r} = k_n^{B,s} =: k_n.$$

So we see that an arbitrary field fulfilling the boundary conditions given in eqn. 3.6 can be expanded in terms of solenoidal and irrotational modes.

B.2. Resonance Behaviour of Irrotational Modes

Consider the inhomogeneous Maxwell equations (eqn. 3.1 and 3.4). We assume that the current $\vec{J}$ decomposes into an effective current $\vec{J}_\mathrm{eff}$ driven by an external source and a term obeying Ohms law, which reads

$$\vec{J} = \vec{J}_\mathrm{eff} + \sigma\vec{E}.$$

This is an appropriate choice for general cavity experiments, where the material dependent conductivity σ is induced by power losses in the cavity walls and can be treated as a scalar here. We follow [31] and make a rotation of Faraday's law (eqn. 3.3) to obtain the wave equation

$$\nabla\times(\nabla\times\vec{E}) + \frac{1}{c^2}\frac{\partial^2\vec{E}}{\partial t^2} + \sigma\frac{\partial\vec{E}}{\partial t} = -\frac{\partial\vec{J}_\mathrm{eff}}{\partial t}. \tag{B.5}$$

Since solenoidal and irrotational modes provide a complete basis, we can decompose $\vec{E}$ and use that $\nabla \times (\nabla \times \vec{E}_{\mathrm{rn}}(\vec{x})) = 0$ as well as

$$\nabla \times (\nabla \times \vec{E}_{\mathrm{sn}}) = -\Delta \vec{E}_{\mathrm{sn}}(\vec{x}) + \nabla \cdot (\nabla \cdot \vec{E}_{\mathrm{rn}})(\vec{x}) = -\Delta \vec{E}_{\mathrm{sn}}(\vec{x}) = \frac{\omega_{\mathrm{sn}^2}}{c^2} \vec{E}_{\mathrm{sn}}(\vec{x}),$$

where we used the Helmholtz equation 3.9 in the last step. Inserting this into equation B.5 yields

$$\sum_n \Big[\frac{\omega_{\mathrm{sn}}^2}{c^2} e_{\mathrm{sn}}(t) \vec{E}_{\mathrm{sn}}(\vec{x}) + \frac{1}{c^2} \frac{\partial^2}{\partial t^2} \big(e_{\mathrm{sn}}(t) \vec{E}_{\mathrm{sn}}(\vec{x}) + e_{\mathrm{rn}}(t) \vec{E}_{\mathrm{rn}}(\vec{x}) \big) + \frac{\partial}{\partial t} \big(\sigma_{\mathrm{sn}} e_{\mathrm{sn}}(t) \vec{E}_{\mathrm{sn}}(\vec{x}) + \sigma_{\mathrm{rn}} e_{\mathrm{rn}}(t) \vec{E}_{\mathrm{rn}}(\vec{x}) \big) \Big] = -\frac{\partial \vec{J}_{\mathrm{eff}}}{\partial t}. \tag{B.6}$$

Here, we assumed a different conductivities σ_{sn} and σ_{rn} for each mode. To investigate the behaviour of solenoidal and irrotational modes, we use the orthogonality condition. Starting with the solenoidal modes, we integrate over $\vec{E}_{\mathrm{sm}}$ to get

$$\frac{\omega_{\mathrm{sm}}}{c^2} e_{\mathrm{sm}}(t) \int_{V_{\mathrm{cav}}} \mathrm{d}^3x \vec{E}_{\mathrm{sm}}^2 + \frac{1}{c^2} \frac{\partial^2 e_{\mathrm{sm}}(t)}{\partial t^2} \int_{V_{\mathrm{cav}}} \mathrm{d}^3x \vec{E}_{\mathrm{sm}}^2 + \sigma_{\mathrm{sm}} \frac{\partial e_{\mathrm{sm}}(t)}{\partial t} \int_{V_{\mathrm{cav}}} \mathrm{d}^3x \vec{E}_{\mathrm{sm}}^2 = -\int_{V_{\mathrm{cav}}} \mathrm{d}^3x \vec{E}_{\mathrm{sm}} \frac{\partial \vec{J}_{\mathrm{eff}}}{\partial t}.$$

Assuming a monochromatic source, i.e. $\vec{J}_{\mathrm{eff}}(\vec{x}, t) = \vec{J}_{\mathrm{eff}}(\vec{x}) \cos(\omega_g t)$, this equation can be brought into the form

$$\frac{1}{c^2} \frac{\partial^2 e_{\mathrm{sm}}(t)}{\partial t^2} + \sigma \frac{\partial e_{\mathrm{sm}}(t)}{\partial t} + \frac{\omega_{\mathrm{sm}}^2}{c^2} e_{\mathrm{sm}}(t) = \alpha_{\mathrm{sm}} \omega_g \sin(\omega_g t),$$

where we have introduced the abbreviation

$$\alpha_i := \frac{\int_{V_{\mathrm{cav}}} \mathrm{d}^3x \vec{E}_i(\vec{x}) \vec{J}_{\mathrm{eff}}(\vec{x})}{\int_{V_{\mathrm{cav}}} \mathrm{d}^3x \vec{E}_i^2(\vec{x})}.$$

The inhomogeneous second-order differential equation can be solved with standard methods. For $e_{\mathrm{sm}}(t)$, we find

$$e_{\mathrm{sm}}(t) = \frac{\alpha_{\mathrm{sm}} c^4 \omega_g}{(\omega_g^4 + \omega_{\mathrm{sm}}^4) - 2\omega_{\mathrm{sm}}^2 \omega_g^2 + c^4 \sigma_{\mathrm{sm}}^2 \omega_g^2} \Big(\sigma \omega_g \sin(\omega_g t) - \frac{\omega_{\mathrm{sm}}^2 - \omega_g^2}{c^2} \cos(\omega_g t) \Big) + \cdots,$$

where we omitted further decaying terms dependent on the boundary conditions. It is immediately clear that there is a resonance at $\omega_{\mathrm{sm}} = \omega_g$, so it is possible to resonantly enhance solenoidal modes. On the other hand, when we integrate equation B.6 over $\vec{E}_{\mathrm{rm}}$ to analyze the irrotational modes, we get

$$\frac{1}{c^2} \frac{\partial^2 e_{\mathrm{rm}}(t)}{\partial t^2} + \sigma_{\mathrm{rm}} \frac{\partial e_{\mathrm{rm}}(t)}{\partial t} = \alpha_{\mathrm{rm}} \omega_g \sin(\omega_g t)$$

for a monochromatic source $\vec{J}_{\mathrm{eff}}(\vec{x}, t) = \vec{J}_{\mathrm{eff}}(\vec{x}) \cos(\omega_g t)$. The solution is given by

$$e_{\mathrm{rm}}(t) = -\frac{\alpha_{\mathrm{rm}} c^4}{\omega_g^2 + \sigma^2 c^4} \Big(\frac{\omega_g}{c^2} \sin(\omega_g t) + \sigma_{\mathrm{rm}} \cos(\omega_g t) \Big) + \cdots,$$

where we again omitted decaying terms depending on the boundary conditions. There is clearly no resonance appearing here, so we come to the conclusion that irrotational modes cannot be resonantly enhanced [31]. Thus, we will neglect these modes when we calculate the cavity signal of a certain gravitational wave event and only consider the solenoidal ones. The advantage is that we can therefore always assume $\nabla \cdot \vec{E}_n = 0$.

C. RLC Circuits and Thermal Noise

This chapter gives a short introduction to the correspondence between RLC circuits and cavities. The results are then used to derive the thermal noise PSD $S_{b_{\mathrm{th}}}(\omega)$ that has been used in chapter 7.2. More details can be found in standard textbooks on electrodynamics such as [49, 95].

C.1. RLC Circuits and Cavities

Consider a typical parallel RLC circuit with resistance R, inductance L and conductivity C (see fig. C.1). The circuit obeys Kirchhoff's voltage law, i.e.

$$u_d = u_R + u_C + u_L = RI + \frac{q}{C} + L\dot{I}$$

with current $I = \dot{q}$. We can perform the derivative on both sides and introduce the effective voltage $u := u_R = RI$ to get

$$\ddot{u} + \frac{R}{L}\dot{u} + \frac{1}{LC}u = \frac{R}{L}\dot{u}_d. \tag{C.1}$$

The solution for this differential equation in case of a damped oscillation (i.e. $R^2 < 4L/C$) is given by $u(t) = u_0 e^{\alpha t} e^{-i\omega t}$ with constants

$$\alpha := \frac{R}{2L} \qquad \omega := \sqrt{\frac{1}{LC} - \frac{R^2}{4L^2}}.$$

One can immediately see that $\omega = \sqrt{1/(LC)}$ in case of a free harmonic oscillator ($R = 0$). It is further possible to introduce a quality factor $Q := 1/R\sqrt{L/C}$ such that eqn. C.1 can be written

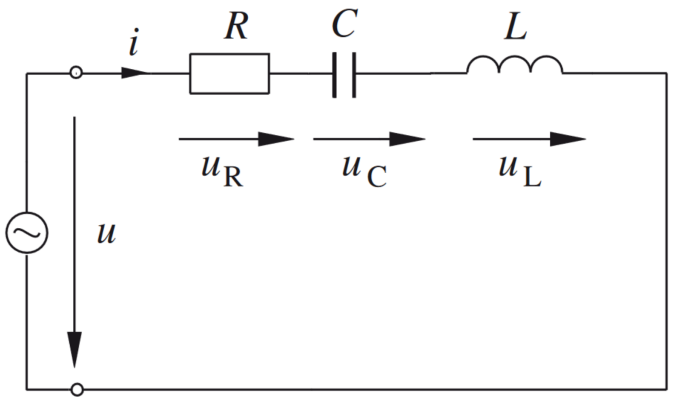

Figure C.1.: *Sketch of a typical parallel RLC circuit with resistance R, inductance L and conductivity C. The figure is taken from [96].*

as

$$\ddot{u}_n + \frac{\omega_n}{Q_n}\dot{u}_n + \omega_n^2 u_n = \frac{\omega_n}{Q_n}\dot{u}_d,$$

where we have introduced an index n referring to the different modes. This is the driven RLC version of eqn. 3.23. If we compare the power signals of both the RLC circuit and the cavity (eqn. 3.30), we get

$$P_{\text{sig}} = \frac{\langle u_n^2(t)\rangle}{R_n} = \frac{1}{(2\pi)^2}\frac{\omega_n}{Q_n}\frac{1}{R_n}\int \mathrm{d}\omega S_{u_n}(\omega) = \frac{1}{2\pi^2}\frac{\omega_n}{Q_n}U_n\int \mathrm{d}\omega S_{b_n}(\omega).$$

This formula gives us a correspondence between a RLC circuit and a cavity. We can compute the signal PSD in one system and then translate the solution into the other system by applying

$$U_n S_{b_n}(\omega) = \frac{S_{u_n}(\omega)}{R_n}. \tag{C.2}$$

This is particularly helpful for the calculation of the thermal noise, which we will perform in the following chapter.

C.2. The Thermal Noise PSD

We follow [43] and describe the thermal noise as an external oscillator that drives additional energy into the signal mode. Thus, it can be modelled in the RLC picture as

$$\ddot{u} + \frac{R_1}{L_1}\dot{u} + \frac{1}{L_1 C_1}u = \frac{R_1}{L_1}\dot{u}_{\text{th}}. \tag{C.3}$$

It is convenient to perform a Fourier transformation of this equation and to write the solution as

$$u(\omega) = \left[i\omega\frac{\omega_1}{Q_1} - (\omega^2 - \omega_1^2)\right]^{-1} i\frac{\omega\omega_1}{Q_1}u_{\text{th}}(\omega),$$

where we have written the coefficients again in terms of the mode-frequency ω_1 and the quality factor Q_1. We can then make a narrow-width approximation, i.e. the Breit-Wigner resonance can be treated as a delta-peak because $\omega_1/Q_1 \ll 1$. Applying standard techniques from functional analysis gives

$$\frac{(\omega\omega_1/Q_1)^2}{(\omega\omega_1/Q_1)^2 + (\omega^2 - \omega_1^2)^2} \longrightarrow \pi\frac{\omega_1}{Q_1}\delta(\omega - \omega_1^2/\omega) = \frac{\pi\omega_1}{2Q_1}\big(\delta(\omega - \omega_1) + \delta(\omega + \omega_1)\big).$$

For the thermal noise, we will need the time average $\langle u^2(t)\rangle$. With eqn. 3.25, we get

$$\langle u^2(t)\rangle = \frac{1}{4\pi}\frac{\omega_1}{2Q_1}\big(S_{u_{\text{th}}}(\omega_1) + S_{u_{\text{th}}}(\omega_1)\big) = \frac{\omega_1}{4\pi Q_1}S_{u_{\text{th}}}(\omega),$$

since the spectrum of the thermal noise is assumed to be flat and therefore $S_{u_{\text{th}}}(-\omega_1) = S_{u_{\text{th}}}(\omega_1)$. The temperature T can be now connected to the average energy via the equipartition theorem [43, 69]. We note that the full Hamiltonian of the system can be written as

$$H = \frac{1}{2}L_1 I^2 + \frac{1}{2}C_1 u^2.$$

It is then straightforward to calculate

$$k_{\mathrm{B}}T = \left\langle I_1 \frac{\partial H}{\partial I_1} \right\rangle = L_1 \langle I^2(t) \rangle = \frac{L_1}{R_1^2} \langle u^2(t) \rangle = \frac{1}{R_1} \frac{Q_1}{\omega_1} \langle u^2(t) \rangle,$$

where k_{B} is the Boltzmann constant. With equation C.2, it follows the final expression for the thermal noise in the cavity. The result is

$$U_{\mathrm{th}} S_{b_{\mathrm{th}}}(\omega) = \frac{S_{u_{\mathrm{th}}}(\omega)}{R_1} = 4\pi k_{\mathrm{B}} T.$$

D. Axions

In [3] and [43], it was argued that heterodyne cavity experiments can be used for Axion research as well. So the question arises how strong such a signal would be in the MAGO cavity, although it is not actively optimized for these signals.
We start with a short discussion of the theoretical background. Axions are light scalar particles that were initially introduced to solve the strong CP-problem in quantum chromodynamics. The problem arises due to an additional so-called θ-term in the Lagrangian, which violates the invariance under CP-transformation. It reads

$$\mathcal{L}_{\mathrm{QCD}} = \bar{\psi}(i\gamma^\mu \partial_\mu - m)\psi - g_s \bar{\psi}(\gamma^\mu T^a G^a_\mu)\psi - \frac{1}{4} G^a_{\mu\nu} G^{a\mu\nu} + \underbrace{\bar{\theta} \frac{g_s^2}{32\pi^2} G^{\mu\nu}_a \tilde{G}^a_{\mu\nu}}_{\theta\text{-Term}}.$$

Until today, no CP-violation was measured and the upper experimental bound is $\theta \lesssim 10^{-10}$ [97]. From naturalness arguments, one would therefore expect that there must be a mechanism suppressing the θ-term and preserving the CP-symmetry. In 1977, R. D. Peccei and H. Quinn introduced a new global chiral $U(1)$ symmetry, which is spontaneously broken at some (large) energy scale f_a [98]. It leads to a new scalar field a in the Lagrangian such that we get

$$\mathcal{L}_{\mathrm{QCD}} = \mathcal{L}_{\mathrm{SM}} - \frac{1}{2}\partial_\mu a \partial^\mu a + \mathcal{L}_{\mathrm{int}}\left[\frac{\partial^\mu}{f_a}\right] + \left(\bar{\theta} + \xi \frac{a}{f_a}\right) \frac{g_s^2}{32\pi^2} G^{\mu\nu}_a \tilde{G}^a_{\mu\nu}.$$

It turns out that the scalar field effectively cancels the θ-term. This approach is commonly known as *Peccei-Quinn mechanism*. An improved mechanism was developed one year later by S. Weinberg and F. Wilczek [99, 100]. They identified the scalar field with a new light pseudo Nambu-Goldstone boson, which was dubbed *Axion* by F. Wilczek.
Apparently, the original Axion does only couple to quarks. However, there are two reasons why it is reasonable to search for Axion-photon couplings. The first is that since the introduction of the Peccei-Quinn mechanisms, many new light particles with similar properties were predicted which are commonly called Axion-like particles. They are related, for instance, to String Theory, where they are embedded in the so-called *String Axiverse* [101]. Some of these particles can in principle couple to the photon.
But already the original Axion (sometimes called QCD Axion) can couple to the photon via higher order loops (which is known as the Primakoff effect [102]). It leads to an effective Lagrangian, which can be written as

$$\mathcal{L}_{\mathrm{EM}} = -\frac{1}{4} F_{\mu\nu} F^{\mu\nu} - \frac{1}{2}\partial_\mu a \partial^\mu a - \frac{g_{a\gamma\gamma}}{4} a F_{\mu\nu} \tilde{F}^{\mu\nu}. \tag{D.1}$$

The coupling $g_{a\gamma\gamma}$ is not constant and can be enhanced by applying strong electromagnetic fields. In such a field, Axions can convert into photons and vice-versa, which is used by various Axion experiments such as ALPS [103, 104], ADMX [29] and HAYSTACK [30]. But also heterodyne cavity detectors such as MAGO should be in principle able to detect Axions. In the following,

we will therefore calculate the corresponding PSD and compare it with the GW signal.
We start with the modified maxwell equations, which can be easily deduced from the Lagrangian D.1 to be

$$\begin{aligned} \nabla \vec{E} &= \rho_{\text{eff}} \\ \nabla \times \vec{B} - \partial_t \vec{E} &= \vec{j}_{\text{eff}}, \end{aligned}$$

where we introduced an effective charge density and current given by

$$\begin{aligned} \rho_{\text{eff}} &= -g_{a\gamma\gamma} \vec{B} \cdot \nabla a \\ \vec{j}_{\text{eff}} &= -g_{a\gamma\gamma} (\vec{E} \times \nabla a - \vec{B} \frac{1}{c} \partial_t a). \end{aligned}$$

As in [3], we assume that the spatial gradients of the Axion field are small, i.e. $\nabla a = 0$. We already know how to find the PSD for this coupling, we just have to find the corresponding projected current. Applying eqn. 5.18, we can calculate

$$J_1(t) = \frac{1}{2U_1} \int_{V_{\text{cav}}} \mathrm{d}^3 x \frac{1}{\mu_0} \omega_1 \vec{E}_1(\vec{x}) \vec{j}_{\text{eff}}(t, \vec{x}) = \sqrt{\frac{U_0}{U_1}} \eta_{01}^{\text{A}} \omega_1 g_{a\gamma\gamma} b_0(t) \partial_t a(t),$$

where the overlap factor η_{01}^{A} is defined by

$$\eta_{01}^{\text{A}} := \frac{1}{2\sqrt{U_0 U_1}} \int_{V_{\text{cav}}} \mathrm{d}^3 x \sqrt{\frac{\varepsilon_0}{\mu_0}} \vec{E}_1(\vec{x}) \vec{B}_0(\vec{x}).$$

A fourier transformation of the current gives

$$J_1(\omega) = \sqrt{\frac{U_0}{U_1}} \eta_{01}^{\text{A}} \omega_1 g_{a\gamma\gamma} \int \frac{\mathrm{d}\omega'}{2\pi} (\omega - \omega') b_0(\omega') a(\omega - \omega').$$

We assume a monochromatic pump mode, i.e. $b_0(\omega') = 2\pi\delta(\omega' - \omega_0)$. Plugging the current into eqn. 6.15 and using $b_1(\omega) = A_1(\omega - (\omega_0 + \omega_g))$ gives

$$b_1(\omega) = \sqrt{\frac{U_0}{U_1}} \eta_{01}^{\text{A}} \omega_1 g_{a\gamma\gamma} \frac{(\omega - \omega_0) a(\omega - \omega_0)}{\Lambda_2(\omega - (\omega_0 + \omega_g))},$$

where ω_g is some arbitrary frequency that cancels in $\Lambda_2(\omega - (\omega_0 + \omega_g))$. From eqn. 3.30 and 6.19 (together with eqn. 3.27 and 3.28), we can directly calculate the signal PSD. The solution is

$$S_{\text{sig}}(\omega) = \frac{\omega_1}{Q_{\text{cpl}}} U_0 (\eta_{01}^{\text{A}} \omega_1 g_{a\gamma\gamma})^2 \frac{(\omega - \omega_0)^2 S_a(\omega - \omega_0)}{|\Lambda_2(\omega - (\omega_0 + \omega_g))|^2}. \tag{D.2}$$

We now evaluate this PSD by making some very specific assumptions. First of all, we assume that $S_a(\omega - \omega_0)$ is a monochromatic PSD centred at the Axion mass m_a, i.e. $S_a(\omega - \omega_0) = 4\pi^2 2\rho_{\text{DM}}/m_a^2 \delta(\omega - \omega_0 - m_a)$, where $\rho_{\text{DM}} = 3.07 \times 10^{-42}\,\text{GeV}^4$ is the local DM density (see [3] for more details). Furthermore, we make a scanning experiment, which means we can assume $Q_{\text{cpl}} = 10^{10}$. The parameters m_a and $g_{a\gamma\gamma}$ are in principle arbitrary with only some upper bounds from various Axion experiments (see e.g. [3]). We choose them such that, if the Axion

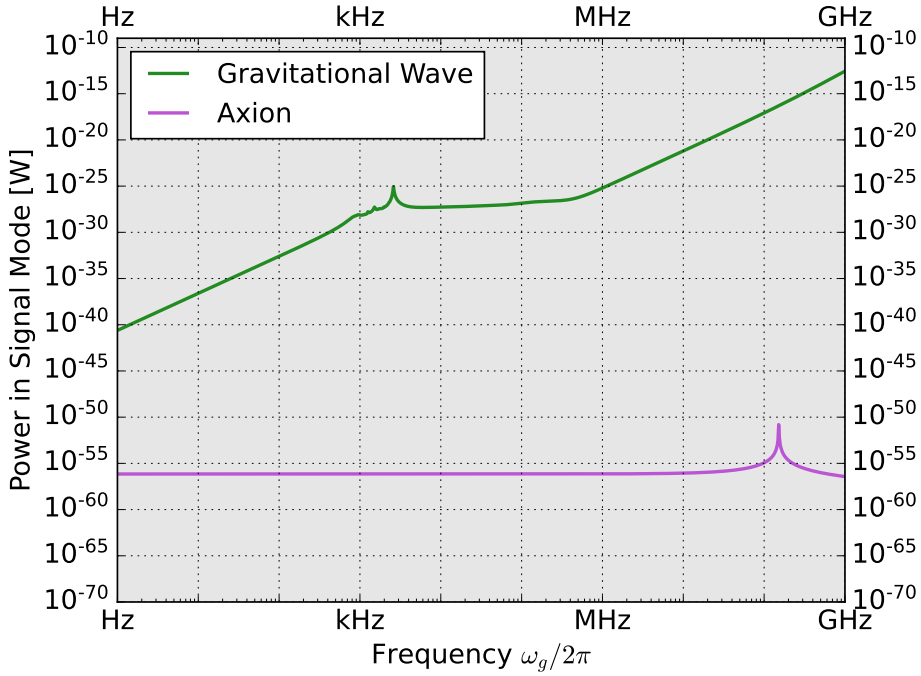

Figure D.1.: *Comparison of a GW signal with a dark matter Axion signal. Note that we consider very special cases for both effects: The GW is supposed to be monochromatic and resonant with the frequency difference of pump and signal modes. The Axion mass and coupling are fixed to values where it would explain the entire dark matter content in the universe. However, the possible parameter space is much larger. Note that there is a resonance in the Axion signal at $m_a = 10^{-7}\,eV \approx 152\,MHz$. The plot shows that due to the small coupling of $\eta_{01}^A \approx 10^{-7}$ to a MAGO-like cavity, the Axion signal is negligible and GWs are the much more promising source to find new physics.*

is a QCD Axion, it could in principle explain the dark matter content in the universe. So, according to [3], we have[1]

$$m_a = 10^{-7}\,\mathrm{eV} \qquad\qquad g_{a\gamma\gamma} = 5 \times 10^{-17}\,\mathrm{GeV}^{-1}.$$

The first step is to evaluate the overlap factor η_{01}^{A}. For the symmetric and antisymmetric TE_{011} modes in the MAGO cavity, it yields

$$\eta_{01}^{\mathrm{A}} \approx 4.06 \times 10^{-7},$$

so the coupling is considerably suppressed. The total signal power can be then written as (using eqn. 3.30)

$$P_{\mathrm{sig}} = \frac{\omega_1}{Q_{\mathrm{cpl}}} U_0 (\eta_{01}^{\mathrm{A}} \omega_1 g_{a\gamma\gamma})^2 \frac{2\rho_{\mathrm{DM}}}{|\Lambda_2(m_a - \omega_g)|^2}.$$

In figure D.1, we compare the signal power of the Axion with the signal power of a monochromatic GW propagating in z-direction (scanning case). The small coupling constant η_{01}^{A} leads to a

[1] Note that $g_{a\gamma\gamma}$ is not a constant since it depends on the EM-field strength. We assume a field strength as in the ALP DM experiment, which has been done in [3] as well.

suppressed Axion signal. Although it has to taken into account that we consider a very special case for the parameters m_a and $g_{a\gamma\gamma}$, we conclude that the MAGO cavity is not suitable to measure Axions. A solution could be to use a different cavity geometry with enhanced coupling $\eta_{01}^{\mathrm{A}} \sim 1$. In [3], for instance, it was suggested to use cylindrical cavities.

E. MAGO Parameters

In this chapter, we summarize the most important parameters for the numerical simulations. This also includes a list of the 98 strongest couplings of the MAGO-like cavity.

Table E.1.: *This table lists the parameter used for the numerical calculations in this these. Note that some of them are fixed, while others can be varied (such as the temperature, energy in the pump mode etc.). When we explicitly calculate the total signal, we assume an optimistic GW strain of* $h_0 = 10^{-20}$*. The values are chosen such that they are compareable to [2, 4]. Note that RRR 300 means that the niobium has a residual resistivity ratio of 300 and RT stands for room temperature.*

Description	Symbol	Value
EM Quality Factors (Scanning)	Q_0 Q_{int} Q_{cpl}	10^{10} 10^{10} 10^{10}
EM Quality Factors (Broadband)	Q_0 Q_{int} Q_{cpl}	10^{10} 10^{10} $\max\left(10^5, \frac{2\omega_0}{\omega_g}\right)$
Mechanical Quality Factor	Q_l	10^6
Pump Mode Frequency	ω_0	1.773430 GHz
Signal Mode Frequency	ω_1	1.773446 GHz
Cavity Mass	M	5 kg
Cavity Wall Thickness	w	2 mm
Cavity Volume	V_{cav}	$0.00956\,\text{m}^3$
Cavity Surface	A_{cav}	$0.3111\,\text{m}^2$
Lowest Lying Mode	ω_{min}	0.05 kHz
Minimal Displacement	q_{rms}	0.1 nm
Temperature (for cold run)	T	1.8 K
Strain Normalization	H	$h_0 \times 12\,\text{m}^2$
GW-EM overlap	$\eta_{01}^{\text{E,B}}$	0.2
Axion Overlap	η_{01}^{A}	4.06×10^{-7}
Energy in Pump Mode	U_0	40 J
Density Niobium (RRR 300, RT)	ρ	$8570\,\text{kg/m}^3$
Young's Modulus (Nb RRR 300, RT)	E	106 GPa
Poisson's Ration (Nb RRR 300, RT)	ν	0.40

Table E.2.: *This list show the 98 modes that have the strongest coupling to the GW. They are selected according to the condition* $|C^l_{01}| \geq 0.001$, $|\Gamma_+| \geq 0.0001$, $|\Gamma_\times| \geq 0.0001$.

Frequency ω_l	C^l_{01}	Γ_+	$\Gamma_\times$
5.1396	−0.0117	0.0021	−0.0004
5.1466	0.7243	−0.0002	−0.0006
5.1609	−0.0115	−0.0002	0.0003
5.1620	0.0020	−0.0009	−0.0003
5.1675	0.0063	−0.0007	0.0003
5.1717	−0.0090	−0.0006	−0.0007
5.1747	−0.0022	0.0004	0.0008
5.1986	0.0052	−0.0033	−0.0007
5.2019	0.0242	−0.0006	0.0005
5.2318	−0.0035	−0.0102	0.0004
5.3854	−0.0042	0.0003	0.0002
5.4092	−0.0052	0.0003	0.0002
5.9586	0.1616	−0.0033	0.0017
5.9610	−0.0230	−0.0026	0.0006
5.9916	0.0022	−0.0029	−0.0002
5.9922	−0.0019	−0.0005	0.0003
5.9969	−0.0018	−0.0002	0.0003
6.0125	−0.0011	−0.0001	−0.0005
6.0520	0.0012	0.0004	0.0002
6.0734	−0.0017	0.0010	−0.0001
6.7889	0.0307	0.0053	0.0004
6.8049	−0.0050	−0.0007	0.0007
6.8076	0.0048	0.0006	−0.0019
6.8142	−0.0059	−0.0012	−0.0042
6.8274	−0.0170	0.0004	0.0006
6.9568	−0.0024	−0.0003	−0.0006
6.9670	−0.0022	0.0010	−0.0003
6.9707	0.0024	−0.0007	−0.0002
7.8904	0.0013	−0.0012	−0.0009
7.8948	0.0098	−0.0014	−0.0003
7.9000	0.0069	−0.0018	0.0006
7.9718	−0.0039	0.0005	0.0009
7.9726	−0.0030	−0.0006	−0.0005
7.9792	0.0016	−0.0006	−0.0003
7.9959	−0.0031	0.0006	−0.0007
9.2202	−0.0477	−0.0052	0.0052
9.2330	−0.0289	−0.0023	0.0026
9.2536	0.0079	−0.0017	−0.0053
9.2565	0.0037	−0.0009	0.0036
9.2640	−0.0041	0.0007	0.0012

Frequency ω_l	C_{01}^l	Γ_+	$\Gamma_\times$
9.2723	0.0032	0.0008	0.0017
9.2838	0.0017	−0.0005	−0.0010
9.2990	0.0021	−0.0002	0.0010
9.3917	−0.0068	−0.0006	0.0001
9.4132	0.0048	−0.0005	0.0007
9.4467	−0.0183	−0.0008	0.0012
9.4902	−0.0017	−0.0042	0.0003
9.5547	0.0029	0.0012	0.0005
9.5706	−0.0023	0.0024	−0.0006
9.5971	−0.0069	−0.0004	−0.0083
9.6029	0.0201	−0.0031	−0.0002
9.6050	0.0438	0.0039	−0.0005
9.6536	0.0037	−0.0002	0.0004
9.6604	0.0036	0.0007	−0.0001
9.6859	−0.0017	0.0005	0.0005
9.7159	−0.0013	0.0004	0.0002
10.7255	0.0608	0.0013	0.0004
10.7608	0.0024	−0.0012	−0.0002
10.8048	0.0067	0.0010	0.0005
10.8647	−0.0021	−0.0004	−0.0004
10.8733	−0.0017	−0.0012	0.0003
10.9208	−0.0035	−0.0006	−0.0004
10.9483	−0.0027	0.0008	0.0004
11.4891	−0.0039	−0.0007	−0.0001
12.3825	−0.0134	−0.0026	−0.0008
12.3882	−0.0065	−0.0024	−0.0002
12.4256	−0.0046	0.0006	−0.0007
12.4399	0.0046	−0.0002	0.0006
12.4677	−0.0028	0.0002	−0.0004
12.4832	−0.0019	0.0009	0.0006
12.5046	0.0010	−0.0003	−0.0001
13.9871	0.0403	−0.0026	0.0013
13.9968	−0.0011	0.0011	−0.0003
14.0120	−0.0075	−0.0002	0.0001
14.0203	0.0059	−0.0006	−0.0006
14.0278	−0.0044	0.0003	0.0011
14.0348	−0.0012	−0.0002	−0.0004
14.0370	0.0020	−0.0002	−0.0001
14.0694	0.0025	−0.0003	0.0002
14.1734	−0.0021	0.0004	−0.0002
15.8242	0.0111	−0.0031	0.0006
15.8248	−0.0087	0.0037	0.0028
15.8429	−0.0314	−0.0005	0.0008
15.8599	0.0058	−0.0009	0.0011

Frequency ω_l	C_{01}^l	Γ_+	$\Gamma_\times$
15.8728	0.0033	0.0004	−0.0040
15.8932	−0.0036	−0.0017	0.0003
15.9152	0.0013	0.0005	0.0014
15.9884	0.0013	−0.0003	0.0018
16.0606	−0.0018	−0.0021	0.0014
16.0698	−0.0016	−0.0015	−0.0028
16.1045	0.0012	0.0005	0.0033
16.2805	−0.0010	−0.0037	0.0025
16.3200	0.0018	0.0068	−0.0036
16.3296	0.0017	−0.0022	−0.0007
16.3301	0.0076	−0.0111	−0.0042
16.3419	−0.0039	−0.0074	−0.0240
16.3579	0.0017	−0.0056	−0.0096
16.3674	−0.0017	−0.0235	0.0047

Bibliography

[1] B. P. Abbott et al. "Observation of Gravitational Waves from a Binary Black Hole Merger". In: *Phys. Rev. Lett.* 116 (6 Feb. 2016), p. 061102.

[2] R Ballantini et al. "Microwave Apparatus for Gravitational Waves Observation". In: (2005). arXiv: 0502054v1 [gr-gc].

[3] Asher Berlin et al. "Axion Dark Matter Detection by Superconducting Resonant Frequency Conversion". In: (2019). arXiv: 1912.11048 [hep-ph].

[4] Asher Berlin et al. "MAGO 2.0 : Electromagnetic Cavities as Mechanical Bars for Gravitational Waves". In: (2023). arXiv: arXiv:2303.01518v1 [hep-ph].

[5] Ph. Bernard et al. "A Detector of Gravitational Waves Based on Coupled Microwave Cavities". In: (2002). arXiv: 0203024v1 [gr-gc].

[6] R. Abbott et al. "GWTC-3: Compact Binary Coalescences Observed by LIGO and Virgo During the Second Part of the Third Observing Run". In: (2021). arXiv: 2111.03606 [gr-qc].

[7] Marica Branchesi et al. "Science with the Einstein Telescope: a comparison of different designs". In: (2023). arXiv: 2303.15923 [gr-qc].

[8] Stefan Hild, Simon Chelkowski, and Andreas Freise. "Pushing towards the ET sensitivity using 'conventional' technology". In: (2008). arXiv: 0810.0604 [gr-qc].

[9] M Punturo et al. "The Einstein Telescope: a third-generation gravitational wave observatory". In: *Classical and Quantum Gravity* 27.19 (2010), p. 194002.

[10] Pau Amaro-Seoane et al. "Laser Interferometer Space Antenna". In: (2017). arXiv: 1702.00786 [astro-ph.IM].

[11] Michele Maggiore. *Gravitational Waves Volume 1: Theory and Experiments*. Oxford University Press, 2007.

[12] J. Weber. "Detection and Generation of Gravitational Waves". In: *Phys. Rev.* 117 (1 1960), pp. 306–313.

[13] P. Astone et al. "Long-term operation of the Rome "Explorer" cryogenic gravitational wave detector". In: *Phys. Rev. D* 47 (1993), pp. 362–375.

[14] Pia Astone et al. "The gravitational wave detector NAUTILUS operating at T= 0.1 K". In: *Astroparticle Physics* 7.3 (1997), pp. 231–243.

[15] E. Mauceli et al. "The Allegro gravitational wave detector: Data acquisition and analysis". In: *Physical Review D* 54.2 (1996), pp. 1264–1275. arXiv: 9609058v3 [gr-qc].

[16] Andrea Vinante and (forthe AURIGA Collaboration). "Present performance and future upgrades of the AURIGA capacitive readout". In: *Classical and Quantum Gravity* 23.8 (2006), S103–S110.

[17] Asimina Arvanitaki and Andrew A. Geraci. "Detecting High-Frequency Gravitational Waves with Optically Levitated Sensors". In: *Physical Review Letters* 110.7 (2013).

[18] Maxim Goryachev and Michael E. Tobar. "Gravitational wave detection with high frequency phonon trapping acoustic cavities". In: *Phys. Rev. D* 90 (10 2014), p. 102005.

[19] Maxim Goryachev et al. "Rare events detected with a bulk acoustic wave high frequency gravitational wave antenna". In: *Physical Review Letters* 127.7 (2021), p. 071102. arXiv: 2102.05859 [gr-qc].

[20] Paul D Lasky and Eric Thrane. "Did Goryachev et al. detect megahertz gravitational waves?" In: *Physical Review D* 104.10 (2021), p. 103017. arXiv: 2110.13319 [gr-qc].

[21] J. Anandan and R. Y. Chiao. "Gravitational radiation antennas using the Sagnac effect". In: *General Relativity and Gravitation* 14.6 (1982), pp. 515–521.

[22] C. Kiefer and C. Weber. "On the interaction of mesoscopic quantum systems with gravity". In: *Annalen der Physik* 517.4 (2005), pp. 253–278.

[23] Jonathan Gräfe, Falk Adamietz, and Ralf Schützhold. *Energy transfer between gravitational waves and quantum matter*. 2023. arXiv: 2302.14694 [quant-ph].

[24] Dennis Rätzel et al. "Dynamical response of Bose–Einstein condensates to oscillating gravitational fields". In: *New Journal of Physics* 20.7 (2018), p. 073044.

[25] UHF-GW Initiative. *Ultra-High-Frequency Gravitational Waves*. 2021. URL: https://www.ctc.cam.ac.uk/activities/UHF-GW.php (visited on 04/08/2023).

[26] Nancy Aggarwal et al. "Challenges and opportunities of gravitational-wave searches at MHz to GHz frequencies". In: *Living reviews in relativity* 24.1 (2021), pp. 1–74.

[27] Mikhail Evgeny Gertsenshtein. "Wave resonance of light and gravitational waves". In: *Soviet Physics Jetp* 14 (1962), pp. 84–85.

[28] Ya B Zel'dovich. "Electromagnetic and gravitational waves in a stationary magnetic field". In: *Zh. Eksp. Teor. Fiz* 65 (1973), pp. 1311–1315.

[29] R. Khatiwada et al. "Axion dark matter experiment: Detailed design and operations". In: *Review of Scientific Instruments* 92.12 (2021), p. 124502. arXiv: 2010.00169v1 [astro-ph.IM].

[30] L. Zhong et al. "Results from phase 1 of the HAYSTAC microwave cavity axion experiment". In: *Physical Review D* 97.9 (2018), p. 092001. arXiv: 1803.03690v1 [hep-ex].

[31] Asher Berlin et al. "Detecting High-Frequency Gravitational Waves with Microwave Cavities". In: (2021). arXiv: 2112.11465v1 [hep-ph].

[32] V. B. Braginskii and M. B. Menskii. "High-Frequency Detection of Gravitational Waves". In: *JETP Letters* 13.11 (1971), pp. 417–419.

[33] V. B. Braginskii et al. "Electromagnetic detectors of gravitational waves". In: *Zh. Eksp. Teor. Fiz.* 65 (1973), pp. 1729–1737.

[34] Carlton M. Caves. "Microwave cavity gravitational radiation detectors". In: *Physics Letters B* 80.3 (1979), pp. 323–326.

[35] F. Pegoraro et al. "Electromagnetic Detector for Gravitational Waves". In: *Physics Letters A* 68.2 (1978), pp. 165–168.

[36] Francesco Pegoraro, Emilio Picasso, and LA Radicati. "On the operation of a tunable electromagnetic detector for gravitational waves". In: *Journal of Physics A: Mathematical and General* 11.10 (1978), p. 1949.

[37] Francesco Pegoraro and LA Radicati. "Dielectric tensor and magnetic permeability in the weak field approximation of general relativity". In: *Journal of Physics A: Mathematical and General* 13.7 (1980), pp. 2411–2421.

[38] Alberto J. Lobo. "What can we learn about gravitational wave physics with an elastic spherical antenna?" In: *Physical Review D.* 52 (1995).

[39] CE Reece, PJ Reiner, and AC Melissinos. "Observation of 4× 10-17 cm harmonic displacement using a 10 GHz superconducting parametric converter". In: *Physics Letters A* 104.6-7 (1984), pp. 341–344.

[40] Ph Bernard et al. "A detector of small harmonic displacements based on two coupled microwave cavities". In: *Review of Scientific Instruments* 72.5 (2001), pp. 2428–2437. arXiv: 0103006v2 [gr-gc].

[41] Ph Bernard et al. *Coupled Microwave Cavities for the Detection of Small Harmonic Displacements*. Tech. rep. SCAN-9906068, 1998.

[42] Ph Bernard et al. "Coupled superconducting cavities for the detection of weak forces". In: *Part. Accel.* 61 (1998), pp. 79–86.

[43] Asher Berlin et al. "Heterodyne Broadband Detection of Axion Dark Matter". In: (2020). arXiv: 2007.15656v1 [hep-ph].

[44] Sebastian Ellis. "Talk: Revisiting Gravitational Wave Detection in an SRF Cavity". In: (2021). URL: https://indico.cern.ch/event/982987/contributions/4201176/attachments/2206617/3733620/GWavesRF_CERN.pdf.

[45] Raffaele Tito D'Agnolo. "Quantum Universe Colloquium: A New Chapter in the Quest for Dark Matter: the Ultralight Regime". In: *Particle and Astroparticle Physics Colloquium Hamburg* (2022). URL: https://indico.desy.de/event/32903/attachments/75236/101453/dagnolo_DM_colloquium.pdf.

[46] Nicolas Herman et al. "Detecting Planetary-mass Primordial Black Holes with Resonant Electromagnetic Gravitational Wave Detectors". In: (2021). arXiv: 2012.12189v2 [gr-qc].

[47] Dieter Proch et al. "Niobium in superconducting RF cavities". In: *Niobium, Science and Technology* (2001).

[48] Georg Goubau. *Electromagnetic Waveguides and Cavities*. Pergamon Press, 1961.

[49] John David Jackson. *Klassische Elektrodynamik*. de Gruyter, 2006.

[50] Richard Courant and David Hilbert. *Methoden der mathematischen Physik*. Springer-Verlag, 1993.

[51] Athanasios Papoulis and S. Unnikrishna Pillai. *Probability, Random Variables and Stochastic Processes*. McGraw-Hill, 2002.

[52] L.D. Landau and E.M. Lifschitz. *Lehrbuch der Theoretischen Physik VII, Elastizitätstheorie*. Akademie Verlag, 1987.

[53] Kip S. Thorne and Roger D. Blandford. *Volume 3 of Modern Classical Physics, Elasticity and Fluid Dynamics*. Princeton University Press, 2021.

[54] Peter R. Saulson. "Thermal noise in mechanical experiments". In: *Physical Review D*. 42 (1990), pp. 2437–2445.

[55] Sebastian Boblest, Thomas Müller, and Günter Wunner. *Spezielle und allgemeine Relativitätstheorie: Grundlagen, Anwendungen in Astrophysik und Kosmologie sowie relativistische Visualisierung*. Springer Spektrum, 2015.

[56] James B. Hartle. *Gravity, An Introduction To Einstein's General Relativity*. Pearson Education, 2003.

[57] Charles W. Misner, Kip S. Thorne, and John Archibald Wheeler. *Gravitation*. Macmillan Education, 1973.

[58] Pierluigi Fortini and Antonello Ortolan. "Gauge Transformations in Linearized Theory of Gravitational Waves". In: *Problems of Fundamental Physics II, Proceedings of the 5th Winter School on Hadronic Physics* (1990), pp. 379–389.

[59] Chiara Caprini and Daniel G. Figueroa. "Cosmological Backgrounds of Gravitational Waves". In: (2020). arXiv: 1801.04268v3 [astro-ph.CO].

[60] Fred K. Manasse and Charles W. Misner. "Fermi Normal Coordinates and Some Basic Concepts in Differential Geometry". In: *J. Math. Phys.* 4 (1963), pp. 735–745.

[61] Wei-Tou Ni and Mark Zimmermann. "Inertial and gravitational effects in the proper reference frame of an accalerated, rotating observer". In: *Physical Review D* 17 (1978), pp. 1473–1476.

[62] Wann-Quan Li and Wei-Tou Ni. "Coupled inertial and gravitational effects in the proper reference frame of an accelerated, rotating observer". In: *J. Math. Phys.* 20 (1979), pp. 1473–1480.

[63] Wann-Quan Li and Wei-Tou Ni. "Expansions of the affinity, metric and geodesic equations in Fermi normal coordinates about a geodesic". In: *J. Math. Phys.* 20 (1979), pp. 1925–1929.

[64] P.L. Fortini and C. Gualdi. "Fermi Normal Co-ordinate System and Electromagnetic Detectors of Gravitational Waves". In: *Nuovo Cimento* 71B.1 (1982), pp. 37–54.

[65] Karl-Peter Marzlin. "Fermi coordinates for weak gravitational fields". In: *Physical Review D* 50 (1994), pp. 888–891.

[66] Malik Rakhmanov. "Fermi-normal, optical, and wave-synchronous coordinates for spacetime with a plane gravitational wave". In: *Classical Quantum Gravity* 31 (2014), pp. 1–34.

[67] Anna Grasselino. "Talk: Dark SRF - experiment". In: (2019). URL: https://indico.fnal.gov/event/19433/contributions/52137/attachments/32415/39710/DarkSRF.pdf.

[68] Y.M. Pischalnikov et al. "Operation of an SRF Cavity Tuner Submerged into Liquid He". In: International Conference on RF Superconductivity 19 (2019), pp. 660–663.

[69] Wolfgang Nolting. *Grundkurs Theoretische Physik 6, Statistische Physik*. Springer-Verlag, 2007.

[70] Saptarshi Chaudhuri et al. "Optimal Electromagnetic Searches for Axion and Hidden-Photon Dark Matter". In: (2019). arXiv: 1904.05806v2 [hep-ex].

[71] B. Brubaker et al. "First results from a microwave cavity axion search at 24 micro-eV". In: *Phys. Rev. D* 118 (1 2016), p. 015149. arXiv: 1610.02580v3 [astro-ph.CO].

[72] Berkeley Nucleonics Corporation. *Model 865-M Wideband Synthesizer*. 2019. URL: https://www.berkeleynucleonics.com/sites/default/files/product-downloads/865-m_datasheet_v1.04.pdf.

[73] David M Pozar. *Microwave engineering*. Wiley, 2011.

[74] Enrico Rubiola. *Phase Noise and Frequency Stability in Oscillators*. Cambridge University Press, 2008.

[75] Joshua Wiener and Hasan Padamsee. "Improvements in Field Emission: A Statistical Model for Electropolished Baked Cavities". In: *Conf. Proc. C* 806233.MOPP164 (2008), pp. 934–936.

[76] Hasan Padamsee. *RF superconductivity: science, technology, and applications*. John Wiley & Sons, 2009.

[77] Hasan Padamsee, J. Knobloch, and T. Hays. *RF Superconductivity for Accelerators*. John Wiley & Sons, 1998.

[78] Michele Maggiore. *Gravitational Waves Volume 2: Astrophysics and Cosmology*. Oxford University Press, 2018.

[79] Andreas Ringwald, Jan Schütte-Engel, and Carlos Tamarit. "Gravitational waves as a big bang thermometer". In: *Journal of Cosmology and Astroparticle Physics* 2021.03 (2021), p. 054. arXiv: 2011.04731v2 [hep-ph].

[80] T. Byrnes Christian and S. Cole Philippa. "Lecture notes on inflation and primordial black holes". In: (2021). arXiv: 2112.05716 [astro-ph.CO].

[81] Gabriele Franciolini, Anshuman Maharana, and Francesco Muia. "The Hunt for Light Primordial Black Hole Dark Matter with Ultra-High-Frequency Gravitational Waves". In: (2022). arXiv: 2205.02153v1 [astro-ph.CO].

[82] Keisuke Inomata, Masahiro Kawasaki, and Yuichiro Tada. "Revisiting constraints on small scale perturbations from big-bang nucleosynthesis". In: *Physical Review D* 94.4 (2016). arXiv: 1605.04646v2 [astro-ph.CO].

[83] Boyuan Liu and Volker Bromm. "Accelerating Early Massive Galaxy Formation with Primordial Black Holes". In: *The Astrophysical Journal Letters* 937.2 (2022), p. L30.

[84] Przemek Mróz et al. "No large population of unbound or wide-orbit Jupiter-mass planets". In: *Nature* 548.7666 (2017), pp. 183–186. arXiv: 1707.07634v1 [astro-ph.EP].

[85] Niikura Hiroko et al. "Constraints on Earth-mass primordial black holes from OGLE 5-year microlensing events". In: *Physical Review D* 99.8 (2019). arXiv: arXiv:1901.07120v2 [astro-ph.CO].

[86] Takashi Nakamura et al. "Gravitational Waves from Coalescing Black Hole MACHO Binaries". In: *The Astrophysical Journal* 487.2 (1997), pp. L139–L142. arXiv: 9708060v1 [astro-ph].

[87] Simeon Bird et al. “Did LIGO Detect Dark Matter?” In: *Physical Review Letters* 116.20 (2016). arXiv: 1603.00464v2 [astro-ph.CO].

[88] Sebastien Clesse and Juan Garcia-Bellido. “The clustering of massive Primordial Black Holes as Dark Matter: Measuring their mass distribution with advanced LIGO”. In: *Physics of the Dark Universe* 15 (2017), pp. 142–147. arXiv: 1603.05234v2 [astro-ph.CO].

[89] Hideaki Mouri and Yoshiaki Taniguchi. “Runaway Merging of Black Holes: Analytical Constraint on the Timescale”. In: *The Astrophysical Journal* 566.1 (2002), pp. L17–L20. arXiv: 0201102v2 [astro-ph].

[90] Richard Brito, Vitor Cardoso, and Paolo Pani. *Superradiance: New Frontiers in Black Hole Physics*. Springer, 2020.

[91] Asimina Arvanitaki, Masha Baryakhtar, and Xinlu Huang. “Discovering the QCD axion with black holes and gravitational waves”. In: *Phys. Rev. D* 91 (8 2015), p. 084011. arXiv: 1411.2263v3 [hep-ph].

[92] R. Penrose. “Gravitational collapse: The role of general relativity”. In: *Riv. Nuovo Cim.* 1 (1969), pp. 252–276.

[93] Nancy Aggarwal et al. “Searching for new physics with a levitated-sensor-based gravitational-wave detector”. In: (2020). arXiv: 2010.13157 [gr-qc].

[94] Masha Baryakhtar et al. “Black hole superradiance of self-interacting scalar fields”. In: *Phys. Rev. D* 103 (9 2021), p. 095019. arXiv: arXiv:2011.11646v2 [hep-ph].

[95] Ludwig Bergmann. *Lehrbuch der Experimentalphysik II, Elektrizität und Magnetismus*. de Gruyter, 1986.

[96] Wilfried Plassmann and Detlef Schulz. *Handbuch Elektrotechnik*. Springer Vieweg, 2013.

[97] C. A. Baker et al. “Improved Experimental Limit on the Electric Dipole Moment of the Neutron”. In: *Phys. Rev. Lett.* 97 (13 2006), p. 131801.

[98] R. D. Peccei and Helen R. Quinn. “CP Conservation in the Presence of Pseudoparticles”. In: *Phys. Rev. Lett.* 38 (25 1977), pp. 1440–1443.

[99] Steven Weinberg. “A New Light Boson?” In: *Phys. Rev. Lett.* 40 (4 1978), pp. 223–226.

[100] F. Wilczek. “Problem of Strong P and T Invariance in the Presence of Instantons”. In: *Phys. Rev. Lett.* 40 (5 1978), pp. 279–282.

[101] Asimina Arvanitaki et al. “String axiverse”. In: *Phys. Rev. D* 81 (12 2010), p. 123530.

[102] H. Primakoff. “Photo-Production of Neutral Mesons in Nuclear Electric Fields and the Mean Life of the Neutral Meson”. In: *Phys. Rev.* 81 (5 1951), pp. 899–899.

[103] R Bähre et al. “Any light particle search II — Technical Design Report”. In: *Journal of Instrumentation* 8.09 (2013), T09001.

[104] Katharina-Sophie Isleif. “The Any Light Particle Search Experiment at DESY”. In: *Moscow University Physics Bulletin* 77.2 (2022), pp. 120–125. arXiv: 2202.07306v1 [hep-ex].

Eidesstattliche Erklärung

Ich versichere, dass ich die beigefügte schriftliche Masterarbeit selbstständig angefertigt und keine anderen als die angegebenen Hilfsmittel benutzt habe. Alle Stellen, die dem Wortlaut oder dem Sinn nach anderen Werken entnommen sind, habe ich in jedem einzelnen Fall unter genauer Angabe der Quelle deutlich als Entlehnung kenntlich gemacht. Dies gilt auch für alle Informationen, die dem Internet oder anderer elektronischer Datensammlungen entnommen wurden. Ich erkläre ferner, dass die von mir angefertigte Masterarbeit in gleicher oder ähnlicher Fassung noch nicht Bestandteil einer Studien- oder Prüfungsleistung im Rahmen meines Studiums war. Die von mir eingereichte schriftliche Fassung entspricht jener auf dem elektronischen Speichermedium. Ich bin damit einverstanden, dass die Masterarbeit veröffentlicht wird.

19.04.2023 — Ort, Datum

Robin Gömbel — Unterschrift